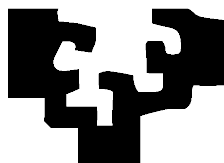# Contributions to the Analysis and Segmentation of Remote Sensing Hyperspectral Images

By

Miren Josune Gallego Merino

http://www.ehu.es/ccwintco

Dissertation presented to the Department of Computer Science
and Artificial Intelligence in partial fulfillment of the requirements
for the degree of
Doctor of Philosophy

PhD Advisor:

Prof. Manuel Graña Romay

At
The University of the Basque Country
Donostia - San Sebastian
2011

Universidad Euskal Herriko
del País Vasco Unibertsitatea

AUTORIZACION DEL/LA DIRECTOR/A DE TESIS

PARA SU PRESENTACION

Dr/a. _____ con N.I.F. _____

como Director/a de la Tesis Doctoral: _____

_____

_____

realizada en el Departamento _____

_____

por el Doctorando Don/ña. _____ ,

autorizo la presentación de la citada Tesis Doctoral, dado que reúne las condiciones

necesarias para su defensa.

En _____ a _____ de _____ de _____

EL/LA DIRECTOR/A DE LA TESIS

Fdo.: _____

CONFORMIDAD DEL DEPARTAMENTO

El Consejo del Departamento de _____

_____

en reunión celebrada el día _____ de _____ de _____ ha acordado dar la

conformidad a la admisión a trámite de presentación de la Tesis Doctoral titulada: _____

_____

_____

dirigida por el/la Dr/a. _____

_____

y presentada por Don/ña. _____

ante este Departamento.

En _____a _____de _____de _____

Vº Bº DIRECTOR/A DEL DEPARTAMENTO   SECRETARIO/A DEL DEPARTAMENTO

Fdo.: _____   Fdo.: _____

eman ta zabal zazu

Universidad **Euskal Herriko**
del País Vasco **Unibertsitatea**

ACTA DE GRADO DE DOCTOR

ACTA DE DEFENSA DE TESIS DOCTORAL

DOCTORANDO DON/ÑA. _____

TITULO DE LA TESIS: _____

_____

_____

El Tribunal designado por la Subcomisión de Doctorado de la UPV/EHU para calificar la Tesis Doctoral arriba indicada y reunido en el día de la fecha, una vez efectuada la defensa por el doctorando y contestadas las objeciones y/o sugerencias que se le han formulado, ha otorgado por_____la calificación de:

unanimidad ó mayoría

En _____a _____de _____de _____

EL/LA PRESIDENTE/A,   EL/LA SECRETARIO/A,

Fdo.:   Fdo.:

Dr/a: _____   Dr/a: _____

VOCAL 1º,   VOCAL 2º,   VOCAL 3º,

Fdo.:   Fdo.:   Fdo.:

Dr/a: _____Dr/a:_____Dr/a:_____

EL/LA DOCTORANDO/A,

Fdo.: __

Acknowledgements

Contributions to the Analysis and Segmentation of Remote Sensing Hyperspectral Images

by

Miren Josune Gallego

abstract

This PhD Thesis deals with the segmentation of hyperspectral images from the point
of view of Lattice Computing. We have introduced the application of Associative
Morphological Memories as a tool to detect strong lattice independence, which has
been proven equivalent to affine independence. Therefore, sets of strong lattice inde-
pendent vectors found using our algorithms correspond to the vertices of convex sets
that cover most of the data. Unmixing the data relative to these endmembers pro-
vides a collection of abundance images which can be assumed either as unsupervised
segmentations of the images or as features extracted from the hyperspectral image
pixels. Besides, we have applied this feature extraction to propose a content based
image retrieval approach based on the image spectral characterization provided by
the endmembers. Finally, we extended our ideas to the proposal of Morphological
Cellular Automata whose dynamics are guided by the morphological/lattice indepen-
dence properties of the image pixels. Our works have also explored the applicability
of Evolution Strategies to the endmember induction from the hyperspectral image
data.

Contents

List of Algorithms

List of Figures

List of Tables

Chapter 1

Introduction

This chapter provides a general introduction to this Thesis. We discuss the general motivation of the works in Section 1.1. We detail the contributions of this Thesis in Section 1.2. Section 1.3 details the publications produced during the work on this Thesis. Finally, Section 1.4 details the structure of the Thesis.

1.1 Introduction

The main topic of this Thesis, from an application point of view, is the unsupervised processing of remote sensing hyperspectral images. Hyperspectral sensors have been proposed as new evolution of the optical remote sensing devices, providing a fine sampling of the visible and near infrared spectrum. Each image pixel is a high dimensional vector corresponding to a fine sampling of the incoming radiance at this pixel. Such increased spectral resolution was expected to improve the ability of automatic image processing techniques to identify materials in the scene, allowing for better and more robust detection and segmentation algorithms. The point of view in this thesis is that the processing algorithms are unsupervised because no information about the true contents of the image is assumed.

Our main interest is to perform unsupervised segmentation of the hyperspectral images. More specifically, we assume a linear mixing model of the pixel spectra. In this model, the observed spectra is assumed to be a linear composition of

elemental spectra, called endmembers. These endmembers correspond to pure materials in the scene, and the linear aggregation is assumed to be an effect of the low spatial resolution of the image capturing device. The linear coefficients are the fractiona abundances of each endmember in the pixel composition. Taking the image as a whole, the abundance coefficients for each endmembers can be viewed as an image, and the whole collection of abundace images as a multiband image that provide a segmentation of the image into meaningful regions of high abundance of specific materials.

Therefore, from the point of vew of computational techniques, our approach consists in the induction (identification) of the endmembers from the image data in an unsupervised way. To this end, we have considered the application of the theory developed around the Autoassociative Morphological Memories (AMM). The morphological independence is a key property for the detection of endmembers in the image data. In our work we have proposed the AMM for this detection task. Much of this Thesis is devoted to this single, but very important, issue. We have also tested some evolutionary algorithm approaches for the induction of the endmembers from the image data. The evolutionary algorithm follows the Michigan approach, which implies some original reformulation of the process.

Besides this we have found that the unmixing features, the endmembers, can also be used for search in large scale hyperspectral image databases. This is an application of our approach to Content Based Image Retrieval (CBIR) that is unique, because no other approach deals with the spectral content of the images in order to answer queries to the image database.

An issue that deserves special attention is that of validation. Labeled hyperspectral data is scarce, therefore we tried to develop resources for an improved validation of the proposed approaches and their competing algorithms. We have built a hyperspectral image synthesis toolbox allowing for extensive quantitative validation procedures.

Finally, we have extended our work on AMM and morphological independence to propose a Cellular Morphological Automaton which uses the morphological independence to obtain robust segmentations of color images.

1.2 Contributions of this Thesis

- Endmembers in the image are the vertices of a convex polygon covering the data samples. Therefore, endmembers are affinely independent vectors. We have identified the morphological independence with the affine independence. Further works by G.X. Ritter [79, 81] have developed the theoretical foundations supporting this idea.

- The idea of detecting endmembers on the basis of morphological independence properties has led to the application of AMM to the detection of the endmembers proposed in the image spectra. We have proposed an innovative algorithm exploiting this idea. This proposal has been tested thoroughfully on real hyperspectral images and synthetic images. We have made a strong effort in this validation process, showing the improvements obtained with our algorithm versus other linear transformations and endmember induction algorithms found in the literature.

- Validation of the AMM based approach to endmember induction includes the use of the abundance coefficients as feature vectors for classification. This approach has been found advantageous when tested on one hyperspectral image, building supervised classifiers of image pixel spectra.

- We have proposed and validated the use of endmembers as image features for Content Based Image Retrieval (CBIR) in hyperspectral image databases. We have defined a specific distance on the collections of endmembers that the image spectral features for CBIR. We apply two different Endmember Induction Algorithms (EIAs) to demonstrate that the approach is robust and does not depend too much on the EIA applied or on the underlying distance.

- We have proposed a Single Individual Evolutionary Strategy (SIES) following the Michigan approach for the induction of indemembers from the data. The proposed algorithm is faster and much more effective than a conventionalEvolutionary Strategy (ES), tailored to this task. The SIE considers a set of endmembers as an evolving population. Individuals correspond to hypothetical endmember spectra, and they are selected as candidates for mutation on the basis of their partial abundance images. The population's global fitness when the mutated individual substitutes its parent is the measure of the goodness of the individual. Although the

3

aim of defining the SIE was to reduce the computational cost of applying ES to the high volume data in hyperspectral images, we have found that SIE also improves the fitness performance of conventional ES.

- We have proposed a Morphological Cellular Automaton (MCA) for the segmentation of color images based on morphological independence instead of linear filters. This MCA also posseses a scale parameter allowing to tune the resolution of the segmentation. The MCA has assured convergence to a state characterized by morphological dependences and independences between neighboring cell states. Cell dynamic rules test morphological dependence among neighboring cell's states. When neighboring cell states are morphological dependent in the erosive or dilative sense, the morphologically dominant state colonizes the neighbor with morphological dependent state. The resulting configuration of cell states is composed of homogeneous regions whose boundaries are defined by the morphological independence relation.

- From the operational point of view we have generated a collection of hyperspectral images which can be used as benchmark for other hyperspectral image processing algorithms. The main advantage is the perfect knowledge of all its ground truth information and the realistic appearance of the generated images.

1.3 Publications produced during this PhD Thesis

1. M. Graña, J. Gallego (2003) *Associative Morphological Memories for Endmember Induction* in IGARSS'2003 Proceedings Vol. 6 pp. 3757 - 3759; IEEE Press; ISBN 0-7803-7930-6

2. M. Graña, J. Gallego (2003) *Associative morphological memories for spectral unminxing* in ESANN'2003, M. Verleysen (ed) pp. 481-486; dfacto press; Bruselas; ISBN 2-930307-03-x

3. M. Graña, J. Gallego (2003) *On the application of Associative Morphological Memories to Hyperspectral Image Analysis* in Artificial Neural Nets Problem Soving Methods (IWANN'2003) Parte II; LNCS 2687 pp. 567-574; Springer Verlag; ISBN 3-540-40211-x

4. M. Graña, J. Gallego (2003) *Hyperspectral image analysis with associative morphological memories* in ICIP'2003 Proceedings Vol. 3 pp. 549-52; IEEE Press; ISBN 0-7803-7751-6

5. M. Graña, J. Gallego, C. Hernandez (2003) *A single individual evolutionary strategy for endmember search in hyperspectral images* in JCIS 2003, 7th Joint Conf. on Information Sciences; pp. 363-366; Duke University press; ISBN 0-9707980-2-5

6. M. Graña, J. Gallego (2003) *More results on AMM for endmember induction* in Image and signal processing for remote sensing IX, Lorenzo Bruzzone (ed) pp. 316-327; SPIE Press vol 5238; ISBN 0-8194-5221-5

7. M. Graña, J. Gallego, C. Hernandez (2003) *Further results on AMM for endmember induction* in IEEE 2003 Workshop on Advances in Techniques for Analysis of Remotely Sensed Data, Lorenzo Bruzzone (ed) pp. 237-243 IEEE Press; ISBN 0-7803-8351-6

8. M. Graña, J. Gallego, C. Hernandez (2004) A Single Individual Evolutionary Strategy for Endmember Search in Hyperspectral Images. *Information Sciences, Int. J* 161(3-4):181-197

9. C. Hernández, J. Gallego, M. García-Sebastián, Manuel Graña Romay (2006) *On Clustering Performance Indices for Multispectral Image,* in Knowledge-Based Intelligent Information and Engineering Systems, 10 International Conf. – KES 2006, B. Gabrys, R. J. Howlett and L. C. Jain (Eds.) LNCS 4253, Springer Verlag, Berlin, KES 2006, Part III, pp. 277-283. ISBN 978-3-540-46542-3

10. C. Hernández, J. Gallego, M. Graña (2006) *On performance indices for unsupervised multispectral image classification* in IGARSS 2006; pp. 3907-3910 IEEE Press; ISBN 0-7803-9490-9

11. M. Graña, M. A. Veganzones, E. Irigoyen, J. Gallego (2010) Endmember based CBIR on hyperspectral image databases *Computers & Geosciences (submitted).*

12. J. Gallego, C. Hernandez, M. Graña (2010) A Morphological Cellular Automata based on Morphological Indepence *Logic Journal of the IGPL* (accepted)

1.4 Structure of the Thesis

Although we have not defined parts of the report, we can say that the first chapters, from Chapter 2 up to Chapter 5 provide background information, setting the theoretical framework for our works and defining the algorithms for endmember induction which are a central contribution of this thesis. The following chapters are devoted to validation and applications of these ideas. Therefore, Chapters 6 to 9 contain a Conclusion section that gives the particular conclusion and further work directions for this particular chapter. According to this structure, we have not included a final chapter devoted to conclusions which would be a mere repetition of these chapters' conclusions.

Chapter 2 contains the motivation and some background information on the PhD Thesis research topics.

Chapter 3 introduces the Linear Mixing Model and the Linear Unmixing as a subpixel resolution hyperspectral image analysis.

Chapter 4 contains the theoretical background on Associative Morphological Memories that supports the Endmember Induction Algorithm based on Morphological Independence.

Chapter 5 contains the description of an Endmember Induction Heuristic Algorithm based on Morphological Independence and Morphological Memories.

Chapter 6 contains the results of the application of the Endmember Induction Heuristic Algorithm on simulated hyperspectral images and some publicly available hyperspectral images.

Chapter 7 contains the description of a CBIR system based on spectral information for hyperspectral images.

Chapter 8 contains results on the MCA based on morphological independence for the segmentation of (color) images.

Appendix A contains the description of the synthetic hyperspectral images used in the computational validation experiments.

Appendix B contains the description of the public hyperspectral images used in the computational validation experiments.

Chapter 2

Background and Motivation

This chapter contains the motivations and some background to the works of this Ph.D. Section 2.1 introduces the hyperspectral images. Section 2.2 discusses the general approaches to hyperspectral image analysis and some comments on the validation issue. Section 2.3 introduces the Associative Morphological Memories. Section 2.4 comments on the use of fractional abundances as classification features. Section 2.5 introduces the problem of Content Based Image Retrieval in hyperspectral image databases. Section 2.6 introduces the Morphological Cellular Automata. Finally, section 2.7 introduces the Evolutionary Algorithms and their application to endmember induction.

2.1 Hyperspectral images

Hyperspectral images are a central topic of this Thesis from the point of view of application and materials used for the computational experiments. Hyperspectral images can be defined as images whose pixels contain a fine sampling of the light spectra. Therefore each pixel is a high dimensional vector, whose components are the received radiance values inside a fine wavelength band of the spectra. Most of the hyperspectral sensors cover the visible light spectrum and the near infrared (NIR) spectrum. In figure 2.1 we show the structure of a hyperspectral image from a computational point of view. It consists of a 3D matrix, whose third dimension corresponds to the radiance spectra sampled at the pixel. The two first dimensions correspond to the spatial coordiantes in the
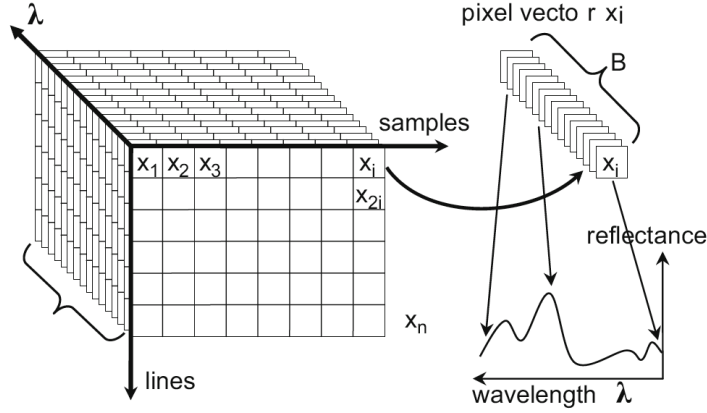
Figure 2.1: Structure of a hypespectral image

image plane. Another view of the data in a hyperspectral image is given in figure 2.2. In figure 2.3 we show an illustration of the hyperspectral iamge capture in a remote sensing setting. A high altitude device, either an airplane or a satelite, goes over the land picking the images. On board sensors often capture one line of the image, so that the motion of the device gives the second spatial dimension. The figure shows that different land covers produce different spectra in the corresponding image pixels. This additional spectral information has the promise of allowing image automated detection of materials highly efficient and robust without resorting to spatial processing [5, 11, 23, 43, 63, 84, 100, 101].

A central idea of this Thesis is that pixel spectra are in fact linear combination of elemental spectra called endmembers: the Linear Mixing Model (LMM) [52, 84]. The physical justification for this model is illustrated in figure 2.4. The model assumes that the land cover is composed of separated regions of different materials, however the resolution of the imaging sensor aggregates several covers inside each image pixel. The observed image pixel spectra is assumed to be a combination of the elementary spectra proportional to the fraction of pixel surface covered by each elementary material, thus the name of "fractional abundances" given to the linear combination coefficients.

8

▲ 3. Imaging spectrometry data cube illustrating the 3-D spatial and spectral character of the data.
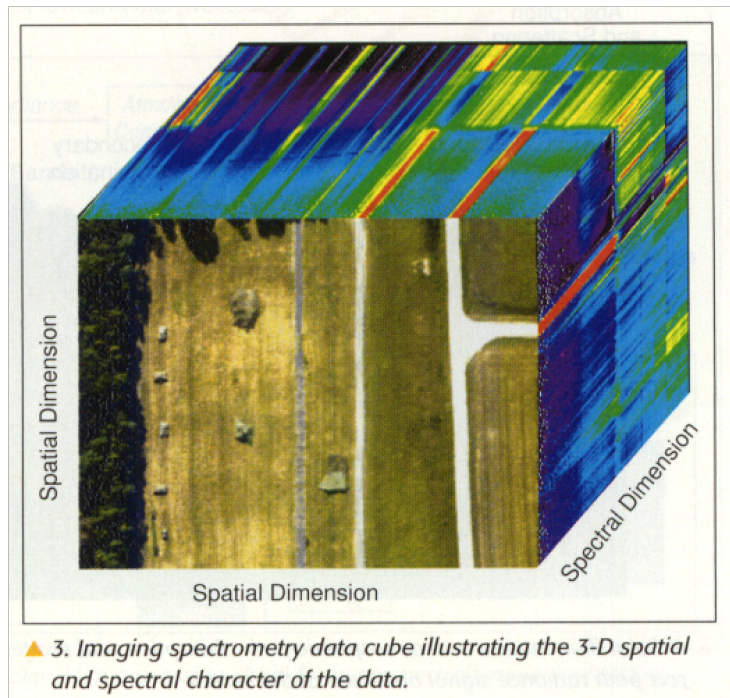
Figure 2.2: The hyperspectral image datacube

▲ 1. Principle of imaging spectroscopy.
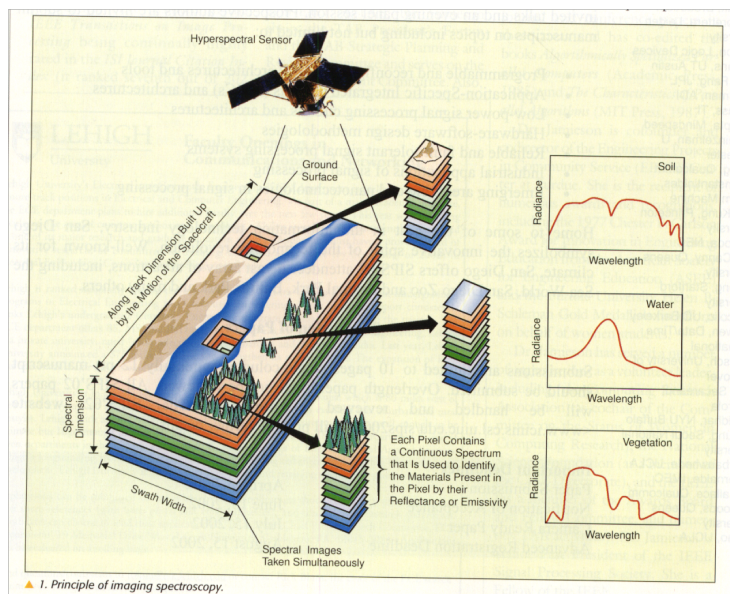
Figure 2.3: An illustration of the remote sensing hyperspectral image capture

9

(a)
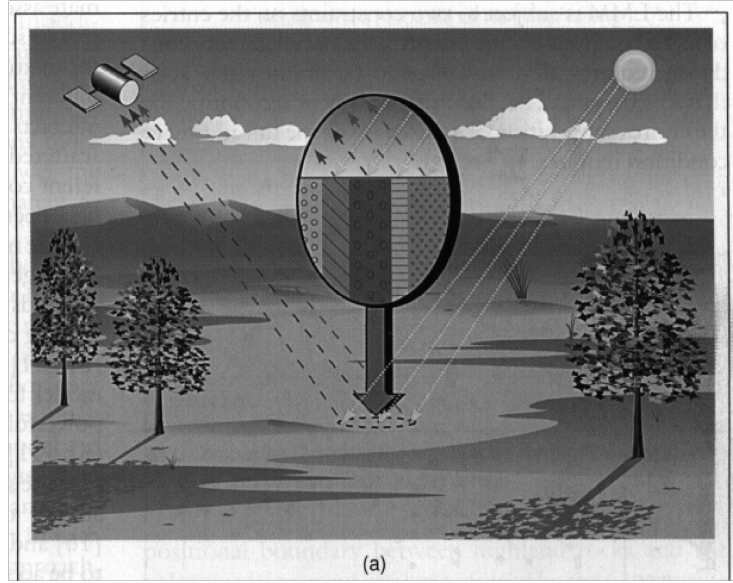
Figure 2.4: Linear Mixing as a product of imaging resolution

2.2 Hyperspectral image analysis

The goal of hyperspectral image analysis is the realization of a thematic map from the image data. A thematic map contains the labeling of the regions according to the materials in the land cover. If no precise information about the materials in the scene can be provided, the thematic map becomes a segmentation of the image. There are two basic strategies to build the the labeling of the image: supervised and unsupervised. The supervised approaches use available information on pixel classes in the image, to perform the classification of the remaining (label unknown) pixels.

The main drawback of supervised analysis and classification of hyperspectral remote sensing data is the difficulty in obtaining labeled sample data that can be trusted to the point of using it for quantitative evaluation. The scarcity of ground truth data has been recognized and specific training strategies have been devised to cope with this handicap [33, 100, 101]. The point of view assumed in this Thesis is that the efforts must be addressed to the unsupervised analysis and segmentation of the hyperspectral data to obtain salient image regions that may deserve further analysis and search for labeled data. In some applications, i.e. content based image retrieval, the goal is to navigate through a database

10

of images, so the system will require that all images are treated equal to obtain equivalent image features for the computation of similarity measures.

Some unsupervised segmentation attempts have been based on clustering algorithms, including competitive artificial neural networks related to the Self-Organizing Map (SOM) [68, 106]. The main inconvenience of these approaches is that they are guided by the data probability distribution, so they have a bias to ignore small features of the data or must be over-parameterized to model them. Therefore, it is difficult for them to detect and isolate small regions of the image with salient spectral features. In essence, SOM related algorithms are searching for data averages, while salient infrequent feature vectors are outliers of the data space.

We follow the general approach of linear filter target detection [64], inducing the filters from the image data. It is related to the "spectral unmixing" [52] image analysis paradigm. Ideally, hyperspectral images may allow the identification of materials in the image from the spectra of single pixels. However, image pixel spectra are frequently the result of a combination of spectra of elementary materials. We assume a linear mixing model, in which several basic materials (endmembers) are combined according to some abundance coefficients at each image pixel. In this model, the mixing linear coefficients have two constraints.

- The coefficients are positive, because negative contributions do not have physical meaning.

- The coefficients add up to one, because they correspond to a complete decomposition of the observed spectrum.

These conditions imply that the constituent materials, the endmembers, have a specific geometrical disposition: they are the vertices of a convex polygon convering the data points of the image in a high dimensional space [24].

Under this model, if the endmembers are given, it is possible to obtain a subpixel resolution material identification decomposing each pixel spectrum into their constituent material spectra. Spectral unmixing can be done by unconstrained least squares estimation or by some non-negative factorization algorithm, depending on the desired stress in complying with the basic assumptions of the linear mixing model. Taking its spatial distribution, the abundance coefficients may be visualized as abundance images, which give a description of material

11

distribution in the space. The computation of the abundance coefficients given a pixel spectra and a set of endmembers is the unmixing procedure. If the endmembers are given, the unmixing procedure is equivalent to the parallel detection of the spectral features represented by the endmembers (i.e.: materials). If the endmembers are unknown, we must induce them from the image data. Then, the unmixing procedure is unsupervised and may interpreted as an unsupervised segmentation of the image.

Therefore, the identification of such endmembers is a process of growing relevance in the hyperspectral image processing literature. Libraries of known pure ground spectra or laboratory observations were used in the early approaches. However, this approach has severe problems with varying illumination conditions, the diference of sensor intrinsic parameters, and the *a priori* knowledge about the material composition of the scene. Besides the methodological questions, this approach is not feasible when trying to process large quantities of image data. Current approaches try to induce the endmembers from the image data itself. The Endmember Induction Algorithms (EIA) either try to select some image pixel spectra as the best approximation to the endmembers in the image. There are several propositions in the literature for the extraction of the endmembers from the data, like the Convex Cone Analysis (CCA) method [46], the minimum volume transformations [24], the N-finder [109], extended morphological operators [69], or the fast pixel purity index [14], simulated annealing [67]. Some of thema have been evaluted in [70].

The works of this Thesis have dealt with two different approaches to the induction of the endmembers from the data. One stems from the works on the Associative Morphological Memories (AMM), the other from the field of Evolutionary Algorithms, more precisely Evolutionary Strategies. Both procedures are unsupervised. The first finds the number of endmembers depending on the setting of a variance related parameter, the second needs that the user specifies this number.

The AMM based procedure is based on the relation between morphological indepence and the convex polygon defined by the endmembers. The existence of this relation was an intuition that has been proved recently [84]. The algorithm was based on the selective sensitivity to noise of the AMM for the detection of the morphological independence conditions on the data. In its actual implementation it works in a single pass over the image, which is a desirable feature given the large computational cost of processing hyperspectral images.

12

The Evolutionary Strategy approach pursues the maximization of a fitness function that incorporates the objective of minimizing the error introduced by the unmixing process and the linear coefficient constraints. The main contribution, that will be commented later, is the formulation of a Michigan approach that is less computationally expensive and more effective.

2.2.1 The issue of algorithm validation

A critical aspect of the evaluation of algorithms applied to hyperspectral images is the lack of well-labeled test images. Benchmark images are roughly hand labeled, so on top of the noise in the images, the algorithms must dealt with the noise in the sample pixel labels. Besides, obtaining the images and performing an accurate pixel labeling is a costly and time-consuming process. The use of synthetic images allows the accurate validation of the algorithms and it is very economic and automatic. Most of the examples found in the literature up to now use simple hand designed spatial distributions of materials and linear combinations where additive noise is introduced to regulate the difficulty of the segmentation or identification problem. Our approach consists on the simulation of gaussian fields [55] to generate the abundance images, which are used to produce the linear mixing that gives the synthetic image. The covariance matrix parameters control the randomness of the resulting image, without resorting to the addition of noise. Although in this paper we present qualitative results on such an image, the approach leads easily to quantitative evalutations of the algorithms computing the correlation between the abundance images found by the algorithms and the original ones.

2.3 Associative Morphological Memories

In a short definition Morphological Neural Networks are equivalent computational constructions to the well know Artificial Neural Networks, with the specificity that their non-linearities are the maximum (Max) and/or minimum (Min) operators, which are the lattice theory basic operators. The Associative Morphological Memories (AMM) [85, 78, 80] are the morphological counterpart of the well known Hopfield Associative Memories [49]. AMM's are constructed as correlation matrices computed by either matrix Min- or Max-product, which are like the conventional matrix products in the algebra defined by the lattice

operators and the addition. Dual constructions can be made using the dual Min and Max operators. The AMM are selectively sensitive to specific types of noise (erosive and dilative noise). Memory recall is defined as a Min- or Max-product of the corresponding type of AMM.

The notion of morphological independence and strong morphological independence was introduced in [82] to study the construction of AMM exhibiting robustness against general noise, that is, simultaneous additive and erosive noise. It was established that AMM are able to robustly store and recall morphologically strongly independent sets of patterns. Applying an input to the AMM for recalling of a pattern morphologically dependent on one of the stored patterns gives the stored pattern. When the input pattern is morphologically independent of the stored patterns, the result of recall is a morphological polynomial on the stored patterns [97, 98]. In essence our procedure tests if the recalled pattern is different to the stored patterns to detect morphologically independent patterns.

In the context of this Thesis, the strong morphological independence has been a key concept to find endmembers in the hyperspectral images. We postulated that strog morphological independent vectors where in fact the vertices of a convex polytope which can be accepted as the endmembers in the image. Therefore, the algorithms developed used the AMM to detect morphological independence among pixel spectra.

2.4 Abundances as classification features

Linear feature extraction algorithms, like Principal Component Analysis (PCA) [35], Linear Discriminant Analysis (LDA) [35], Independent Component Analysis (ICA) [44] are defined as a linear transformation obtaining minimizing some criterion function, like the mean square error (PCA), a class separability criterion (LDA) or an independence criterion (ICA). Many classification approaches use the linear features for the construction of the classifier, obtaining an improved computational efficiency and accuracy. An alternative approach is to characterize the data through the vertices of a convex region that encloses it or most of it. The features extracted are the convex coordinates of the data points in this region. Therefore the dimensionality reduction depends on the degree of detail of the definition of this convex region: the number of vertices

that describe it.

In the context of hyperspectral image processing, the computation of the convex coordinates corresponds to the linear spectral unmixing of the image pixel spectra relative to a set of endmembers, assuming the LMM [52], in which several basic materials (endmembers) are combined according to some abundance coefficients at each image pixel. The computation of the abundance coefficients could be interpreted as a linear feature extraction algorithm or linear dimensional reduction algorithm. The induction of the endmembers from the data is performed by an unsupervised algorithm, the number of endmembers is not set *a priori*. Therefore its use as a feature extraction algorithm is an innovative method to combine unsupervised and supervised algorithms. We present in chapter 6 some results of this approach on hyperspectral image pixel classification.

2.5   Content Based Image Retrieval

The increasing amount of Earth Observation data provided by hyperspectral sensors, motivates research in some technological problems related with the scale of the available data, such as the scalability of paralel implementations of the analysis algorithms [71]. Content Based Image Retrieval (CBIR) [58, 61, 93] consist in the extraction of information from a query image in order to find similar images in a database. It is intended to allow for easy nagivation over huge databases. It has been applied to a number of image categories, such as medical images [13, 73, 110], using a wide variety of computational techniques [15, 17, 18, 19, 36, 48, 72, 25, 113, 114]. However, this problem has not been properly addressed for the case of remote sensing hyperspectral images. Approaches to CBIR in remote sensing images proposed up to now are focused on panchromatic or low dimension multispectral images such as LANDSAT [29, 32, 28, 30, 27, 90, 91]. There are few works in the literature dealing with hyperspectral images, and only [62, 105] deal explicitly with the spectral information to guide the search.

In CBIR systems, the images stored in the database are indexed by feature vectors extracted from the images by means of computer vision and digital image processing techniques. In the query-by-example approach, the interrogation to the database is done through the presentation of a query image, and the answer

are the most similar images in the database according to some similarity measure [93]. In the approach proposed in chapter 7 we use the endmembers induced from the database images by a predefined endmember induction algorithm as feature vectors. We define a dissimilarity measure between these feature vectors which can deal with the inherent asymmetries between the sets of ednmembers induced from the images. The aim is to declare as similar images that posses similar material spectral signatures regardles of its spatial distribution on the image, that is, we do not consider the spatial segmentation of the image. The dissimilarity is a function of the individual distances between endmembers from the images. We explore in chapter 7 the effect of using different endmember distances, Euclidean and Angular distances, and the use of different endmember induction algorithms. Specifically we test the N-FINDER [109] and an Incremental Lattice Independence Algorithm (ILIA) [37, 41] in the computational experiments performed over a large collection of synthetic hyperspectral images. Testing on synthetic datasets allows us to measure exactly the performance of the search and perform quantitative measurements, because the underlying ground thruth is know exactly. We have found that the approach is quite robust against changes in the endmember induction algorithm and endmember distance employed. In all cases, the precision and recall obtained suggest that the approach can be used in real life databases of hyperspectral images.

2.6   Morphological Cellular Automata

Cellular Neural Networks (CNN) are an specific class of Cellular Automata [26, 34, 53, 60, 87, 89, 94, 112]. Specifically, CNN have been applied to image processing and segmentation [20, 21, 22], however they are mostly restricted to one channel images. We intend to perform the extension this approach to multispectral images and to base this extension in morphological operators. Therefore, we propose in chapter 8 the application of morphological operators and properties arising from the work on Associative Morphological Memories (AMM) [86, 77, 81, 79, 83]. Morphological Cellular Neural Network (MCNN) provide a formal morphological extension to the CNN, consisting in using the AMM as the synaptic operators between neighboring cells. Though theoretically appealing, and possesing a really fast convergence, segmentation results are poor in practice. The goal is to provide a segmentation similar to the watershed algorithm [47, 107], which has had some difficulties in its generalization to

color and multispectral images [50, 92], because of the difficulties in definition of appropriate gradients. The MCNN is an attempt to reproduce the dynamical definition of CNN in morphological terms, with AMM as the state change operator. The system effectively converges to a configuration where each pixel is morphologically dependent of its neighbors, but this is a very weak condition to obtain perceivable homogenous regions, unless some labelling postprocess is imposed which must be based on some specific properties of morphologically dependent pixels still to be defined.

Maintaining the goal of obtaining a morphologically based image segmentation, performed by a collection of autonomous agents in the shape of a Cellular Automata, we shifted our attention from the operator (the AMM) to the property (morphological independence). That leads us to the idea of considering morphological dependence as a kind of equivalence relation. Pixel regions could be identified by being morphologically dependent on a given morphologically dominant vector, which is some kind of morphological region representative vector that can be found in the image. For the visual identification of the region, we can substitute all the morphologically dependent pixels by the morphologically dominant one. This in essence the working of the Morphological Cellular Automata (MCA) proposed and tested in chapter 8.

2.7   Evolutionary algorithms

In chapter 9 we study the application of evolutionary strategies to induce the endmember spectra from the data in the image. The goal was to obtain robust methods of endmember induction, insensitive to small variations in the algorithm paramters or the image characteristics. Elitist Evolutionary Strategies (ES) [9, 8, 10] are the class of algorithms that can be applied to the problema having the required global convergence properties ensuring the robustness of the algorithm. They have been applied to a wide spectra of problems in the literature, i.e. a small sample [3, 2, 12, 4, 16, 42, 51, 59, 1, 76, 88, 95]In the straightforward representation of the problem the population individuals are sets of endmembers and their fitness is related to some optimality criteria of the abundance images. That is, the objective function to be minimized is the combination of the reconstruction error of the image pixels and the satisfaction of the properties of a true abundance image: the full aditivity to one and non-negativity of all the abundance image pixels. The high computational cost of ES

motivates the proposition of a faster algorithm. The conventional ES follows the so called Pittsburg approach, where each populaiton individual models a complete solution to the problem. The evolutionary dynamics stablishes a competition between individuals looking for the best solution. The opposite view is sustained by the Michigan approach, where the whole population encodes a solution to the problem and the individuals must somehow cooperate to obtain the best solution. In our setting we propose to use the entire population as a single set of endmembers. Each individual is an endmember spectrum. Selection and mutation is performed over a singled out spectra, while the evaluation of a mutated individual relies in the improvement that it introduces in the global population fitness. The selection of the individual to be mutated needs of the definition of a local fitness function for each individual spectra in the set of hypothetical endmembers. We call this algorithm a Single Individual Evolution (SIE) strategy.

Chapter 3

Linear Mixing Model

This chapter introduces the Linear Mixing Model (LMM) that is a central concept in the work of this Thesis. The LMM is based on the knowledge of the endmembers, whose induction from the data is the subject of most of this Thesis. We introduce also in this chapter the competing approaches used in the validation of the computational results, including the linear feature extraction algorithms that do not perform an endmember induction. Section 3.1 gives the formal definition of LMM and the spectral unmmixing. Section 3.2 introduces the problem of endmember induction. Section 3.3 introduces the Independent Componenent Analysis (ICA) and Principal Component Analysis (PCA).

3.1 Spectral unmixing and the linear mixing model

The linear mixing model (LMM) [52] can be expressed as follows:

$$\mathbf{x} = \sum_{i=1}^{M} a_i \mathbf{s}_i + \mathbf{w} = \mathbf{S}\mathbf{a} + \mathbf{w}, \qquad (3.1)$$

where $\mathbf{x}$ is the d-dimension image pixel spectrum vector, $\mathbf{S}$ is the $d \times M$ matrix whose columns are the d-dimension endmembers $\mathbf{s}_i, i = 1, .., M$, $\mathbf{a}$ is the M-dimension fractional abundance vector, and $\mathbf{w}$ is the d-dimension additive

observation noise vector. The linear mixing model is subjected to two constraints on the abundance coefficients.

- First, to be physically meaningful, all abundance coefficients must be non-negative

$$a_i \geq 0, i = 1, .., M.$$

- Second, to account for the entire composition, they must be fully additive

$$\sum_{i=1}^{M} a_i = 1.$$

Once the endmembers have been determined, the unmixing process is the computation of the matrix inversion that gives the fractional abundance of each endmember in each pixel spectra and, therefore, the spectral unmixing. The simplest approach is the unconstrained least squared error estimation given by:

$$\widehat{\mathbf{a}} = \left(\mathbf{S}^T \mathbf{S} \right)^{-1} \mathbf{S}^T \mathbf{x}. \tag{3.2}$$

The abundance coefficients that result from this computation do not necessarily fulfill the non-negativity and full additivity conditions. It is possible to enforce each condition separately, but rather difficult to enforce both simultaneously [52]. However, as our aim is to obtain qualitative segmentations of the image the unconstrained estimation of equation (3.2) is convenient to compute the abundance images efficiently. When presenting visual results, we will scale and shift the abundance images to present them as grayscale images. This manipulation is intended to enhance the visualization but may introduce some deformation of the relative values of the abundance coefficients for the same pixel. Therefore, when computing the correlation between abundance images we proceed on the originally estimated images.

A final comment about the spectral unmixing: If we consider the normalized abundance coefficients, they can be assimilated to posterior probabilities of the classes represented by the endmembers. Therefore, the spectral unmixing can be assimilated to a classification procedure, that provides a soft segmentation of the hyperspectral image. If the endmembers are induced from the data without any a priory selection, the procedure is an unsupervised soft segmentation of the image.

As a measure of the quality of the spectral unmixing obtained it is useful to introduce the reconstruction error:

$$\varepsilon^2 = \|\mathbf{x} - \mathbf{S}\widehat{\mathbf{a}}\|^2.$$ (3.3)

This measure will be used in the fitness functions of the evolutionary strategies in chapter 9.

3.2 Endmember induction

Once stated the LMM, a key issue is the determination of the endmembers wich compose the basis for the linear decomposition of the data. Early approaches to endmember determination were based on human expertise. The prior knowledge about the contents of the imaged terrain was used by the expert to select some candidate endmember spectra from a provided library. The spectra in the library must come from the same sensor, in order to perform the matching and unmixing. This approach is not feasible when trying to process large quantities of image data. Current approaches try to induce the endmembers from the image itself. Recent reviews are [70] which makes some emphasis on the degree of automation to classify the algorithms, and [104] whose emphasis is on the computational foundations, assuming that user interaction must be minimal or null. We distinguish three fundamental approaches: *Geometric approaches*, that try to find a simplex that covers the image data; *Lattice Computing approaches*, that use some kind of lattice theoretic formalism or mathematical morphology approach; and, *Heuristic approaches*, that are not very rigorously formalized under a theoretical framework.

The first significant work on the automated induction of endmembers from image data is [24], which starts with the observation that the scatter plots of remotely sensed data are tear shaped or pyramidal, if two or three spectral bands are considered. The apex lies in the so-called dark point. The endmember detection becomes the search for non-orthogonal planes that enclose the data defining a minimum volume simplex, hence the name of the method. The method is computationally expensive and requires the prior specification of the number of endmenbers. A recent approach to the automatic endmember detection is the Convex Cone Analysis (CCA) method proposed in [46] and applied to target detection. The CCA selects the greatest eigenvalue eigenvectors, as many

21

as the specified number of endmembers. These eigenvectors define the basis of the convex cone that covers the image data. The vertices of the convex cone correspond to spectra with as many zero elements as the number of eigenvectors minus one. The search for the convex cone vertices involves the exploration of the combination of bands and the solution of a linear system for each combination. The complexity of the search for these vertices is $O\left(b^c\right)$ where b is the number of bands and c the number of eigenvectors. At present we use a raw random search for the experimental result in the experiment below. Another approach is the modelling by Markov Random Fields and the detection of spatially consistent regions whose spectra will be assumed as endmembers [75]. An approach based on mathematical morphology in [69] involves the recursive morphological filtering of image windows of increasing size to obtain progressively pure endmember representatives. The erosion and dilation operators are based on the local window statistics (average and eccentricity). In the following, we present a brief review of the CCA and N-FINDER algorithms used on the computational experiments to compare with our own proposed algorithms presented in chapter 5.

3.2.1   The Convex Cone Analysis (CCA)

The CCA was proposed by [46]. The basic idea is that after performing a PCA of the spectral correlation matrix, the data falls in a cone shaped region in the positive subspace centered in the first eigenvector. Given the $N \times M \times D$ hyperspectral image, it is reorganized as a $NM \times D$ matrix $\mathbf{S}$. The spectral correlation matrix is computed as

$$\mathbf{C} = \mathbf{S}^T \mathbf{S}.$$

Let it be $\mathbf{C} = \mathbf{PLP}^T$ the PCA decomposition of the correlation matrix, select the first c eigenvectors $[\mathbf{p}_1, .., \mathbf{p}_c] = \mathbf{P}_c$ and search for the boundaries of the convex region characterized by

$$\mathbf{x} = \mathbf{p}_1 + a_1 \mathbf{p}_2 + .. + \mathbf{a}_{c-1} \mathbf{p}_c \geq \mathbf{0}.$$

The vertices of this region are the points with exactly $c - 1$ zero components. The CCA algorithm searches among all the $\binom{b}{c-1}$ possible combinations of eigen-

---
Algorithm 3.1 N-FINDER algorithm
---
1. Apply Principal Component Analysis (PCA) to reduce the data dimensionality. Keep the first $p - 1$ principal components to acumulate up to 99% of variance.

2. Randomly select p vectors from the data to initialize the set of induced endmembers E.

3. Calculate the volume of the simplex $v = V(E)$ (3.5). $v_{actual} = v$.

4. For each endmember $\mathbf{e}_k; k = 1, \ldots p$:

    (a) For each data vector $\mathbf{f}(i) : i = 1, .., N$:

        i. Form a new matrix E' by substituting the endmember $\mathbf{e}_k$ by the data vector $\mathbf{f}(i)$.
        ii. Calculate the volume of the simplex $v' = V(E')$.
        iii. If $v' > v_{actual}$ then E' becomes E. $v_{actual} = v'$.

5. If $v_{actual} > v$ then $v = v_{actual}$. Go to step 4.

---

vectors performing the following test. Let it be

$$[\mathbf{p}(\gamma_1), .., \mathbf{p}(\gamma_{c-1})] = \mathbf{P}'$$

the selected set of eigenvectors. Solve the set of equations

$$\mathbf{P}'\mathbf{a} = \mathbf{0}$$

and compute

$$\mathbf{x} = \mathbf{P}_c\mathbf{a}.$$

If $\mathbf{x}$ has exactly $c - 1$ zero components then it is a vertex of the convex region data. In practice, each component is tested against a threshold. However, as the combinatorial space grows the problem becomes intractable. We implemented an straightforward random search. Application of more sophisticated random search algorithms like genetic algorithms may be of interest for large problems. The CCA algorithm provides the endmembers that may be used to compute the abundance images.

3.2.2 N-FINDER

The N-FINDER algorithm was introduced in [109], it is presented in Algorithm 3.1). Algorithm N-FINDER works by growing a simplex inside the data, beginning with a random set of pixels. Previously, data dimensionality has to be reduced to $p-1$ dimensions, being p the number of endmembers searched for.

Let E be the matrix of endmembers augmented with a row of ones

$$E = \begin{bmatrix} 1 & 1 & \ldots & 1 \\ \mathbf{e_1} & \mathbf{e_2} & \ldots & \mathbf{e}_p \end{bmatrix} \tag{3.4}$$

where $\mathbf{e}_i$ is a column vector containing the spectra of the i-th endmember. The volume of the simplex defined by the endmembers is proportional to the determinant of E

$$V(E) = \frac{abs(\det(E))}{(p-1)!} \tag{3.5}$$

The algorithm starts by selecting an initial random set of pixels as endmembers. Then for each pixel and each endmember, the endmember is replaced with the spectrum of the pixel and the volume recalculated by 3.5. If the volume of the new simplex increases, the endmember is replaced by the spectrum of the pixel. The procedure ends when no more replacements are done. The algorithm needs of some random initializations to avoid local maxima.

3.3 Linear feature extraction: ICA and PCA

The Independent Component Analysis (ICA) [44] assumes that the data is a linear combination of nongaussian, mutually independent latent variables with an unknown mixing matrix. The ICA reveals the hidden independent sources and the mixing matrix. That is, given a set of observations represented by a D dimensional vector $\mathbf{x}$, ICA assumes a generative model

$$\mathbf{x} = \mathbf{As},$$

where $\mathbf{s}$ is the M dimensional vector of independent sources and $\mathbf{A}$ is the $D \times M$ unknown basis matrix. Then, ICA searches for the linear transformation of the

data $\mathbf{W}$, such that the projected variables

$$\mathbf{Wx} = \mathbf{s}$$

are as independent as possible. It has been shown that the model is completely identifiable if the sources are statistically independent and at least $M - 1$ of them are non gaussian. If the sources are gaussian the ICA transformation could be estimated up to an orthogonal transformation. Estimation of mixing and unmixing matrices can be done maximizing diverse objective functions, among them the non gaussianity of the sources and the likelihood of the sample. For the computational experiments, we have used the FastICA [44, 45] algorithm available at http://www.cis.hut. /projects/ica/fastica. To apply it we did reshape the hyperspectral images so that each band becomes a data vector. The basis of vectors that specify the linear tranformation, equivalent to our endmembers, are the columns of the estimated mixing matrix $\mathbf{W}$, and the estimated abundance coefficients are the independent sources $\mathbf{s}$. Obviously, the number of independent sources M searched for is equivalent to the number of endmembers, and D is the number of spectral bands.

The Principal Component Analysis (PCA) [35] is a well-known linear dimension reduction procedure that has been proved to be optimal in the sense of the mean squared error. It consists in the selection of the largest eigenvalue eigenvectors of the data covariance matrix. These eigenvectors constitute the transformation matrix. The selection of the number of eigenvectors or the independent components can be made attending to some quantitative criteria, but in our experiment below we selected the number of components in the ground truth image. Eigenvectors are equivalent to the endmembers, and the linear coefficients of the PCA projection are the corresponding

Chapter 4

AMM and Morphological Independence

The Associative Morphological Memories (AMM) [86, 77, 97, 98, 83] are the morphological counterpart of the well known Hopfield Associative Memories [49]. Dual AMM's are constructed as correlation matrices computed by either one of the dual matrix Min- or Max-product. The AMM are selectively sensitive to specific types of noise (erosive and dilative noise). The notion of morphological independence and morphological strong independence was introduced in [83] to study the construction of AMM robust to general noise. It was established that AMM are able to robustly store and recall morphologically strongly independent sets of patterns. Applying an input to the AMM for recalling of a pattern morphologically dependent on one of the stored patterns gives the stored pattern. When the input pattern is morphologically independent of the stored patterns, the result of recall is a morphological polynomial on the stored patterns [98]. These results set the stage for the definition in chapter 5 of our procedure for endmember induction, which tests if the recalled pattern is different to the stored patterns to detect morphologically independent patterns.

Section 4.1 gives the basic definitions of AMM. Section 4.2 introduces the effect of noise in AMM. Section 4.3 introduces the morphological independence. Section 4.4 presents the relation between strong lattice indepencende and affine independence. Section 4.5 gives the reason why our algorithms in chapter 5 are defeined on binary AMMs.

4.1 Associative Morphological Memories

The work on Associative Morphological Memories stems from the consideration of partially ordered ring $(\mathbb{R}, \vee, \wedge, +)$ instead of the algebraic ring $(\mathbb{R}, +, \cdot)$ as the computational framework for the definition of Neural Networks computation [86, 77]. The operators $\vee$ and $\wedge$ denote, respectively, the max and min operators, which correspond to the morphological dilation and erosion operators, respectively. Given a set of input/output pairs of pattern $(X, Y) = \left\{ \left(\mathbf{x}^{\xi}, \mathbf{y}^{\xi} \right); \xi = 1, .., k \right\}$, a linear heteroassociative neural network based on the pattern's cross correlation [49] is built up as

$$W = \sum_{\xi} \mathbf{y}^{\xi} \cdot \left(\mathbf{x}^{\xi} \right)'.$$

Recall of an stored output pattern is achieved by the multiplication of the input pattern with memory:

$$\widehat{\mathbf{y}^{\xi}} = W \mathbf{x}^{\xi}.$$

When the recalled pattern is identical to the stored one, i.e. $\widehat{\mathbf{y}^{\xi}} = \mathbf{y}^{\xi}$, then we have perfect recall. The robustness of the memory consists in its ability to recall good approximations of the stored pattern even when the input pattern is distorted by noise.

Mimicking this construction procedure [86, 77] propose the following constructions of Heteroassociative Morphological Memories (HMM's), the erosive HMM:

$$W_{XY} = \bigwedge_{\xi=1}^{k} \left[\mathbf{y}^{\xi} \times \left(-\mathbf{x}^{\xi} \right)' \right] \tag{4.1}$$

and the dilative HMM:

$$M_{XY} = \bigvee_{\xi=1}^{k} \left[\mathbf{y}^{\xi} \times \left(-\mathbf{x}^{\xi} \right)' \right], \tag{4.2}$$

where $\times$ is any of the $\boxdot$ or $\boxdot$ operators. Here $\boxdot$ and $\boxdot$ denote the matrix max- and min-product, respectively defined as follows:

$$C = A \boxdot B = [c_{ij}] \Leftrightarrow c_{ij} = \bigvee_{k=1..n} \{ a_{ik} + b_{kj} \}, \tag{4.3}$$

$$C = A \boxtimes B = [c_{ij}] \Leftrightarrow c_{ij} = \bigwedge_{k=1..n} \{a_{ik} + b_{kj}\}. \tag{4.4}$$

The recall operation is performed applying these morpholgical matrix products, that is,

$$\widehat{\mathbf{y}^{\xi}} = W_{XY} \boxtimes \mathbf{x}^{\xi}.$$

or

$$\widehat{\mathbf{y}^{\xi}} = M_{XY} \boxtimes \mathbf{x}^{\xi}.$$

If $X = Y$ then the HMM memories are Autoassociative Morphological Memories (AMM). Conditions of perfect recall by the HMM's and AMM's of the stored patterns are proved in [86, 77]. In the continuous case, the AMM's are able to store and recall any set of patterns, that is:

$$W_{XX} \boxtimes \mathbf{x} = \mathbf{x} = M_{XX} \boxtimes \mathbf{x}, \ \forall \mathbf{x} \in X, \tag{4.5}$$

which can be stated in compact form as follows:

$$W_{XX} \boxtimes X = X = M_{XX} \boxtimes X, \tag{4.6}$$

for any X.

That is, AMMs possess *perfect recall* for noiseless patterns [86, 77]. It is also interesting to note that if we iterate the memory recall we obtain a fixed point very fast, in fact it is obtained at the second iteration:

$$W_{XX} \boxtimes \mathbf{z} = \mathbf{v} \Rightarrow W_{XX} \boxtimes \mathbf{v} = \mathbf{v}, \tag{4.7}$$

$$M_{XX} \boxtimes \mathbf{z} = \mathbf{u} \Rightarrow M_{XX} \boxtimes \mathbf{u} = \mathbf{u}. \tag{4.8}$$

The set of fixed points $F(X)$ of the morphological memories constructed from the set of patterns X is the same for both types of AMM:

$$F(X) = \{\mathbf{x} \mid W_{XX} \boxtimes \mathbf{x} = \mathbf{x}\} = \{\mathbf{x} \mid M_{XX} \boxtimes \mathbf{x} = \mathbf{x}\}.$$

4.2 Noise in AMM

The perfect recall results hold when we try to recover the output patterns from the noise-free input pattern. Let it be $\widetilde{\mathbf{x}}^\gamma$ a noisy version of $\mathbf{x}^\gamma$. Two kinds of noise can be distinguished from the morphological point of view:

- Erosive noise: If $\widetilde{\mathbf{x}}^\gamma \leq \mathbf{x}^\gamma$ then $\widetilde{\mathbf{x}}^\gamma$ is an eroded version of $\mathbf{x}^\gamma$, alternatively we say that $\widetilde{\mathbf{x}}^\gamma$ is corrupted by erosive noise.

- Dilative noise: If $\widetilde{\mathbf{x}}^\gamma \geq \mathbf{x}^\gamma$ then $\widetilde{\mathbf{x}}^\gamma$ is a dilated version of $\mathbf{x}^\gamma$, alternatively we say that $\widetilde{\mathbf{x}}^\gamma$ is corrupted by dilative noise.

Morphological memories are selectively sensitive to these kinds of noise. The conditions of *robust* perfect recall [86, 77] are on the basis of the proposed endmember induction algorithms. Given a set of patterns X, the equality

$$W_{XX} \boxdot \widetilde{\mathbf{x}}^\gamma = \mathbf{x}^\gamma \tag{4.9}$$

holds when the noise affecting the pattern is erosive $\widetilde{\mathbf{x}}^\gamma \leq \mathbf{x}^\gamma$ and the following relation holds:

$$\forall i \exists j_i; \widetilde{x}_{j_i}^\gamma = x_{j_i}^\gamma \vee \left(\bigvee_{\xi \neq \gamma} \left(x_i^\gamma - x_i^\xi + x_{j_i}^\xi \right) \right). \tag{4.10}$$

Similarly, the equality

$$M_{XY} \boxdot \widetilde{\mathbf{x}}^\gamma = \mathbf{x}^\gamma \tag{4.11}$$

holds when the noise affecting the pattern is dilative $\widetilde{\mathbf{x}}^\gamma \geq \mathbf{x}^\gamma$ and the following relation holds:

$$\forall i \exists j_i; \widetilde{x}_{j_i}^\gamma = x_{j_i}^\gamma \wedge \left(\bigwedge_{\xi \neq \gamma} \left(x_i^\gamma - x_i^\xi + x_{j_i}^\xi \right) \right). \tag{4.12}$$

Therefore, the AMM will systematically fail to recall the pattern if the noise is a mixture of erosive and dilative noise.

4.3 Morphological independence

To obtain general noise robustness [74], some works proposed the kernel method and some enhancements [77, 83]. Related to the construction of the kernels, [83] introduced the notion of morphological independence. Here we distinguish erosive and dilative versions of this definition. Given vectors $\mathbf{x}, \mathbf{y} \in \mathbb{R}^d$, $\mathbf{y}$ is morphologically *dependent* in the *erosive* sense of $\mathbf{x}$ if $\mathbf{y} \leq \mathbf{x}$, $\mathbf{y}$ is morphologically *dependent* in the *dilative* sense of $\mathbf{x}$ if $\mathbf{y} \geq \mathbf{x}$. In both cases, we say that $\mathbf{x}$ is dominant. Given a set of pattern vectors $X = \left(\mathbf{x}^1, ..., \mathbf{x}^k \right)$, a pattern vector $\mathbf{y}$ of the same dimensionality is

- Morphologically independent of X in the erosive sense if $\mathbf{y} \nleq \mathbf{x}^\gamma; \gamma = \{1, .., k\}$, and

- Morphologically independent of X in the dilative sense if $\mathbf{y} \ngeq \mathbf{x}^\gamma; \gamma = \{1, .., k\}$.

The set of pattern vectors X is said to be morphologically independent in either sense when all the patterns are morphologically independent of the remaining patterns in the set. For the endmember induction application we want to use AMM as detectors of the of morphological independent vectors which correspond to the set of extreme points, to obtain a rough approximation of the minimal simplex that covers the data points. We note that given a set of pattern vectors $X = \left(\mathbf{x}^1, ..., \mathbf{x}^k \right)$, and the erosive W_{XX} and dilative M_{XX} memories constructed from it, and a test pattern $\mathbf{y} \notin X$, if $\mathbf{y}$ is morphologically independent of X in the erosive sense, then $W_{XX} \boxtimes \mathbf{y} \notin X$. Also, if $\mathbf{y}$ is morphologically independent of X in the dilative sense, then $M_{XX} \boxtimes \mathbf{y} \notin X$. Therefore the AMM's can be used as detectors of morphological independence.

Morphological independence has been generalized to lattice independence in recent works [79, 81] stablishing its relation with affine independence. This equivalence is very useful for the induction of endmembers from data for linear unmixing processes [40, 38]. A vector $\mathbf{x}$ is lattice dependent on the set X if it can be expressed as a linear minimax combination of the X :

$$\mathbf{x} = \bigvee_{j \in J} \bigwedge_{\gamma=1}^{k} \left(a_{\gamma j} + \mathbf{x}^\gamma \right). \tag{4.13}$$

It is important to note [79] that a vector $\mathbf{x}$ is a fixed point of the erosive W_{XX} and dilative M_{XX} memories if and only if it is lattice dependent on X. In other words, $F(X)$ is composed of the vectors that are lattice dependent on X.

4.4 Lattice independence and Affine Independence

It has been shown [79, 96] that given a set of vectors $X = \left\{ \mathbf{x}^1, ..., \mathbf{x}^k \right\} \subset \mathbb{R}^n$, a vector $\mathbf{y} \in \mathbb{R}^n_{\pm\infty}$ is a fixed point of W_{XX}, that is $W_{XX} \boxtimes \mathbf{y} = \mathbf{y}$, if and only if $\mathbf{y}$ is lattice dependent on X.

A set of vectors $X = \left\{ \mathbf{x}^1, ..., \mathbf{x}^k \right\} \subset \mathbb{R}^n$ is said to be *max dominant* if and only if for every $\lambda \in \{1, ..., k\}$ there exists and index $j_\lambda \in \{1, ..., n\}$ such that

$$ x^\lambda_{j_\lambda} - x^\lambda_i = \bigvee_{\xi=1}^{k} \left(x^\xi_{j_\lambda} - x^\xi_i \right) \forall i \in \{1, ..., n\}. $$

Similarly, X is said to be *min dominant* if and only if for every $\lambda \in \{1, ..., k\}$ there exists and index $j_\lambda \in \{1, ..., n\}$ such that

$$ x^\lambda_{j_\lambda} - x^\lambda_i = \bigwedge_{\xi=1}^{k} \left(x^\xi_{j_\lambda} - x^\xi_i \right) \forall i \in \{1, ..., n\}. $$

These expressions are identical to the ones given above for the robust recall of noisy patterns. Their value as an identifiable property of the data has been discovered in the context of the formalization of the relationship between strong lattice independence, defined below, and the affine independence in the classical linear analysis.

A set of lattice independent vectors $\left\{ \mathbf{x}^1, ..., \mathbf{x}^k \right\} \subset \mathbb{R}^n$ is said to be *strongly lattice independent* (SLI) if and only if X is max dominant or min dominant or both.

As said before, min and max dominance are the conditions for perfect recall. Per construction, the column vectors of Lattice Autoassociative Memories are diagonally min or max dominant, depending of their erosive or dilative nature, therefore they will be strong lattice independent, *if* they are lattice independent.

In [81] it has been proven that if $X = \left\{ \mathbf{x}^1, ..., \mathbf{x}^k \right\} \subset \mathbb{R}^n$ is strongly lattice independent then X is affinely independent. This result is the key result relating

32

the linear convex analysis and the non-linear morphological/lattice analysis. Building sets of strongly morphological/lattice independent vectors allows to assume them as affine independent vertices of a convex polytope covering the data.

4.5   Rationale for the use of binary AMM

The endmembers that we are searching for define a high dimensional box centered at the origin of the high dimensional space (the data mean is shifted to the origin). They are morphologically independent vectors both in the erosive and dilative senses, and they enclose the remaining vectors. Working with integer valued vectors, given a set of pattern vectors $X = \left(\mathbf{x}^1, ..., \mathbf{x}^k\right)$ and the erosive W_{XX} and dilative M_{XX} memories constructed from it, if a test pattern $\mathbf{y} < \mathbf{x}^\gamma$ for some $\gamma \in \{1, .., k\}$ then $W_{XX} \boxtimes \mathbf{y} \notin X$. Also, if the test pattern $\mathbf{y} > \mathbf{x}^\gamma$ for some $\gamma \in \{1, .., k\}$ then $M_{XX} \boxtimes \mathbf{y} \notin X$. Therefore, working with integer valued patterns the AMM will be useless for the detection of morphologically independent patterns. However, if we consider the binary vectors obtained as the sign of the vector components, then morphological independence can be detected as suggested above: The already detected endmembers are used to build the erosive and dilative AMM. If the output recalled by a new pattern does not coincide with any of the endmembers, then the new pattern is a new endmember.

33

Chapter 5

The AMM-based endmember induction algorithm

We present in this chapter our computational procedure for the induction of endmembers from hyperspectral image for spectral unmixing. This procedure makes profit of the selective noise sensitivity of the Associative Morphological Memories (AMM) to detect the morphological independence conditions that are a necessary condition of endmember spectra. We present to equivalent versions of the algorithm. The first is called Endmember Induction Heuristic Algorithm (EIHA) corresponds to the earlier formulations when the theory underlying the approach was not stablished. This algorithm was used to obtain the results in chapter 6. The second is called Incremental Lattice Independent Algorithm (ILIA) following a more recent notation. It has been used for the CBIR experiments in chapter 7. Both algorithms work in a single pass over the image, which is a desirable feature given the large computational cost of processing hyperspectral images. The procedure is unsupervised and does not need the explicit setting of the number of endmembers searched for.

Section 5.2 describes the EIHA algorithm. Section 5.3 describes the ILIA version of the algorithm.

5.1 Notation

We denote by $\left\{ \mathbf{f}\left(i,j\right) \in \mathbb{R}^d; i=1,..,n; j=1,..,m \right\}$ the multispectral or hyperspectral image whose pixels are d-dimensional vector.

We denote $\boldsymbol{\mu}$ and $\boldsymbol{\sigma}$ the d-dimensional vectors containing the the mean and standard deviations of each pixel component computed over the image, that is

$$\boldsymbol{\mu}_k = \frac{1}{n \cdot m} \sum_{i,j} \mathbf{f}_k\left(i,j\right),$$

$$\boldsymbol{\sigma}_k = \frac{1}{n \cdot m} \sum_{i,j} \left(\mathbf{f}_k\left(i,j\right) - \boldsymbol{\mu}_k\right)^2 .$$

We denote by α a tuning sensitivity parameter for the selection of endmembers. This parameter filters out the pixels that are considered as random perturbation of the already detected endmembers. The vector interval that is considered as a perturbation is defined by the addition and subtraction of $\alpha \boldsymbol{\sigma}$. Therefore, we assume some kind of normal distribution model of the data around each endmember. Lowering α we allow for more endmembers to be discovered, bigger values of α impose greater limitations to test pixels as candidate endmembers thus lowering the number of endmembers discovered.

We denote by $E = \{\mathbf{e}_1, \mathbf{e}_2, \ldots, \mathbf{e}_p\}$ the set of endmembers induced by the algorithm.

The sign function $\text{sign} : \mathbb{R}^d \rightarrow \{0,1\}^d$ returns a binary vector corresponding to the sign of each component of the input. Let it be $\mathbf{b} = \text{sign}\left(\mathbf{x}\right)$, then the function is characterized by:

$$b_i = \left\{ \begin{array}{ll} 1 & x_i > 0 \\ 0 & x_i \leq 0 \end{array} \right. .$$

5.2 EIHA

The Endmember Induction Heuristic Algorithm (EIHA) starts by computing the zero mean image, that is obtained by substracting the pixel spectra mean from all the image pixels. This shifted image will allow the identification of the space partitions relative to the mean. The set of endmembers is initialized picking a pixel spectrum at random (it can be the first pixel in the image). The

---

Algorithm 5.1 Endmember Induction Heuristic Algorithm
___
1. Compute the zero mean image
   $\{\mathbf{f}^c(i,j) = \mathbf{f}(i,j) - \boldsymbol{\mu}; i = 1, .., n; j = 1, .., m\}$.

2. Initialize the set of endmembers $E = \{\mathbf{e}_1\}$ with a pixel spectrum $\mathbf{e}_1 = \mathbf{f}^c(i^*, j^*)$ randomly picked from the image. Initialize the set of morphologically independent binary signatures $X = \{\mathbf{x}_1\}$ with $\mathbf{x}_1 = \text{sign}(\mathbf{e}_1)$.

3. Construct the AMM's based on the morphologically independent binary signatures: M_{XX} and W_{XX}.

4. For each pixel $\mathbf{f}^c(i,j)$

   (a) compute the vector of the signs of the Gaussian noise corrections $\mathbf{f}^+(i,j) = \text{sign}(\mathbf{f}^c(i,j) + \alpha\boldsymbol{\sigma})$ and $\mathbf{f}^-(i,j) = \text{sign}(\mathbf{f}^c(i,j) - \alpha\boldsymbol{\sigma})$

   (b) compute $\mathbf{y}^+ = M_{XX} \boxtimes \mathbf{f}^+(i,j)$

   (c) compute $\mathbf{y}^- = W_{XX} \boxtimes \mathbf{f}^-(i,j)$

   (d) if $\mathbf{y}^+ \notin X$ or $\mathbf{y}^- \notin X$ then $\mathbf{f}^c(i,j)$ is a new endmember to be added to E, go to step 3 and resume the exploration of the image.

   (e) if $\mathbf{y}^+ \in X$ and $\mathbf{f}^c(i,j) > \mathbf{e}_{\mathbf{y}+}$, then the current pixel spectral signature is more extreme than the stored endmember, then substitute $\mathbf{e}_{\mathbf{y}+}$ with $\mathbf{f}^c(i,j)$.

   (f) if $\mathbf{y}^- \in X$ and $\mathbf{f}^c(i,j) < \mathbf{e}_{\mathbf{y}-}$ then the current pixel is more extreme than the stored endmember, then substitute $\mathbf{e}_{\mathbf{y}-}$ with $\mathbf{f}^c(i,j)$.

5. The final set of endmembers is the set of original spectral signatures $\mathbf{f}(i,j)$ of the pixels selected as members of E.

---

algorithm keeps for each endmember its signature, consisiting on its sign. The endmembers' signatures X will be used to detect morphologically independent vectors that give the first condition about the strong morphological independence of the endmembers, required to be affinely independent. Therefore, the algorithm computes the signature of the first found endmember. The endmembers' signatures are the basis vectors to compute the erosive and dilative AMM M_{XX} and W_{XX} used to detect the morphological independence.

The algorithm proceeds testing each image pixel as follows. First computes the signatures (the sign) of the upper and lower bound of the allowable perturbations of the pixel, adding and substracting $\alpha\boldsymbol{\sigma}$. These signatures are applied to the erosive and dilative morphological memories respectively obtaining recall vectors $\mathbf{y}^+$ and $\mathbf{y}^-$, respectively. If one or both of these vectors do not belong to the set of signatures X then a new endmember has been found, which is added to the set E and its signature is added to X.

If the recalled signatures belong to X means that there is an identified endmember in this quadrant of the spectral space, nevertheless we test if the current pixel is further away from the data mean than the considered extreme. We denote $\mathbf{e_{y+}}$ the endmember vector whose signature is $\mathbf{y}^+$.

The algorithm returns the original spectra (before shifting to zero mean) of the detected endmembers. The endmembers correspond to separate spectral space quadrants about the mean of the data, and are the most extreme spectrum found in this quadrant. The steps in the procedure are shown in the Algorithm 5.1

5.3   ILIA

The ILIA is an evolved formulation of the Endmember Induction Heuristic Algorithmm (EIHA). This approach is based on the recent theoretical results showing that Strong Lattice Independent (SLI) sets of vectors are Affine Independendent [79, 81], and, thus, can be interpreted as a collection of endmembers for the analysis of hyperspectral data. This theoretical results confirms the intuition behind EIHA, allowing a more clear formulation. The SLI involves two conditions: Lattice Independence and max/min dominance. Lattice Independence is detected based on results on fixed points for Lattice Autoassociative Memories (LAM) [74, 81, 96]. A lattice dependent vector will be a fixed point of anyone of the

Algorithm 5.2 A LAAM based Incremental Lattice Independence Algorithm (ILIA) for the induction of endmembers

1. Shift the data sample substracting $\bar{\mathbf{f}}$ the mean of the image pixels' spectra $\left\{\mathbf{f}^c\left(i\right) = \mathbf{f}\left(i\right) - \bar{\mathbf{f}}; i = 1, .., n\right\}$.

2. Initialize the set of endmembers $E = \left\{\mathbf{e}_1 = \mathbf{f}^c\left(i^*\right)\right\}$ where i^* is a randomly picked sample index. The initial set of endmember sample indices is $I = \left\{i^*\right\}$.

3. Construct the LAAM's based on the set of endmembers: M_{EE}.

4. For each input image feature vector $\mathbf{f}^c\left(i\right)$

   (a) If there is any $\mathbf{e} \in E$ such that $\forall j : \left\|f^c_j\left(i\right) - e_j\right\| < \alpha\sigma_j$ discard $\mathbf{f}^c\left(i\right)$, otherwise proceed to test SLI

   (b) If $\mathbf{f}^c\left(i\right) = M_{EE} \boxtimes \mathbf{f}^c\left(i\right)$ then discard $\mathbf{f}^c\left(i\right)$ because it is lattice dependent on the already discovered endmembers.

   (c) Test max/min dominance to ensure SLI, consider the enlarged set of endmembers $E' = E \cup \left\{\mathbf{f}^c\left(i\right)\right\}$

      i. $\mu_1 = \mu_2 = 0$
      ii. for $i = 1, \ldots, K+1$
      iii. $\mathbf{s}_1 = \mathbf{s}_2 = \mathbf{0}$

         A. for $j = 1, \ldots, K+1$ and $j \neq i$
            $\mathbf{d} = \mathbf{e}_i - \mathbf{e}_j$; $m_1 = \max\left(\mathbf{d}\right)$; $m_2 = \min\left(\mathbf{d}\right)$.
            $\mathbf{s}_1 = \mathbf{s}_1 + \left(\mathbf{d} == m_1\right)$, $\mathbf{s}_2 = \mathbf{s}_2 + \left(\mathbf{d} == m_2\right)$.
         B. $\mu_1 = \mu_1 + \left(\max\left(\mathbf{s}_1\right) == K\right)$ or $\mu_2 = \mu_2 + \left(\max\left(\mathbf{s}_2\right) == K\right)$.

      iv. If $\mu_1 = K+1$ or $\mu_1 = K+1$ then E' is a set of SLI vectors, go to 3 with the enlarged set of lattice sources and resume exploration with the next input.

5. The output set of endmembers is the set of original data vectors $\left\{\mathbf{f}\left(i\right) : i \in I\right\}$ corresponding to the vectors selected as members of E.

dual LAMs constructed with the current E. The max/min dominance is tested using algorithms inspired in the ones described in [103].

The ILIA (Algorithm 5.2) is a greedy incremental algorithm that passes only once over the sample. It starts as EIHA computing the zero mean shifted image. The endmember set E is initialized with a randomly picked zero mean shifted pixel spectrum vector. The dilative AMM is built with the current set of endmembers. All the pixels are tested following the ensuing steps. First, if the pixel lies in the interval defined by the sensitivity factor α around some of the already detected endmembers, then it is discarded as a random perturbation of the endmember. Second, if the recall obtained from the endmemembers AMM appluing the pixel is the pixel itself, then the pixel is lattice dependent on the current endmembers in E. If not, then the pixel is a candidate endmember, that must be considered for testing min or max-dominance. This is done counting the number of times that each vector contains a maximum or minimum component of the pairwise differences between endmbers. If the count is equal to the number of endmembers including the candidate endmember, then the new set of endmembers is effectively SLI. The algorithm rebuilds M_{EE} with the enlarged set and proceeds with the remaining pixels.

The final endmember set is guaranteed to have a set of SLI vectors. There is not, however, any kind of optimality ensured.

Chapter 6

Experimental results of the EIHA

In this chapter we gather the experimental results produced along the work of this PhD. We will first report the results obtained on synthetic hyperspectral images, which allow a very precise quantification of algorithm performances because we have available both the abundance and the endmembers that constitute the ground truth of the image. We can compute the correlations between the ground truth abundance images and the ones induced by the algorithms to obtain precise evaluations of the endmember accuracies. The image generation process allow to obtain various spatial distributions easily, with great realism as described in Appendix A . We also include the experimental results obtained with the real life hyperspectral images described in Appendix B. The Endmember Induction Heuristic Algorithm (EIHA) of Chapter 5 is compared with the Convex Cone Analysis (CCA), Independent Component Analysis (ICA), Principal Component Analysis (PCA) on those images.

6.1 Experiments on synthetic hyperspectral images

We will consider three collections of synthetic images of increasing number of ground truth endmembers: 2, 3 and 5 endmembers were used in the linear

mixing simulating the image generation process. As the number of endmembers increase, the complexity of the problem increases. The aim is to appreciate how the algorithms degrade their response as the number of endmembers grows. For our algorithm, that increase in complexity means tuning the gain parameter α. For CCA means that the search space grows exponentially and for ICA means that it reaches numerical stability problems. When we deal with the 5 endmember images, our algorithm found for some images 4 endmembers instead of 5, and the ICA sometimes was only able to find 3 endmembers. CCA was able to obtain always the desired number of endmembers at the cost of increased time search.

The experiments consisted on the computation of the endmembers and abundance images induced by each method. When applying the ICA and CCA methods we have set the number of endmembers desired to the exact number of ground truth endmembers. Our approach needed the setting of the noise gain parameter α. For the 2 endmember images we set $\alpha = 2$. After some trials, we set $\alpha = 0.3$ for the 5 endmember images. The comparison is qualitative regarding the shape of the endmembers and the likeness of the abundance images, but also quantitative because we can compute the correlation between the ground truth abundance images and the ones obtained after computing the spectral unmixing with the endmembers given by the algorithms.

6.1.1 Quantitative results

Even if the shape of the induced endmember spectra does not correspond to the shape of the ground truth endmember spectra, it is still possible that the abundance images obtained after spectral unmixing may reflect the same spatial distribution of the ground truth synthetic images. To what degree the algorithms are able to uncover the hidden ground truth abundances? It is well known [35] that unsupervised approaches, e.g. clustering algorithms, can perform data analysis, discovering latent classes in the data, up to some permutation of the original classes. That means that the unsupervised algorithms can not identify the original latent classes. Therefore, to evaluate the quality of the unsupervised approaches we must test all possible combination of algorithm result and ground truth information.

To answer this question we first considered some concrete images in the 2, 3, and 5 endmember collections. We compare first the CCA and the EIHA ap-

proaches. After applying the algorithms and computing the abundance images, we computed the correlation coefficient between each ground truth abundance image and the induced ones.

First we consider the case of the 2 endmembers image. Table 6.1 presents the correlation coefficients between the ground truth abundances (columns GT#) and abundances estimated on the basis of the endmembers obtained by EIHA (left) and CCA (right), by rows. We note two things:

- Both algorithms obtain good identification of the ground truth abundances. There is only one entry with high correlation for each ground truth abundance at each row, and the other entry has strong negative correlation.

- The EIHA is slightly better than the CCA.

Let us consider now the case of the 3 endmembers image. In table 6.2 we present the correlation of ground truth and estimated abundance images. We note as in the previous case that the identification of the ground truth is performed by each algorithm, though in different permutations. Besides we note that the strong negative correlation of the other abundances is dimished. Increasing the complexity of the problem decreases the blind class identification ability of the algorithms.

Finally, we consider the 5 endmember image case. In tables 6.3 and 6.4 we present the correlation results for 5 ground truth endmembers, for the EIHA and CCA, respectively. We note the following facts:

- The EIHA is able to biunivocally identify all the ground truth images, that is, each row and column contains only one strong positive correlation, with the remaining entries showing negative correlation.

- The CCA does not achieve the blind indentification. Row #1 has two high correlation entries, meaning confusion between them. Rows #2, #3 and #4 do not have strong positive correlations, meaning indiference. Row #5 has some moderate positive correlations but shows confusion between several ground truth classes.

- EIHA is much better than CCA in this task.

	EIHA		CCA	
	GT#1	GT#2	GT#1	GT#2
#1	-0.99	0.99	-0.97	0.97
#2	1.00	-0.99	0.97	-0.98

Table 6.1: Correlations between ground truth and estimated abundance images, 2 ground truth endmembers.

	EIHA			CCA		
	GT#1	GT#2	GT#3	GT#1	GT#2	GT#3
#1	-0.43	-0.28	0.98	-0.69	0.88	-0.46
#2	0.99	-0.73	-0.60	0.95	0.01	-0.57
#3	-0.61	0.98	-0.27	-0.33	-0.79	0.99

Table 6.2: Correlations between ground truth and estimated abundance image, 3 ground truth endmembers

	GT#1	GT#2	GT#3	GT#4	GT#5
#1	-0.42	-0.27	0.99	-0.40	-0.40
#2	-0.22	-0.19	-0.28	0.99	-0.10
#3	-0.15	-0.11	-0.16	-0.14	0.97
#4	-0.23	0.99	-0.26	-0.21	-0.18
#5	0.99	-0.33	-0.35	-0.25	-0.11

Table 6.3: Correlation of ground truth and estimated abundance images obtained by the EIHA endmembers, 5 ground truth endmembers.

	GT#1	GT#2	GT#3	GT#4	GT#5
#1	0.92	-0.92	-0.92	0.93	-0.94
#2	-0.16	0.09	0.22	-0.15	0.18
#3	0.03	-0.02	-0.08	0.02	-0.02
#4	-0.22	0.27	0.23	-0.26	0.22
#5	-0.60	0.61	0.57	-0.58	0.57

Table 6.4: Correlation of ground truth and estimated abundance images obtained by the CCA endmembers, 5 ground truth endmembers.

It is evident that our algorithm is able to "discover" the ground truth abundances in the sense of obtaining images with high correlation and no confussion.

Next we extend this experiment to the whole collection of synthetic images, applying EIHA, CCA and ICA. As said above, the estimated abundance images and the induced endmembers are given in an order which is, in the best case, a permutation of the true classes in the ground truth information. Giving the detailed correlation matrices for each image would be an annoying amount of information. Therefore, we will only consider aggregated information, in the form of the best or the worst correlation with the ground truth images.

The experimental database contains several images generated with 2 ground truth endmembers, varying the θ parameter of the correlation function used to generate the abundances. Let us consider only the positive correlations that may be associated with a positive identification of the gorund truth abundance image. We plot in figure 6.1 the highest of such correlations obtained by the competing methods: EIHA (denoted AMM in the figures in this section), ICA and CCA. The plot gives a best value for each θ value, corresponding to an image. It can be appreciated that the EIHA provides the best identification of one of the ground truth classes, very close to 1. Next best is ICA and the CCA provides less optimal identification. We assume that the identification for this class in the images is as in the table 6.1, so that both classes are identified with positive correlations. If we consider the lowest positive correlation, we obtain the plot in figure 6.2. This plot corresponds to the strength of identification of the other ground truth class. Then, ICA results are very bad, while EIHA (denoted AMM) and CCA have similar values as in the figure 6.1. The explanation of ICA's behavior lies in the fact that ICA identifies non-Gaussian sources. Only one Gaussian source can be identified. In the present case, that means that only one of the two ground truth classess can be identified. So the results are consistent with the theoretical expectations. This highlights an intrinsic problem in the application of ICA to hyperspectral image unmixing, that it is very difficult to find images with non-Gaussian sources in the real life applications. It must be noted that the figures have been ordered by the correlation parameter of the gaussian random field aiming to detect influences of the noisiness of the ground truth in the performance of the algorithms. We do not detect any one. That is, our approach is robust against spatial noise in the abundance images.

45

Figure 6.1: Highest positive correlations obtained on the 2 endmember synthetic images between the ground truth abundance images and the ones induced by each method: EIHA (denoted AMM), CCA and ICA.
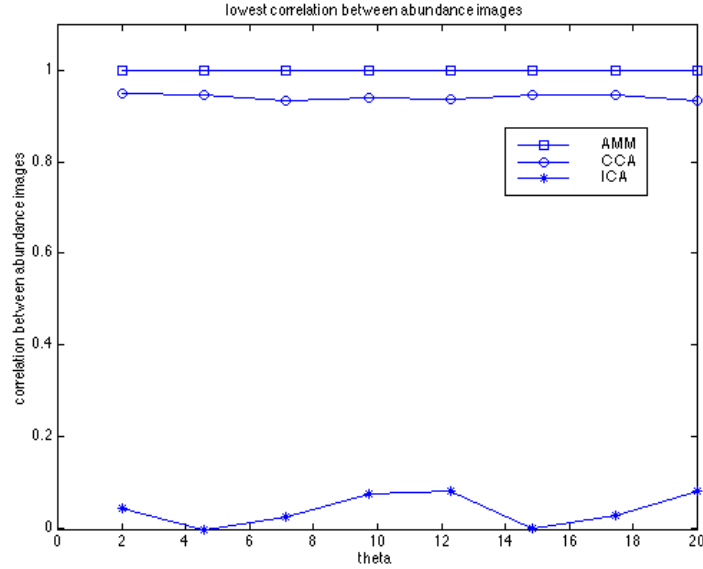
Figure 6.2: Lowest correlations obtained on the 2 endmember synthetic images between the ground truth abundance images and the ones induced by each method: EIHA (denoted AMM), CCA and ICA.

For the images generated with 5 ground truth endmembers we will consider the best correlations obtained for each ground truth image all over the database. This is shown in figure 6.3. This plot does not give information about the possible confusion in the matrix that can be appreciated in table 6.4. We are, thus, focusing on the strength of the best identification found in the correlation table. It can be appreciated that EIHA is the best approach again. ICA is the worst approach most of the times, while CCA is in between. Low positive correlations are a sure symptom for the existence of confusions. If we consider now the lowest positive correlation for each ground truth abundance image, we obtain the plot in figure 6.4. We find that EIHA provides the best results, ICA repeats the worst results, indicative of confusions, and CCA is in between.

Finally we plot all the correlations (after sorting them in ascending order) found by the algorithms in all the images. In figure 6.5 we show them. The abscissa is the ordinal of the estimated abundance image. Note that the curves for ICA are sometimes shorter, because it is not able to obtain the 5 endmembers from the image. Overall EIHA gives the best results again, outperforming CCA and
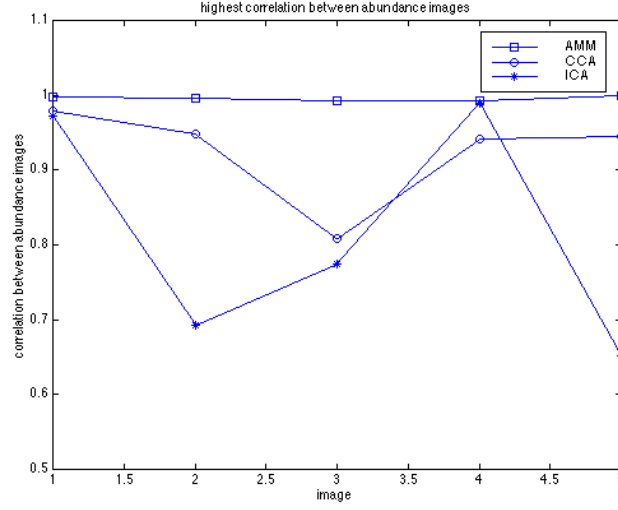
Figure 6.3: Higest correlations obtained on the 5 endmember synthetic images between the ground truth abundance images and the ones induced by each method: EIHA (denoted AMM), CCA and ICA.
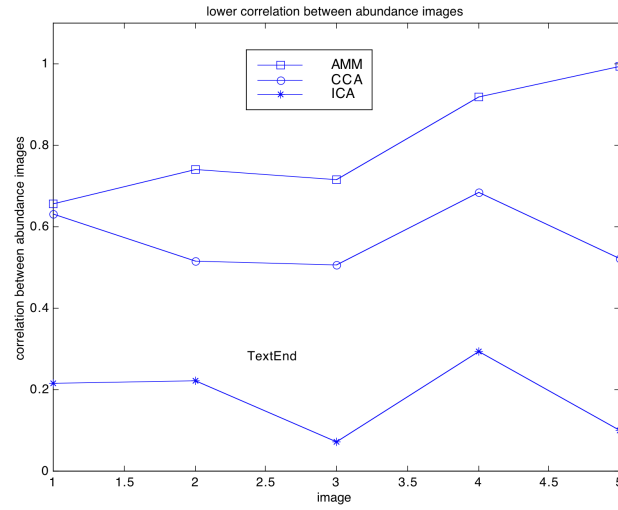
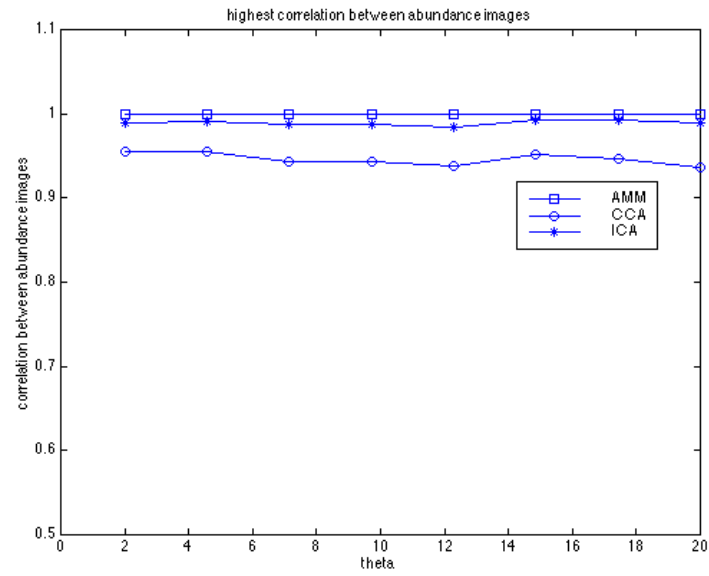Figure 6.4: Lowest correlations obtained on the 5 endmember synthetic images between the ground truth abundance images and the ones induced by each method: EIHA (denoted AMM), CCA and ICA.

ICA. As said before, ICA can only identify one Gaussian source. It can be appreciated that sometimes one of the ICA abundance correlation result comes close to the EIHA results. This correspond to the identified Gaussian source, the other are very far below.
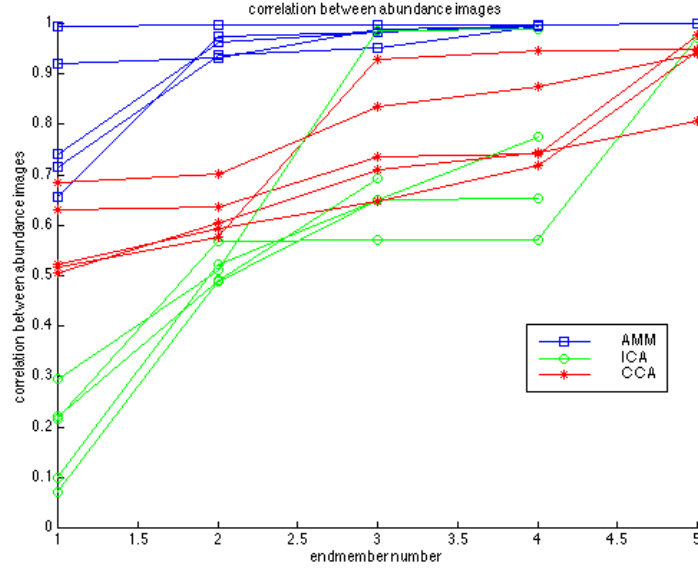
Figure 6.5: Correlations obtained of the induced abundance images with the ground truth for all the 5 endmember synthetic images and methods: EIHA (denoted AMM), CCA and ICA.

6.1.2 Visual qualitative results

We present some instances of the abundance images in figures 6.6, 6.7 and 6.8, to give a qualitative assessment of the results. In the case of 2 endmember images, we present the results without ordering, while for the 5 endmember images we have ordered the induced abundances by their correlation with the ground truth abundance. It can be appreciated that EIHA's estimated abundance images almost reproduce the ground truth abundance images. This is not true for CCA and ICA. For them some of the abundance images are unrelated with the ground truth, while others appear like combinations of several ground truth abundances. Nevertheless these qualitative observations may be of no use with very noisy images, like the ones in figure 6.6, where it is very difficult to ascertain visually

the identification of original abundance structure in the induced images. For this reason, the quantitative evaluation is more useful than the visual inspection of the results.
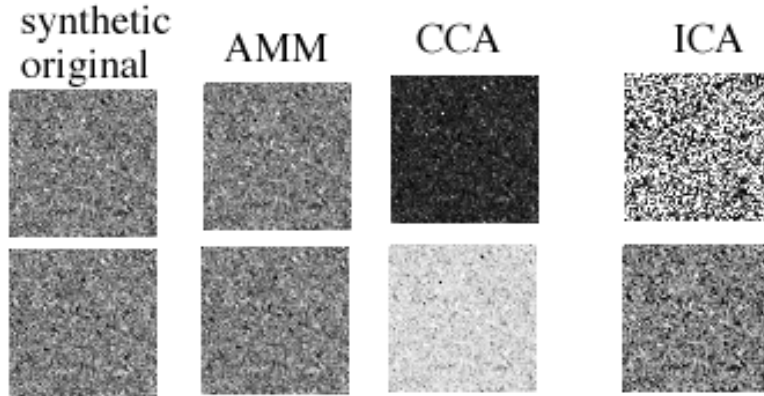
Figure 6.6: Abundance images generated with covariance parameters $\theta = 2$, used to synthetize a 2 endmember hyperspectral image, and the abundance images induced by the EIHA (denoted AMM), ICA and CCA
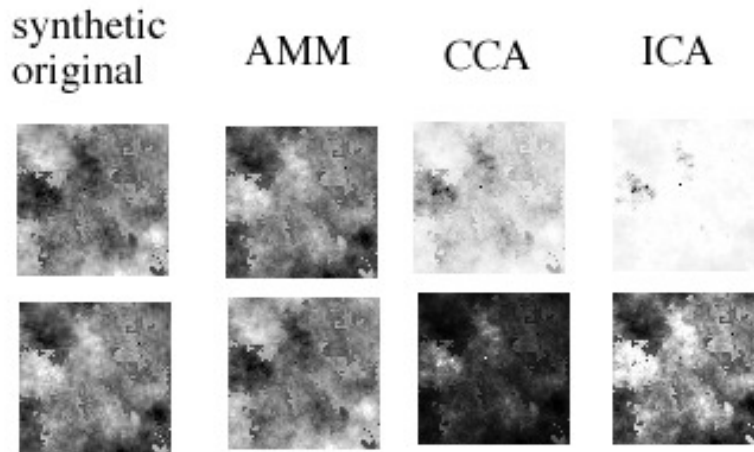
Figure 6.7: Abundance images generated with covariance parameters $\theta = 20$, used to synthetize a 2 endmember hyperspectral image, and the abundance images induced by the EIHA (denoted AMM), ICA and CCA
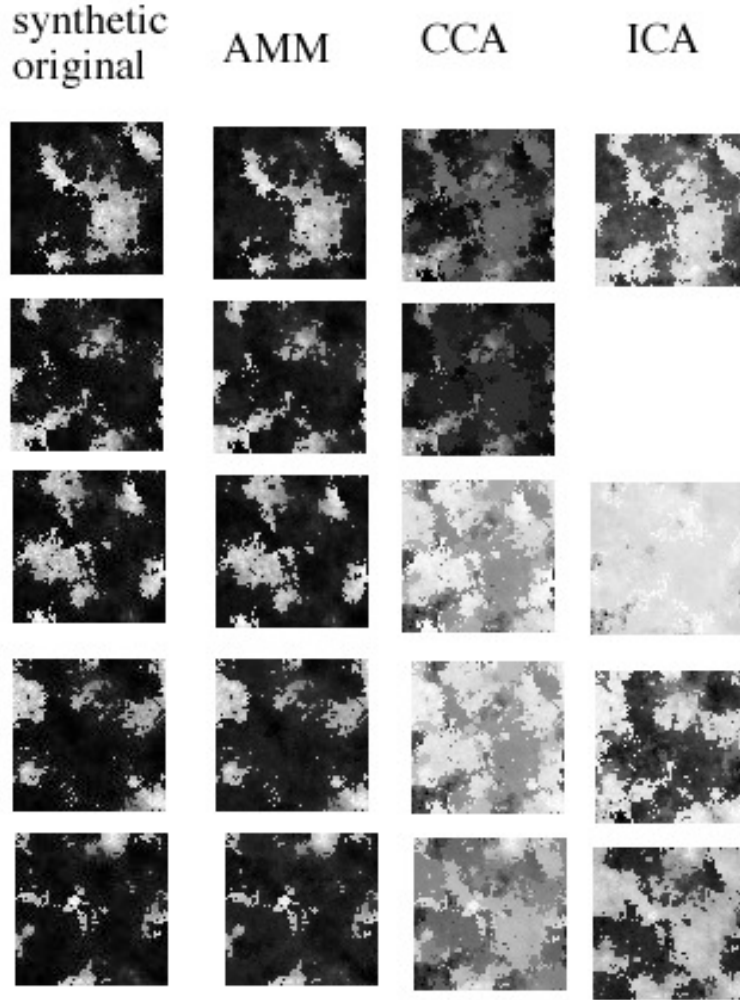
Figure 6.8: Abundance images generated with parameters $\theta = 20$, used to synthetize a 5 endmember hyperspectral image, and the abundance images induced from the data by the EIHA (denoted AMM), ICA, and CCA.

We can perform a visual inspection of the induced endmembers. We must recall that our approach selects spectra from the image, therefore it does not introduce additional noise. We have considered two images of 2 ground truth endmembers, generated with $\theta = 2$ and $\theta = 20$, and an image of 5 ground truth endmembers generated with $\theta = 20$. We show in figures 6.9, 6.12, 6.15 the EIHA induced endmembers. It can be appreciated that they are very similar

to the ones reproduced in the Appendix A. The endmembers induced by CCA (figures 6.10, 6.13, 6.16) and ICA (figures 6.11, 6.14, 6.17) have no relation with the ground truth endmembers used to generate the images. However, if we want to obtain unsupervised segmentations of the images, then the exact shape of the induced endmembers is not important because very different sets of endmembers may give very similar abundance images.
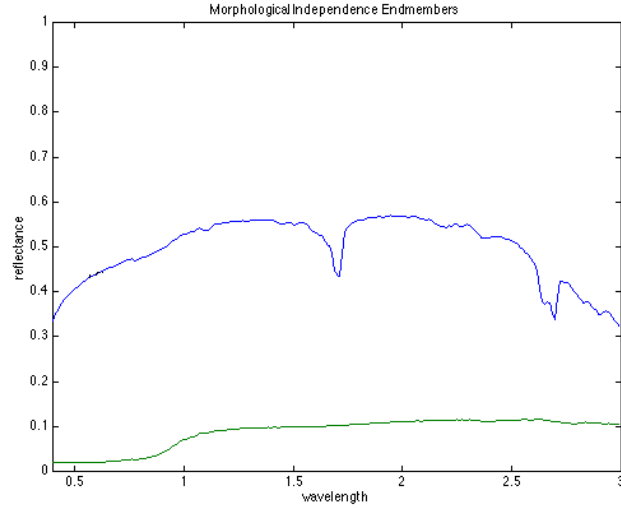
Figure 6.9: Endmembers induced by EIHA on a 2 endmembers synthetic image of parameter $\theta = 2$.
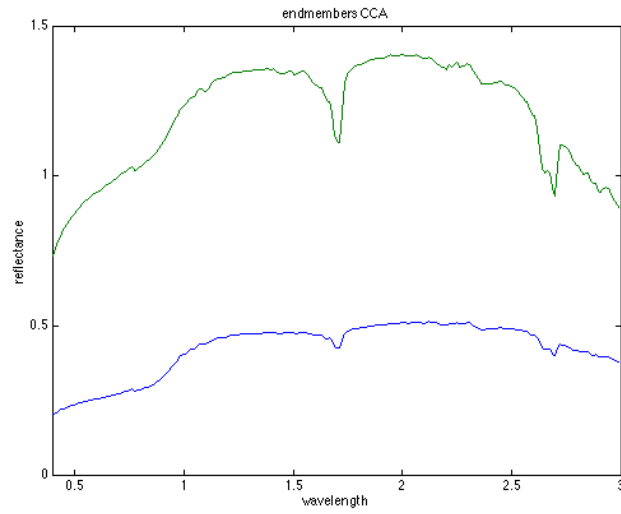
Figure 6.10: Endmembers induced by CCA on a 2 endmembers synthetic image of parameter $\theta = 2$
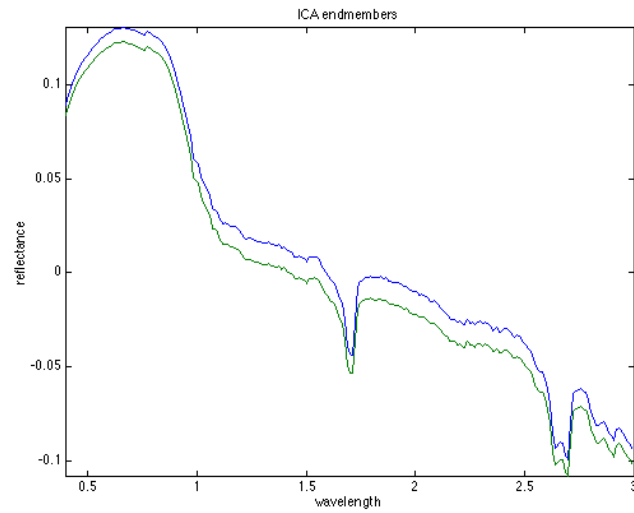
Figure 6.11: Endmembers induced by ICA on a 2 endmembers synthetic image of parameter $\theta = 2$
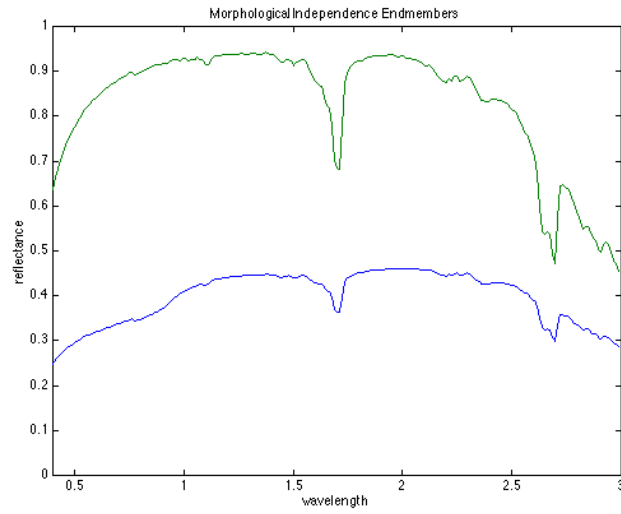
Figure 6.12: Endmembers induced by EIHA on a 2 endmembers synthetic image of parameter $\theta = 20$
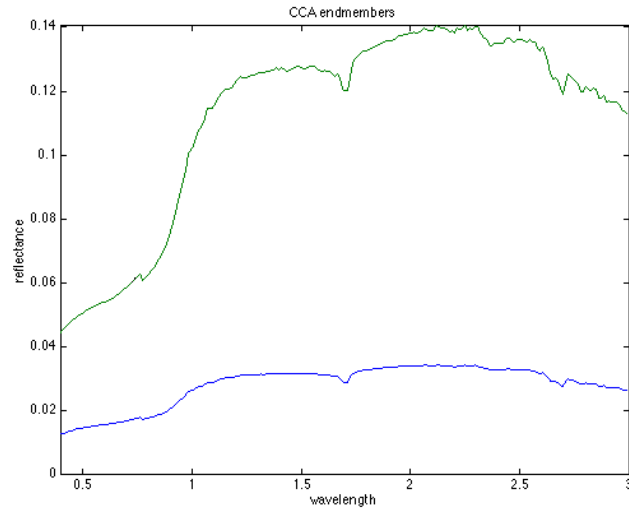
Figure 6.13: Endmembers induced by CCA on a 2 endmembers synthetic image of parameter $\theta = 20$
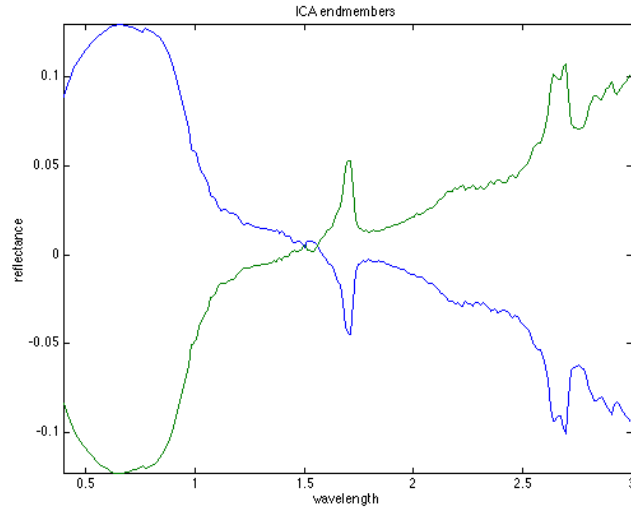
Figure 6.14: Endmembers induced by ICA on a 2 endmembers synthetic image of parameter $\theta = 20$
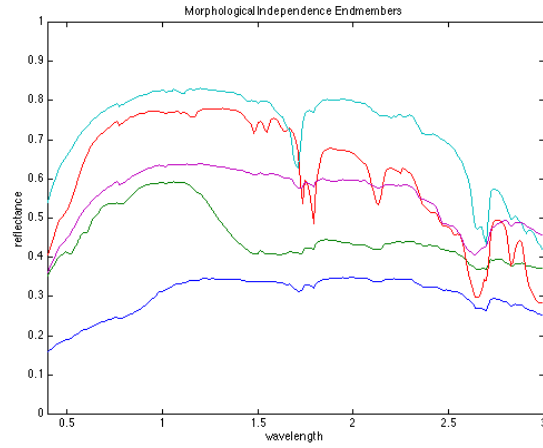
Figure 6.15: Endmembers induced by the EIHA on a 5 endmembers synthetic image of parameter $\theta = 20$.
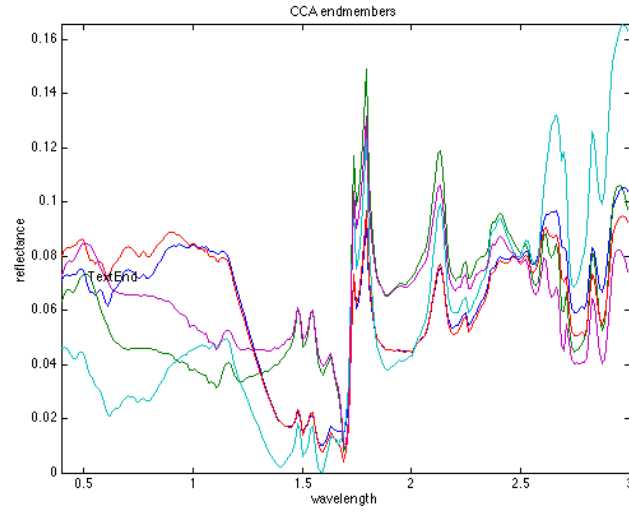
Figure 6.16: Endmembers induced by the CCA on a 5 endmembers synthetic image of parameter $\theta = 20$ (after normalization).
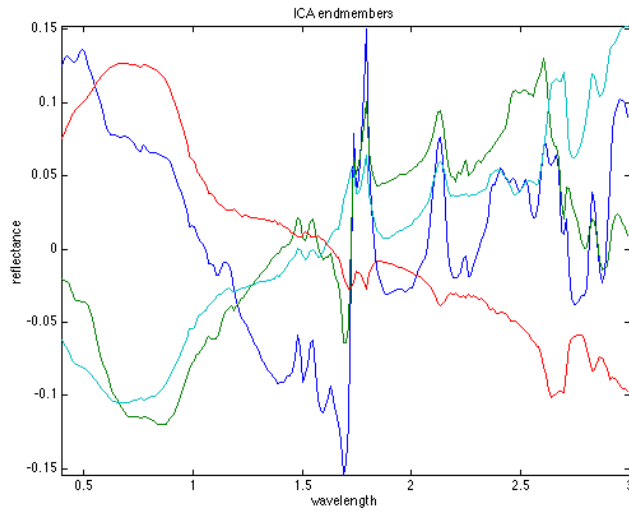
Figure 6.17: Endmembers induced by the ICA on a 5 endmembers synthetic image of parameter $\theta = 20$ (after normalization).

6.2 Experimental results on remote sensing images

We have tested our approach on the Indian Pines image and on the Salinas image which are described in Appendix B. There are two kinds of validation processes involved: one is the qualitative visual inspection of the abundance images, the other is the realization of classification experiments based on the abundance coefficients as feature vectors for the classification systems.

6.2.1 Visual results on Indian Pines

6.2.1.1 Results after PCA

We have performed a Principal Component Analysis (PCA) pixel spectra dimension reduction from 220 to 11 coefficients. The EIHA algorithm has been applied to the PCA coefficients. Working with the PCA reduced data has the advantage of reducing the computational requirements, however it is not clear whether significant information is lost in the dimension reduction process. An important remark: the endmember spectra are taken from the original image, not from the PCA reconstruction. Thus the spectral unmixing is performed on the original image.

Setting $\alpha = 0.2$, we have obtained 8 endmembers. This number of endmembers seems reasonable for this image. We can not use information about the ground truth number of classes in a pure unsupervised approach.

The spectral unmixing based on the endmember spectra found produces abundance images that can be interpreted according to the ground truth in Appendix B assuming that the white corresponds to high concentrations of the corresponding endmember, and, therefore, to the detection of a specific kind of cover. The abundance images are presented in figure 6.18.

- Endmember #1 seems to identify some brushwood marginal regions. These results do not fit well in the ground truth characterization, corresponding mainly to background.

- Endmember #2 identifies the metal towers and shows some confusion with crop fields. Crops in an early stage of growth show mostly bare soil. This confusion is typical of unsupervised methods.
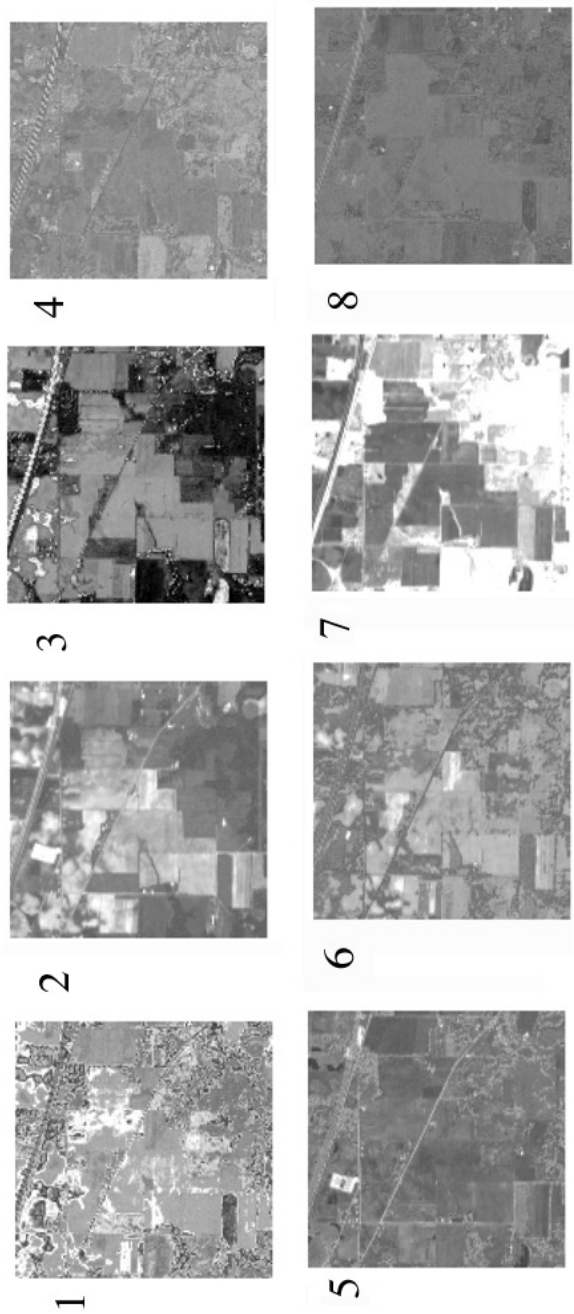
Figure 6.18: Abundance images obtained by EIHA on the PCA coeficients of the Indian Pines image pixel spectra. Unmixing is performed on the original spectra.

58

- Endmember #3 identifies a highway, and has negative response to vegetation covers, specially woods. If we consider the fact that due to the early growth stages most of the surface area corresponding to a pixel in the cultivated land is bare soil, we may assume that the endmember that generates this abundance image corresponds to soil cover spectra.

- Endmember #4 has very little contrast. It may be confused with noise background. Endmember #8 has a similar low contrast appearance.

- Endmember #5 gives a more discriminant identification of the steel and stone towers, also seems to detect asphalt-like materials corresponding to roads. Our interpretation is that this endmember corresponds to a generic opposite to the vegetal cover spectra.

- Endmember #6 seems to detect some grass related cover class.

- Endmember #7 is definitively a positive detector of woods and tree-like vegetal covers. The background cover in the ground truth does correspond to woods in a high percentage of its area. This result agrees with the results of careful supervised classification experiments reported in [100].

- The wheat cover is not detected by any endmember. Other unsupervised approaches have also found difficulties in detecting this region of the image.

6.2.1.2 Results on the raw data

We have applied EIHA and CCA to the Indian Pines image. Setting EIHA's parameter $\alpha = 2$, we have obtained 8 endmembers. The abundance images resulting from the unmixing with the induced endmembers are shown in figure 6.19. Comparison with the results of careful supervised classification [100] explain their discrepancies relative to the ground truth areas. Regarding the EIHA results we can note the following facts:

- The endmember #1 does identify stone or asphalt like materials, because it detects clearly the steel and stone towers as well as the roads in the image. The towers are also strongly detected by endmember #5.

- Endmember #7 is a good detector for woods and vegetal covers alike to them, trees and brushwood.
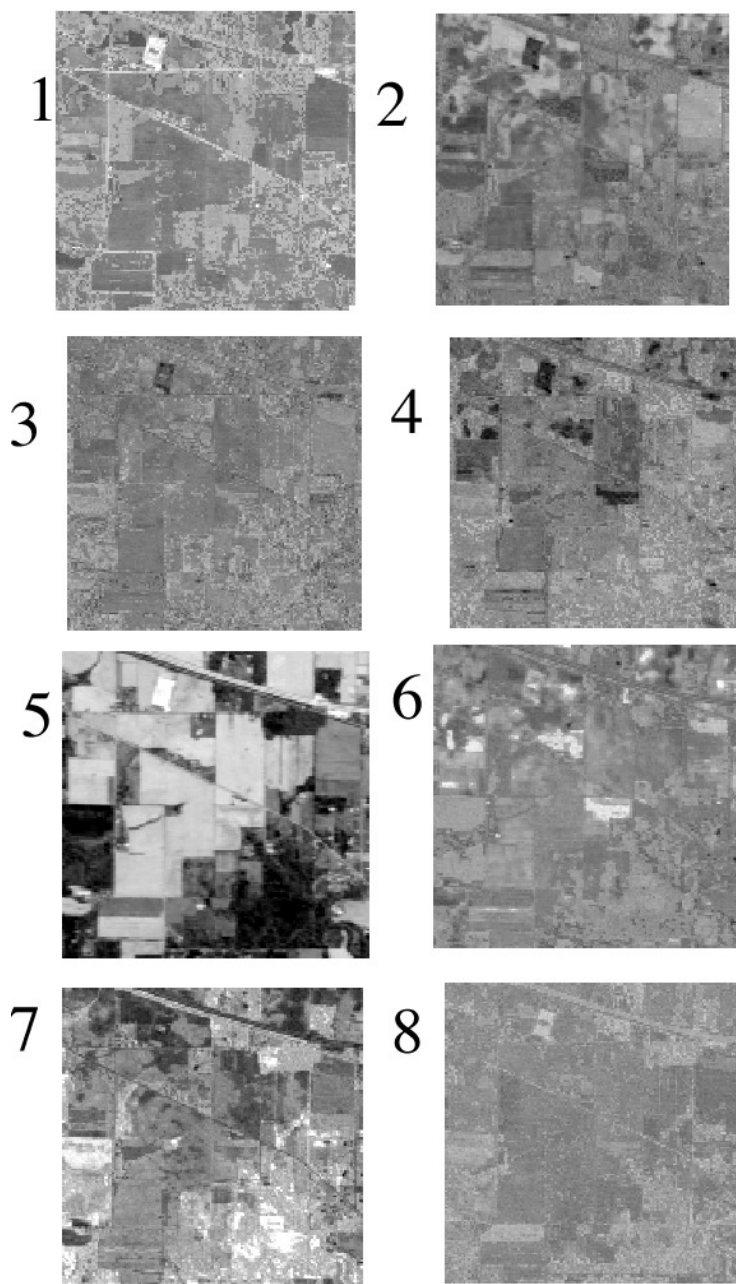
Figure 6.19: Abundance images obtained by spectral unmixing using the end-member spectra obtained with the EIHA on the Indian Pines raw image data.
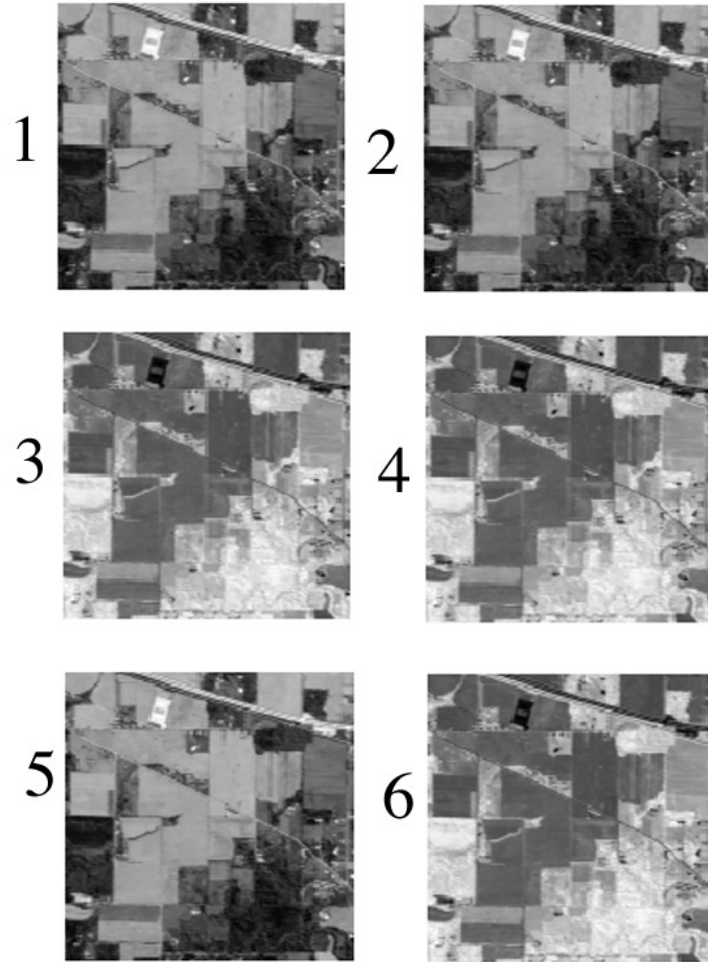
Figure 6.20: Abundance images obtained by spectral unmixing using the end-member spectra obtained with the CCA method on the Indian Pines raw image data.

- Endmember #5 is a good detector of soil and mineral cover, because it detects crop fields that seem to be in early growth stages and the steel and stone towers, as well as some other buildings.

- Endmembers #2, #3 and #8 have little contrast. They detect mostly vegetation.

- The wheat cover regions is not detected.

The comparison with the abundance images obtained from the spectral unmixing with the CCA endmembers serves also to the qualitative validation of our procedure. We have applied the CCA method with the number of endmembers set to 6 (a number of endmembers greater than that gave very large computation times). The abundance images are presented in figure 6.20. Note that they are two basic images repeated three times. The endmember spectra corresponding to two similar abundance images are almost proportional. We note the following facts:

- Endmembers #1, #2, #5 show good detection of soil and stone like structures. It detects the steel and stone towers, the crop fields in early growth stage and the highway.

- Endmbers #3, #4, #6 show good detection of vegetal cover, specially woods. The ground truth background class pixels identified also with woods in some areas of these abundance images agree with the results of careful supervised classification experiments reported in [100].

- The wheat cover region is not detected.

Comparing the CCA with the EIHA results on this image raw data we find that the EIHA gives more endmembers with better discrimination properties of some of the basis ground truth classes. The correspondence with the ground truth information is also better in some cases. The EIHA shows the ability to obtain improved unsupervised segmentations of the hyperspectral images.

6.2.2   Classification results on the Salinas A

The approach in this section is an indirect validation of the unmixing algorithms through the realization of classification experiments using the abundance coefficients as the feature vectors for the classification at the pixel level. The pixel
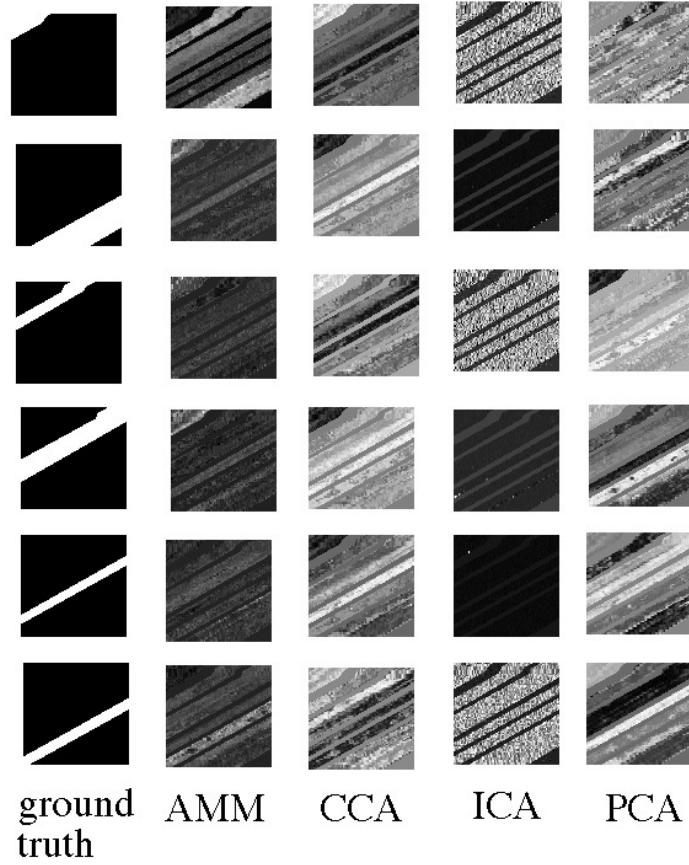
Figure 6.21: From left to right the ground truth abundance images for the Salinas A image, the abundance images obtained from the endmembers induced by EIHA (denoted AMM) and the CCA approaches, the image planes of the coefficients of the linear transformations: ICA and PCA

	1-NN	Gauss	SVM
raw	0.25 (0.0055)	0.22 (0.0303)	0.48 (0.0068)
PCA	0.49 (0.0078)	0.17 (0.0042)	0.49 (0.0052)
ICA	0.45 (0.0083)	0.12 (0.0204)	0.48 (0.0084)
CCA	0.62 (0.0095)	0.46 (0.0067)	0.69 (0.0066)
EIHA	0.63 (0.0078)	0.48 (0.0070)	0.72 (0.0062)

Table 6.5: Classification accuracy and its standard deviation for the 1-NN, Gaussian and SVM classifiers using the raw data of Salinas A and the features extracted by the linear dimension reduction algorithms and the AMM approaches

---

Algorithm 6.1 Endmember induction validation using on supervised classification.

---

1. For each endmember induction algorithm

   (a) Compute the endmember induction

   (b) Compute the abundance images by spectral unmixing with the found endmembers.

   (c) Abundance coefficients are the feature vectors of each pixel. Class labels are given by the ground truth.

   (d) Partition the image data into train and test datasets.

   (e) For each classifier sytem

      i. Train the classifier on the train data.
      ii. Test the classifier.

---

labels correspond to the ground truth classes provided with the image. The approach is summarized in Algorithm 6.1. To test the supervised classification based on the dimension reduction discussed above we focused the study in a subscene of the Salinas dataset (Salinas A) which comprises 83x86 pixels, (described in Appendix B). The different ground truth classes for this data appear as binary images in the left column of images in figure 6.21.

We compute the endmember induction using the EIHA, PCA, CCA and ICA algorithms. The parameter setting is as follows:

- For the EIHA we set $\alpha = 3$ obtaining 6 endmembers.

- For the PCA, ICA and CCA methods we have set the target dimension to the exact number of ground truth components.

The columns in figure 6.21 show the abundance images obtained by the spectral unmixing of the Salinas A image using the endmembers obtained by the different algorithms. Some of the approaches produce abundance images similar to the ground truth images in the leftmost column. It can be appreciated from the images that the CCA and AMM abundance images identify more clearly some of the ground truth regions, than ICA and PCA images. Computing the correlation between these images and the ground truth ones confirms this qualitative intuition.

The supervised classifiers employed were the two simplest ones: the Nearest Neighbor (1-NN) and the Gaussian Classifier (Gaussian) using the Euclidean distance. These classifiers are the simplest ones , so they will not introduce additional bias in the experiment, which is aimed to show the value of the spectral unmixing as a feature extraction algorithm. Finally, we have also applied the SVM [1], with a Radial Basis Function (RBF) kernel of identical variances. As said in the introduction, no attempt has been made to tune the SVM in order to improve the results, because the idea we want to stress is that the abundance images produced by the EIHA induced endmembers improve the other approaches as a feature extraction process.

The experiment consisted in 30 repetitions of the construction and validation of the clasifiers on 2-fold crossvalidation partitions of the data which preserve the *a priori* distributions of the classes. It must be said that the Salinas data is highly noisy, with a very low Signal to Noise Ratio (SNR) in the region of visible light. The SNR improves somehow in the infrared range, but still some of the bands appear almost random. We did not perform any band selection or smoothing of the pixel spectra in the experimental results presented here, although we did a large exploratory experimentation.

The classification accuracy results of the experiment are presented in table 6.5. They consist of the average accuracy of the classifiers and the standard deviation between brackets. Rows correspond to the feature used. First row is the result for the raw pixel spectra, the second row for PCA, the third for ICA, the fourth for the unmixing features using CCA endmembers and the last row for the unmixing features using EIHA endmembers.

The The 1-NN classifier shows a substantial improvement compating the linear feature extraction algorithms PCA and ICA over the raw spectral data. Using

---

[1]Using the implementation by Anton Schwaighofer available in http://www.cis.tugraz.at/igi/ aschwaig/software.html

the unmixing features obtained from CCA and EIHA endmembers improves the linear feature extraction. The Gauss classifier shows lower performance in the linear feature extraction relative to the raw data. This may be due to the low SNR of the data. The spectral unmixing feature approaches however show a significant improvement over the raw data. Nevertheless, the Gaussian classifier performance is very poor. The SVM improves over the 1-NN and Gaussian classifiers on the spectral unmixing features. However, the results on the raw data, PCA and ICA features are undistinguishable. Overall the EIHA features provide the best results in all classifier instances.

6.3   Conclusions

In this chapter we report our results on hyperspectral image segmentation based on both unsupervised and supervised approaches. For the unsupervised approach, we consider that the abundance images obtained after the endmember induction and unmixing process are the region segmentation of the image, where high abundances of each endmember determine image segmentation regions. For the supervised approach, we assume the abundances as features vectors characterizing each pixel, therefore we built supervised classifiers to test the quality of these features. The endmember induction algorithm presented in previous chapters has been applied to both synthetic hyperspectral images and real life remote sensing hyperspectral images obtained from public repositories. We have compared the results of our approach with other linear feature extraction, such as PCA and ICA, and other endmember induction algorithms, such as CCA.

Comparison with other approaches has been qualitative and quantitative. In the qualitative comparison we visualize the extracted endmembers or components and the corresponding abundance images. For synthetic images this approach is of little use, because of the random appearance of the ground truth synthetic images. However, for real life images provided with some ground truth information, this qualitative comparison has some value. We found that our approach compares well with the state of the art algorithms, obtaining visually meaningful segmentations of the images. The quantitative comparison involves the computation of the correlation of the obtained abundances with the ground truth images. For the synthetic images, the knowledge of the ground truth abundances is perfect, so the performance evaluation is perfect in this regard. For the real life images, the ground truth information is approximated and the

correlations obtained are not a perfect measure of performance. Despite that, we found that our approach give very good results on the images tested, finding abundance images with good ground truth correlation, sometimes improving all other approaches. As a further quantitative comparison we performed supervised classification experiments on natural images. In these experiments, abundances where taken as feature vectors input to the trained classifiers. We found that using the abundances, whether the endmembers have been obtained with our algorithm or with other endmember induction algorithms, improves the classification results over PCA and ICA. We find these results encouraging towards the development of a feature extraction methodology based on image unmixing with unsupervisedly extracted endmembers.

Chapter 7

Spectral CBIR system

In this chapter we present some ideas about Content Based Image Retrieval (CBIR) systems for hyperspectral image databases. The approach followed is to provide a spectral characterization of the images, because the ability to provide spectral information is their most distinctive property. The spectral characterization is naturally provided by the endmembers that can be identified in the image by an endmember induction algorithm (EIA). We have tested our own proposal, the ILIA described in Chapter 5, and other state of the art algorithm in order to evaluate the sensitivity of the approach to the EIA used. The CBIR system core is the definition of an appropriate dissimilarity measure that allow to find images with similar spectral characterizations. We have defined a dissimilarity measure computed over the matrix of individual distances among the respective endmembers of the images being compared. The endmember distance can be either the Euclidean distance or the spectral angle (SAM) distance. We have also tested the sensitivity of the system to this underlying distance. The structure of the proposed Spectral CBIR system is illustrated in figure 7.1. In order to validate our approach we needed a large quantity of images, to make the validation realistic. To that end we have generated a large collection of synthetic images.

The structure of the chapter is as follows: Section 7.1 gives our dissimilarity measure. Section 7.2 describes the synthetic images used in the validation experiments. Section 7.3 describes the performance measures used for validation. Section 7.4 gives the results of the validation experiment. Finally, section 7.5 gives some conclusions and future work directions.
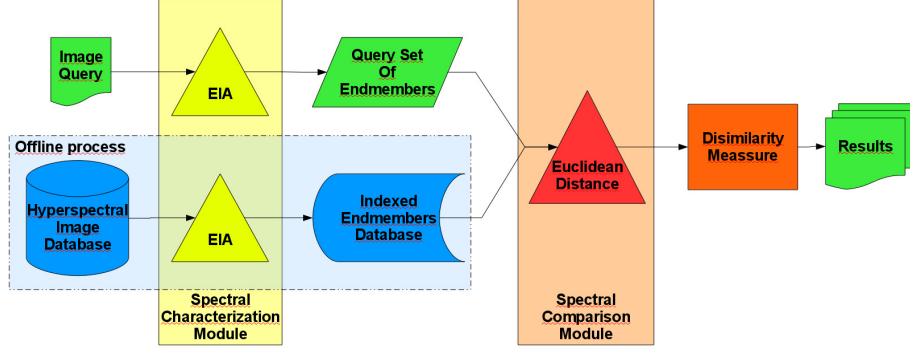
Figure 7.1: Spectral CBIR structure using the Euclidean distance among endmembers.

7.1 Dissimilarity distance

We propose a CBIR system for databases of hyperspectral images where images are indexed by the endmembers E induced from them [62, 105]. A dissimilarity function between two hyperspectral images, $s\left(H_\alpha, H_\beta\right)$ is defined on the basis of the distances between their corresponding set of endmembers E_α and E_β. Let it be $E_\alpha = \left\{\mathbf{e}_1^\alpha, \mathbf{e}_2^\alpha, \ldots, \mathbf{e}_{p_\alpha}^\alpha\right\}$ the set of endmembers induced from the hyperspectral image H_α in the database, where p_α is the number of induced endmembers from the α-th image. Given two images, H_α, H_β, we compute the following matrix whose elements are the distances between the endmembers of each image:

$$D_{\alpha,\beta} = [d_{i,j}; i = 1, \ldots, p_\alpha; j = 1, \ldots, p_\beta], \tag{7.1}$$

where $d_{i,j}$ is any defined distance between the endmembers $\mathbf{e}_i^\alpha, \mathbf{e}_j^\beta \in \mathbb{R}^q$; i.e. the Euclidean distance, d_{euc}, or the Angular distance, also known as Spectral Angle Mapper (SAM) distance in remote sensing applications, d_{sam}:

$$d_{euc}\left(\mathbf{e}_1, \mathbf{e}_2\right) = \sqrt{\sum_{k=1}^{q} \left(e_{1,k} - e_{2,k}\right)^2} \tag{7.2}$$

$$d_{sam}\left(\mathbf{e}_1, \mathbf{e}_2\right) = \cos^{-1}\left(\frac{\sum_{k=1}^{q}\left(e_{1,k} \cdot e_{2,k}\right)}{\sqrt{\sum_{k=1}^{q}\left(e_{1,k}\right)^2}\sqrt{\sum_{k=1}^{q}\left(e_{2,k}\right)^2}}\right) \tag{7.3}$$

	$\mathbf{e}_1^\beta$	$\mathbf{e}_2^\beta$	$\mathbf{e}_3^\beta$	$\mathbf{e}_4^\beta$	$\min_\mathbf{r}$
$\mathbf{e}_1^\alpha$	0.9	0.8	0.8	0.8	**0.8**
$\mathbf{e}_2^\alpha$	0.4	0.3	0.5	0.4	**0.3**
$\mathbf{e}_3^\alpha$	0.9	0.7	0.7	0.8	**0.7**
$\min_\mathbf{c}$	**0.3**	**0.3**	**0.4**	**0.4**	

Table 7.1: Example of a matrix of endmember distances $D_{\alpha,\beta}$

Then the disimilarity between two hyperspectral images, H_α, H_β, is given as a function of the distance matrix (7.1) by the following equation:

$$s\left(H_\alpha, H_\beta\right) = \left(m_r + m_c\right)\left(|p_\alpha - p_\beta| + 1\right) \tag{7.4}$$

where m_r and m_c are the mean of the vectors of minimal values, $\min_\mathbf{r}$ and $\min_\mathbf{c}$, of the distance matrix, $D_{k,l}$, computed by rows and columns, respectively. The value of m_r represents the degree of inclusion of the set E_α in E_β, that is a meassure of how the materials displayed in the image H_α are also presented in the image H_β. In the same way, the value of m_c represents the degree of inclusion of the set E_β in E_α. The factor $\left(|p_\alpha - p_\beta| + 1\right)$ of 7.4 penalizes the difference on the number of materials found in each image p_α, p_β. Note that the endmember induction algorithm can give different number of endmembers for each image. The proposed dissimilarity function can cope with this asymmetry avoiding the combinatorial problem of trying to decide which endmembers can be matched and what to do in case that the number of endmembers is different from one image to the oher.

Example Given a matrix $D_{\alpha,\beta}$ of endmember distances for some sets of end-members $E_\alpha = \{\mathbf{e}_1^\alpha, \mathbf{e}_2^\alpha, \mathbf{e}_3^\alpha\}$ and $E_\beta = \left\{\mathbf{e}_1^\beta, \mathbf{e}_2^\beta, \mathbf{e}_3^\beta, \mathbf{e}_4^\beta\right\}$ induced from the images H_α and H_β respectively, we calculate the vectors of minimum values by rows and columns (Table 7.1). The means of the minima computed by rows and columns are respectively $m_r = 0.6$ and $m_c = 0.35$. All the materials presented on the image H_β are somehow similars to one of the materials presented in H_α; however, only the second material in image H_α is similar to any of the materials in image H_β. This illustrates the asymmetry between the image characterizations. The dissimilarity between the images is then $s\left(H_\alpha, H_\beta\right) = (0.6 + 0.35)\left(|3 - 4| + 1\right) = 1.850$.

7.2 Synthetic hyperspectral images

The synthetic hyperspectral images are synthesized as linear mixtures of a set of spectra (the ground truth endmembers) mixed according to selected abundance coefficients for each pixel. Because the generation of the abundance coefficients follows a spatial distribution, we generate independent images for each abundance coefficient corresponding to an endmember, later we fuse them into a multidimensional abundance image imposing normalization conditions for each pixel independently. The ground truth endmembers were randomly selected from a subset of the USGS spectral library.

The synthetic ground truth multidimensional abundance images were generated in a two-step procedure. First, we simulate each abundance image corresponding to an endmember as a gaussian random field with Matern correlation function of parameters $\theta_1 = 10$ and $\theta_2 = 1$. We applied the procedure proposed by [56] for the efficient generation of gaussian random fields with large domains. Second, to ensure that there are regions of almost pure endmembers, we selected for each pixel the abundance coefficient with the greates value and we normalize the remaining to ensure that the abundance coefficients sum up to one. It can be appreciated observing the abundance images that each endmember has several regions of almost pure pixels, viewed as brighter regions in the images.

We have synthesized a total of 6000 hyperspectral images divided in three datasets of 2000 images each. Each dataset of images is characterized by the number of endmembers in the collection of ground truth endmembers. We defined three collections of ground truth endmembers, with 5, 10 and 20 endmembers each, used to synthesize the datasets, respectively denoted as 5-dataset, 10-dataset and 20-dataset; representing an incresing diversity in the materials. The size of the images is 256x256 pixels with 269 spectral bands *per* pixel. Each dataset contains 500 hyperspectral images, each image built from with 2 to 5 endmembers randomly selected from the corresponding collection of ground truth endmembers. Figure 7.2 shows the collection of ground truth endmembers which is the basis for the generation of the 10-dataset. Figure 7.3 shows an example of ground truth endmembers and corresponding generated abundance images used to synthesize an hyperspectral image.
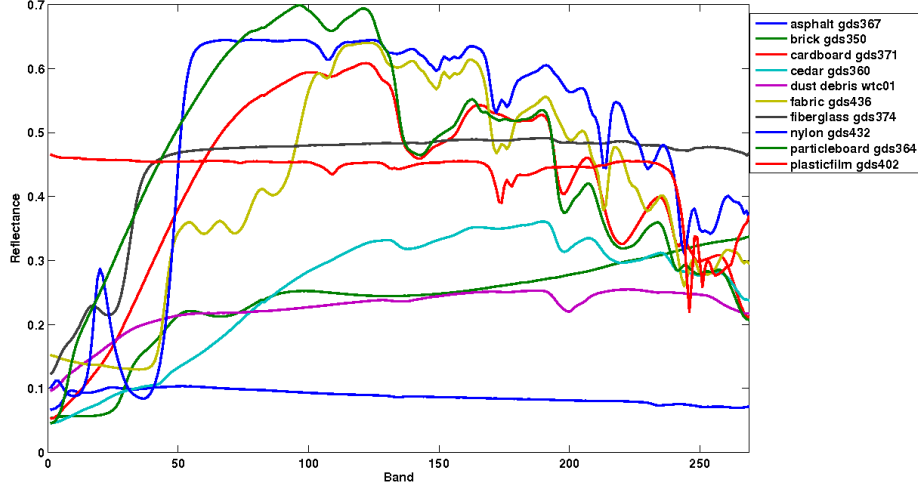
Figure 7.2: Collection of endmembers selected from the USGS library to be the basis to synthesize the hyperspectral images in the 10-dataset.

7.3 Methodology

We have performed independent experiments over each of the three hyperspectral datasets using the dissimilarity function (7.4), where the distance between endmembers is meassured by the Euclidean distance of equation (7.2), s_{euc}, or the SAM distance of equation (7.3), s_{sam}. For each image, we apply independently the N-FINDER and the ILIA algorithms presented in sections 3.1 , 5.3 to induce the set of endmembers.

For each image H_α in a dataset we calculate the dissimilarity between H_α and each of the remaining images in the dataset. These dissimilarities are represented as a vector $\mathbf{s}_\alpha = [s_{\alpha 1}, \ldots, s_{\alpha,n}]$, where n is the number of images in the dataset (2000 in our experiments) and $s_{\alpha,\beta}$ is the dissimilarity between the image H_α and the image H_β, with $\alpha, \beta = 1, \ldots, n$. Let us distinguish between $\mathbf{s}_\alpha^{GT}$ the vector of dissimilarities computed using the known ground truth endmembers, and $\mathbf{s}_\alpha^{IND}$ the vector of dissimilarities computed using the endmembers induced by one of the EIA (either N-FINDER or ILIA). We can define the ranking of the dataset relative to one of the images $\Omega_\alpha = [\omega_{\alpha,p} \in \{1, \ldots, n\}; p = 1, \ldots, n]$ as the set of image indices ordered according to increasing values of their corresponding entries in the dissimilarity vector $\mathbf{s}_\alpha$. That is, we sort in increasing order the components of $\mathbf{s}_\alpha$, and the resulting shuffled image indices constitute

73

(a)

(b)

(c)

(d)
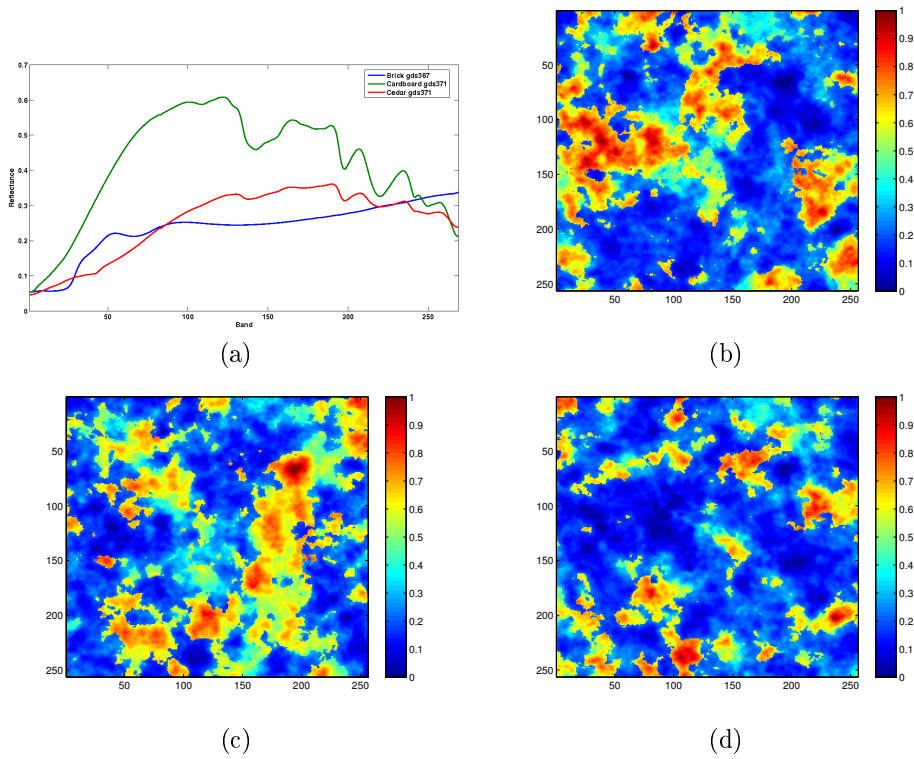
Figure 7.3: Example, from the 10-dataset, of an image's ground truth endmembers and abundance images used to generate it. (a) The three ground truth endmembers randomly selected from a collection of 10 spectra from USGS. (b, c, d) synthetic abundance images corresponding to each of the endmembers in (a).

Ω_α, so that $s_{\alpha,\omega_{\alpha,p}} \leq s_{\alpha,\omega_{\alpha,p+1}}$. We distinguish rankings Ω_α^{GT} and Ω_α^{IND} corresponding to the ground truth and induced dissmilarites, respectively. A query $Q_k(H_\alpha)$ is formulated as a search for the k most similar (less dissimilar) images H_β in the dataset respect to the image H_α. The set of returned images $T_k(H_\alpha)$ and the set of relevant images $V_k(H_\alpha)$ for a query $Q_k(H_\alpha)$ are defined as follows:

$$T_k(H_\alpha) = \Omega_{\alpha,k}^{IND} = \left[\omega_{\alpha,p}^{IND} \text{ s.t. } s_{\alpha,\omega_{\alpha,p}^{IND}} \leq s_{\alpha,\omega_{\alpha,k}^{IND}} \right], \tag{7.5}$$

$$V_k(H_\alpha) = \Omega_{\alpha,k}^{GT} = \left[\omega_{\alpha,p}^{GT} \text{ s.t. } s_{\alpha,\omega_{\alpha,p}^{GT}} \leq s_{\alpha,\omega_{\alpha,k}^{GT}} \right]. \tag{7.6}$$

This definition allows for the inclusion in the query answer of images whose dissimilarity is equal to the maximum one, thus allowing that the cardinality of both returned and relevant sets may be bigger than k. The Precision $P_k(H_\alpha)$ and Recall $R_k(H_\alpha)$ for a query $Q_k(H_\alpha)$ are standard performance measures in CBIR literature, they are defined as:

$$P_k(H_\alpha) = \frac{|V_k(H_\alpha) \cap T_k(H_\alpha)|}{|T_k(H_\alpha)|}, \tag{7.7}$$

$$R_k(H_\alpha) = \frac{|V_k(H_\alpha) \cap T_k(H_\alpha)|}{|V_k(H_\alpha)|}; \tag{7.8}$$

and the average Precision and Recall of the system for a query of size k are defined as:

$$P_k = \frac{1}{n} \sum_{\alpha=1}^{n} P_k(H_\alpha),$$

$$R_k = \frac{1}{n} \sum_{\alpha=1}^{n} R_k(H_\alpha).$$

7.4 Experimental results

We performed the following computational experiments: for each dataset of 2000 synthetic images we computed independently the Precision and Recall obtained using the endmembers induced by either EIA (N-FINDER and ILIA)

and either distance (Euclidean and SAM). Therefore, for each dataset we have four curves when we vary the size of the query in the range $[1, \ldots, 2000]$. We present these results in figures 7.4, 7.5 and 7.6 for the 5-dataset, 10-dataset and 20-dataset, respectively. Each figure is composed of two plots, the left and right plot correspond to the results obtained using the Euclidean and the SAM distance, respectively, to compute the image dissimilarity function. The expected behavior of the Precision as a funtion of the size of the query k is as follows: for small k it is near 1 (optimal performance), as k grows it decreases because allowing more responses introduces more uncertainty in the response, and for large k it comes back to 1 because increasingly almost all the images are accepted as response. We observe that in all combinations of dataset, distance and EIA the Precision follows this pattern. We can also observe that increasing the source endmember collection produces a deeper loss of Precision in the middle region of k values. Regarding the EIA considered, the ILIA algorithm consistently has better Precision values for small k but, when k is the middle region, N-FINDER has better Precision values until both converge to 1. This trend of the results is relatively independent of the distance considered or the dataset. The conclusion, regarding Precision results is that the approach is able to discriminate the underlying classes of images defined regarding their spectral content.

The Recall is low when k is small because it is more difficult to obtain a relevant image when we allow a small query, as the size of the query grows the Recall usually grows accordingly up to 1 when all the images are considered as answers. In the results of our computational experiment we find that the size of the collection of source endmembers has a definite effect in the Recall for small query sizes: increasing the source of endmembers increases the Recall. This may be due to the specific distribution of the source endmembers, with some specific physical material classes that have more than one representative. Nevertheless, the Recall performance is also relatively insensitive to the EIA applied, altough the N-FINDER gives better results again in the intermediate region of values of k, and ILIA is better for small queries.

Summarizing the goals of the computational experiments were:

- Test if the approach proposed can discover the classification of the images induced by the underlying ground truth endmembers. The experimental design, were the ground truth endmembers were known, allows to give a
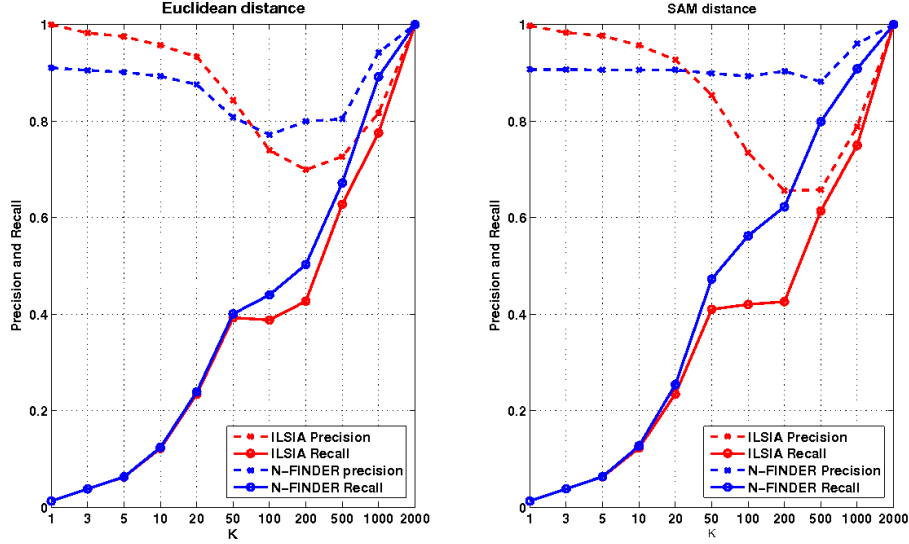
Figure 7.4: Precision and Recall results for the 5-dataset using Euclidean distance (left) and SAM distance (right) based dissimilarities.

positive response as far as the Precision values are very high.

- Test if the type of distance among endmembers has any specific effect on the system's performance: we found that the system performance is similar for Euclidean and SAM distance, so the approach is robust relative to this design element.

- Test if the EIA used has any impact on the system's performance: we found similar evolution of the performance indices with both EIAs tested, in spite of the fact that they rely on quite different fundamental approaches. We think that the proposed system will behave well using other EIAs, as far as it remains the same all along the system's life.

7.5   Conclusions

In this paper we introduce a CBIR system for databases of hyperspectral images using as image features the spectral characterization of the image provided by the endmembers of the image. The system uses an EIA to induce the endmembers from the data. To test its sensitivity to the EIA used, we tested two
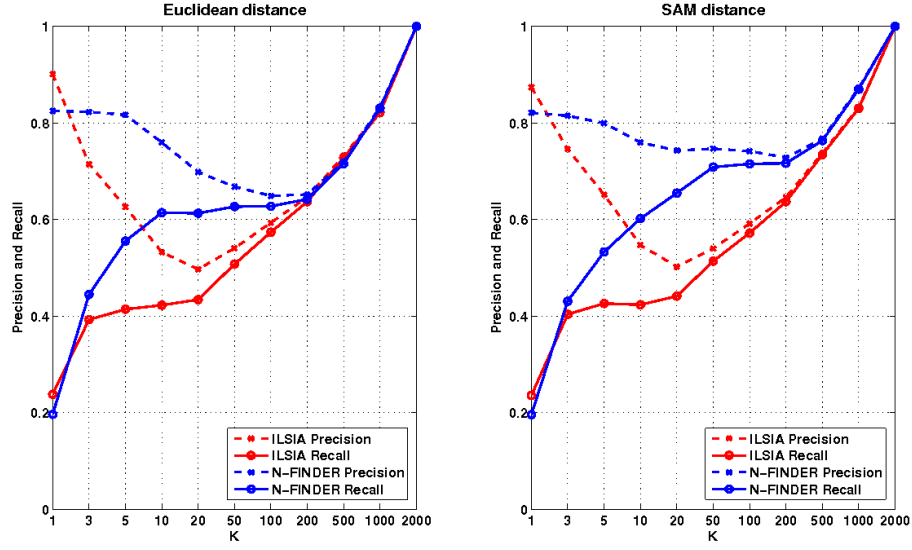
Figure 7.5: Precision and Recall results for the 10-dataset using Euclidean distance (left) and SAM distance (right) based dissimilarities.
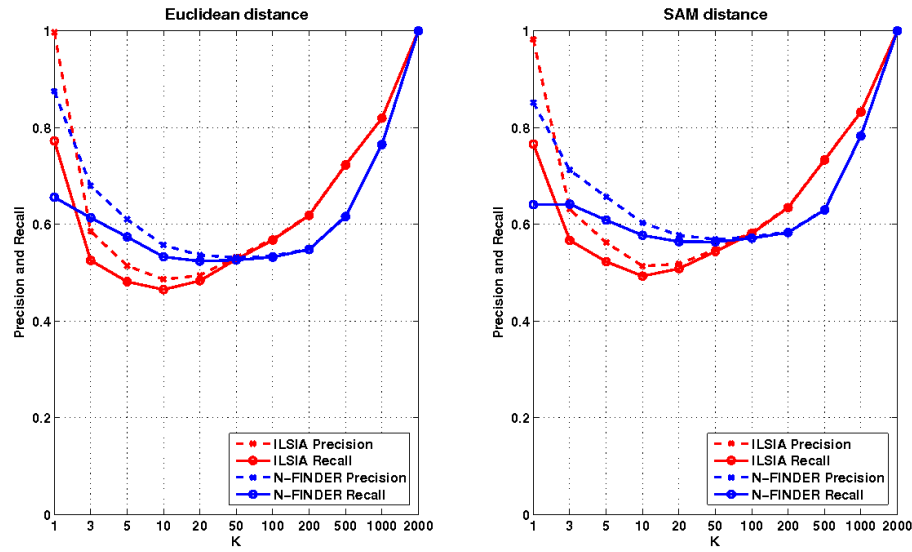
Figure 7.6: Precision and Recall results for the 20-dataset using euclidean distance (left) and SAM distance (right) based dissimilarities.

quite different algorithms, obtaining a rather similar response as measured by the evolution of the Precision and Recall of the answer to the queries. We also found that the system is rather insensitive to the endmember's type of distance employed. The results offered are based on several datasets of synthetic hyperspectral images, thus allowing us to give precise quantitative results. Overall, we have demostrated that the system can perform searches on databases of hyperspectral images. Among the paths of future research, the study of appropriate image normalization procedures is of paramount importance, because data variations due to the image capture conditions and parameters may have a big impact on system performance. Also we are very interested in the development of CBIR systems allowing for some relevance feedback from the user to guide the navigation over the image database [15, 18, 31, 54, 108, 57, 110, 111].

Chapter 8

A Morphological Cellular Automata

We discuss a definition of Morphological Cellular Neural Networks (MCNNs) where the state change operator are Auto-associative Morphological Memories (AMMs). The fast convergence property of the AMM and the shape of its fixed point set make the MCNN dynamics trivial. However, segmentation results are poor. We propose a Morphological Cellular Automata (MCA) with assured convergence to a state characterized by morphological dependences and independences between neighboring cell states. Cell dynamic rules test morphological dependence among neighboring cell's states. When neighboring cell's states are morphological dependent in the erosive or dilative sense, the morphologically dominant state colonizes the neighbor with morphological dependent state. The resulting configuration of cell states is composed of homogeneous regions whose boundaries are defined by the morphological independence relation. Results are given on image segmentation, where MCA cells correspond to image pixels.

The structure of the chapter is as follows. Section 8.1 reviews the definition and basic results of Cellular Neural Networks. Section 8.2 introduces the MCNN. Section 8.3 introduces the MCA. Section 8.4 gives results on image segmentation of MCNN and MCA. Finally, section 8.5 gives our conclusions.

8.1 Cellular Neural Networks

Cellular Neural Networks (CNNs) have been introduced in [20, 21, 22] as a powerful distributed computational model. A *standard CNN architecture* consists of an $M \times N$ rectangular array of cells $C(i,j)$ where (i,j) are the cell's Cartesian coordinates on a grid, $i = 1, 2, \ldots, M$, $j = 1, 2, \ldots, N$. The sphere of influence $S_r(i,j)$ of radius r of the cell $C(i,j)$ is the set of cells in grid site coordinates whose Manhattan distance is less than the radius:

$$S_r(i,j) = \left\{ C(k,l) \,\bigg|\, \max_{1 \le k \le M, 1 \le l \le N} \{|k-i|, |l-j|\} \le r \right\}, \tag{8.1}$$

where r is a positive integer.

A $M \times N$ *standard CNN* is defined by a rectangular grid of cells $C(i,j)$, each defined mathematically by its state and output equations:

$$\dot{x}_{ij} = -x_{ij} + \sum_{S_r(i,j)} A(i,j;k,l)\, y_{kl} + \sum_{S_r(i,j)} B(i,j;k,l)\, u_{kl} + z_{ij} \tag{8.2}$$

$$y_{ij} = f(x_{ij}) \tag{8.3}$$

where $x_{ij} \in \mathbb{R}$, $y_{ij} \in \mathbb{R}$, $u_{ij} \in \mathbb{R}$, and $z_{ij} \in \mathbb{R}$ are the state, output, input signal and threshold of cell $C(i,j)$, respectively. The output function is a non-linear function, corresponding to the activation function of conventional Artificial Neural Networks. The simplest one is the standard nonlinearity [20]: $f(x_{ij}) = \frac{1}{2}|x_{ij}+1| + \frac{1}{2}|x_{ij}-1|$. The evolution of the CNN cell states starts from an initial condition $x_{ij}(0)$, $i = 1, 2, \ldots, M$, $j = 1, 2, \ldots, N$. The synaptic connections $A(i,j;k,l)$ and $B(i,j;k,l)$ can be non-linear operators, denoted $A(i,j;k,l) \circ y_{kl}$ and $B(i,j;k,l) \circ u_{kl}$. They can be time variant, though usually they are assumed time invariant. If the synaptic connections are space invariant they are denote $A(k,l)$ and $B(k,l)$.

The CNN efectively implements a system of ordinary differential equations. The existence and uniqueness of solutions are guaranteed in the case of linear synaptic operators and continuous input signal, threshold and Lipschitz continuous non-linearity $f(x)$. If the initial state, input signal and threshold are bounded then the solution of the standard CNN is bounded.

The time and space invariant CNN with a linear output function implements a linear system that performs linear filtering of the input signal, usually an image.

Therefore they can be designed to perform edge detection, smoothing, contrast boosting and othe linear filtering operations on the input image [20]. Synaptic connections may have delays, so that they are systems with memory and inner states. The inclusion of delays allows to work on image sequences, performing temporal filtering for motion detection and other time based operations. Morphological image operators, such as erosion and dilation, can be approximated with appropriate nonlinearities.

8.2 The Morphological Cellular Neural Network (MCNN)

The aim of Morphological Cellular Neural Network (MCNN) is to perform the segmentation of images with multidimensional range, such as color, multispectral or hypspectral images, on the basis of the morphological properties of the pixel values. First, we consider the definition of MCNN along the lines of the conventional CNN described in section 8.1. Let us consider that cells $C(i,j)$ have a multidimensional state $\mathbf{x}_{ij} \in \mathbb{R}^d$. Let us denote $Y_{ij}(t)$ the set of the states of the neighboring cells in $S_r(i,j)$ at time t. The MCNN synaptic operators will be based on the erosive and dilative memories: W_{YY} and M_{YY}, respectively, built from $Y_{ij}(t)$[1]. According to the kind of the AMM, we can define dual MCNN dynamics. The erosive MCNN

$$\mathbf{x}_{ij}(t+1) = W_{YY} \boxdot \mathbf{x}_{ij}(t), \qquad (8.4)$$

and the dilative MCNN. The dynamics of the MCNN can be defined formally as follows:

$$\mathbf{x}_{ij}(t+1) = M_{YY} \boxdot \mathbf{x}_{ij}(t). \qquad (8.5)$$

The convergence of the MCNN dynamics is related to the properties of AMM fixed points. Although both memories share the same fixed point set they do not obtain the same result for non-fixed point vectors, therefore dynamics of equations (8.4) and (8.5) will produce divergent behaviors starting from the same initial conditions.

Will the MCNN converge to a fixed point global state in finite time?. If $\mathbf{x}_{ij}(t+1) \neq \mathbf{x}_{ij}(t)$ and the neighboring cells do not change $Y_{ij}(t) = Y_{ij}(t+1)$,

---

[1](We have taken the notation liberty $Y_{ij}(t) \equiv Y$)

then $\mathbf{x}_{ij}(t+2) = \mathbf{x}_{ij}(t+1)$ by equation (4.7) or (4.8), depending on the MCNN type. If there is a change in the neighboring cells, i.e. $Y_{ij}(t) \neq Y_{ij}(t+1)$, there will be a finite number of state changes before the cell's state reaches a fixed point even if all the neighboring cells change their states. However, there is not guarantee that no indefinite cycling behaviors may appear. For any two neighboring cells $C(i,j)$ and $C(k,l)$, a change in $\mathbf{x}_{ij}(t+1) \neq \mathbf{x}_{ij}(t)$ implies that $Y_{kl}(t+1) \neq Y_{kl}(t)$ so that it may happen that $\mathbf{x}_{kl}(t+2) \neq \mathbf{x}_{kl}(t+1)$, so that it is possible that $Y_{ij}(t+2) \neq Y_{ij}(t+1)$, and, as a consequence, we may have that $\mathbf{x}_{ij}(t+3) \neq \mathbf{x}_{ij}(t+2)$. This cyclic process will only be proved to converge if it is possible to prove that the sequences of fixed points $F(Y_{ij})$ and $F(Y_{kl})$ are ordered and have a limit value. To our knowledge, convergence to a stationary configuration of cell states of the erosive and dilative MCNN is an open question.

Let us examine the case when the erosive MCNN does converge to a stationary global configuration of cell states, corresponding dual assertions may apply to the dilative MCNN. In the stationary configuration we have that each cell state is a fixed point of the AMM constructed with the corresponding:

$$\mathbf{x}_{ij} = W_{Y_{ij}Y_{ij}} \boxtimes \mathbf{x}_{ij}, \ i = 1, 2, \ldots, N; j = 1, 2, \ldots, M.$$

From the review of the section 4.1, this condition holds when some of the following situations arise:

- $\mathbf{x}_{ij} = \mathbf{x}_{kl}$ for at least one $(k,l) \in S_r(i,j)$. If all the neighboring cells have the same state, then the cell is in the middle of an homogenous region of the MCNN configuration. If some of the neighboring cells have different states, then it is in the boundary between regions.

- $\mathbf{x}_{ij}$ is lattice dependent of Y_{ij}. That means that stationary regions can be composed of cell states which are different. Stationarity would be due to some mutuall lattice dependence. This is a drawback from the image segmentation point of view, unless some kind of equivalence relation can be defined allowing to identify the same region.

The erosive and dilative MCNN, with dynamics defined by equations (8.4) and (8.5) respectively, have a big potential appeal, the segmentation of multispectral images based on morphological properties. There are two major drawbacks: (1) the risk of indefinite convergence and (2) the stationary state is composed of

84

mutually lattice dependent cell states. Unless some kind of equivalence relation could be defined, they would not constitute homogeneous segmentation regions. Besides, there is no evident way to compose both erosive and dilative MCNN dynamics on the same image that may help to improve the convergence to homogeneous regions.

8.3 The Morphological Cellular Automata (MCA)

We are looking for the detection of homogeneous regions. It seems from the discussion above and the results in section 8.4 that lattice independence is not strong enough to define easiliy identifiable regions. We return to the concept of morphological independence. Our aim is to obtain as bondaries morphological independent neighborhs, while using morphological dependence to "assimilate" neighboring pixels. This Morphological Cellular Automata (MCA) is summarized in Algorithm 8.1.

Let us define $\left\{\mathbf{f}\left(i, j\right) \in \mathbb{R}^d; i = 1, .., N; j = 1, .., M\right\}$ the RGB, multispectral or hyperspectral image, $\boldsymbol{\mu}$ and $\boldsymbol{\sigma}$ the vectors of the mean and standard deviations of each band computed over the image, α the band-wise equivalence interval factor. The addition and substraction of $\alpha\boldsymbol{\sigma}$ to each state vector allows to define an interval of equivalence between cell states intended to overcome over-segmentation when morphological independence is due to noise conditions. The image is preprocessed as in the previous algorithm so that each pixel is a zero mean vector $\{\mathbf{f}^c\left(i, j\right) = \mathbf{f}\left(i, j\right) - \boldsymbol{\mu}; i = 1, .., N; j = 1, .., M\}$. Algorithm 8.1 is initialized with this centered image. It repeats the computation of the new configuration $X\left(t\right)$ until convergence is reached. Convergence consists in the absence of changes. Cells are considered in pairs, and their state is changed according to the following reasoning: If there is morphological dependence (either erosive or dilative) the dominant cell assimilates the dependent cell. Previously, we consider the existence of an equivalence interval defined on the basis of the band-wise variance. If the neighboring cell falls in this interval, then the one with the greatest norm dominates, regardless of morphological independence/dependence relation.

Algorithm 8.1 Morphological Cellular Automata dynamics

1. Initialize the MCNN state to the image pixel values: $X(0) = \{\mathbf{x}_{ij}(0) = \mathbf{f}^c(i,j)\}$.

2. Repeat until convergence $X(t) = X(t+1)$, for increasing t:

   (a) For each pair of neighboring cells (i,j), $(k,l) \in S_1(i,j)$:

      i. compute the upper and lower bounds of the interval defined assuming independent Gaussian noise sources $\mathbf{x}_{ij}^- = \mathbf{x}_{ij}(t) - \alpha\boldsymbol{\sigma}$ and $\mathbf{x}_{ij}^+ = \mathbf{x}_{ij}(t) + \alpha\boldsymbol{\sigma}$

      ii. if $(\mathbf{x}_{ij}^- < \mathbf{x}_{kl}(t) < \mathbf{x}_{ij}^+$ and $\|\mathbf{x}_{ij}(t)\| < \|\mathbf{x}_{kl}(t)\|$) or $(\mathbf{x}_{ij}^- \leq \mathbf{x}_{kl}(t))$ or $(\mathbf{x}_{kl}(t) \geq \mathbf{x}_{ij}^+)$

         • then $\mathbf{x}_{ij}(t+1) = \mathbf{x}_{kl}(t+1) = \mathbf{x}_{kl}(t)$,
         • else $\mathbf{x}_{ij}(t+1) = \mathbf{x}_{ij}(t)$; $\mathbf{x}_{kl}(t+1) = \mathbf{x}_{kl}(t)$

8.4 Results on image segmentation

We first present computational results of the erosive MCNN[2] showing the convergence features that can be expected in practice. The experimental image is the well known "clown" image featured in Matlab. Figure 8.1 plots the amount of change, measured by the difference image norm, introduced by each iteration. The convergence is very fast. Besides the changes are very isolated, as shown in figure 8.2, and they do not produce regions of homogeneous colors as desired for a segmentation procedure. We do not reproduce the final image because it does not give any additional information.

The previous results serve as a motivation for the definition of the MCA in section 8.3. In this section we present image segmentation obtained by the MCA algorithm 8.1 whose cells correspond to the image pixels. The cell state is given by the pixel color after the MCA iterations. Initial state of the MCA is given by the actual image to be segmented.

The experimental image is the well known "lena" image. To reduce the computational burden, we have downsampled it to a 64×64 size. The actual image used in the experiments is shown in figure 8.3. The segmentation obtained with the algorithm of the MCA without noise tolerance is shown in figure 8.4. This segmentation is obtained when the algorithm reaches an invariant state.

---

[2]We have made available the code for MCNN at http://www.ehu.es/ccwintco/uploads/a/a6/MCNN_code.zip
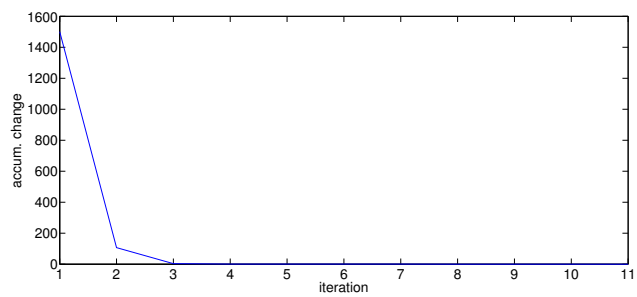
Figure 8.1: Plot of the amount of change introduced by each MCNN iteration in its application to the clown image
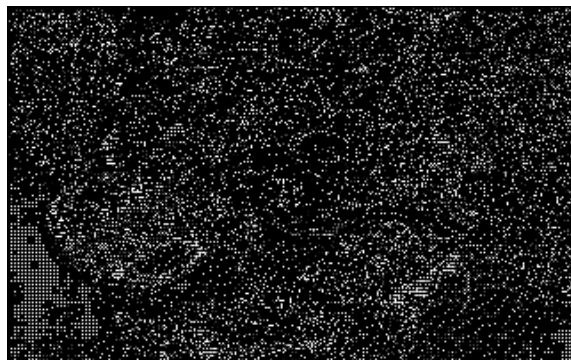

Figure 8.2: Location of the pixels that have suffer some change by the application of erosive MCNN to the clown image

The colors shown correspond to the morphologically independent colors that have propagated from their original pixel sites, absorving morphologically dependent pixel sites. The main features of the image can be distinguished in this segmentation. Observe that some regions of similar color are not identified because they are separated by connected regions of an morphologically independent color. For comparison we show in figure 8.5 the results of the identification of color regions performed by standard Color Quantization algorithms based on the minimization of the quantization distortion. To give an idea of how the spatial process has developed to reach the segmentation of figure 8.4 we have kept track of the original pixel position whose color has been propagated as a morphologically dominant color. In figure 8.6 we show these regions in the following form. Each pixel site (i, j) is identified by the a number given by the function $n(i, j) = 64j + i$. A table with those values is built at the begining of the MCA evolution. Each time that a cell propagates its color to a neighboring cell, the corresponding entries in the table are updated. Figure 8.6 shows the final distribution. Note that the regions in this figure do not match exactly to the ones appreciated in figure 8.4. That is, the same color, from different parts of the image ends up merging in a single region in an autonomous way. Further, the histogram of pixel ids shown in figure 8.7 demonstrate that the evolution of the MCA converges to coherent spatial aggregations of the pixels. At the beginning of the MCA evolution, this histogram is uniform, each entry with a 1 value. The MCA evolution concentrates most of the pixel ids in some values, corresponding to the propagation of the values of morphologically dominant colors until boundaries of morphological independence are settled down.

The activation of the noise related filter has the effect of allowing the fusion of regions of morphologically independent colors. As can be appreciated in figure 8.8, increasing α decreases the number of identified regions until all detail is lost. The effect on the distribution of the propagation regions can be observed in figure 8.9, where the number of dominance regions decreases as in figure 8.8 when the parameter α increases. Finally, figure 8.10 shows how the histogram of pixel-ids evolves towards a more concentrated distibution, which may end in a couple of peaks when α is large enough.

Figure 8.3: Original Lena image

Figure 8.4: Segmentation of the lena image obtained without noise parameter

(a)   (b)

Figure 8.5: Color quantization into 8 colors (a) and 32 colors (b).
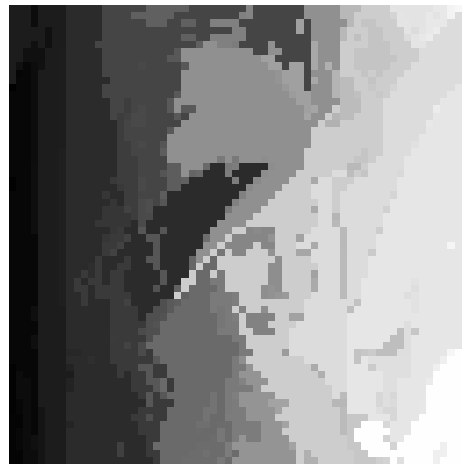
Figure 8.6: Regions in the image according to morphological dominance obtained by the MCA without noise filter.
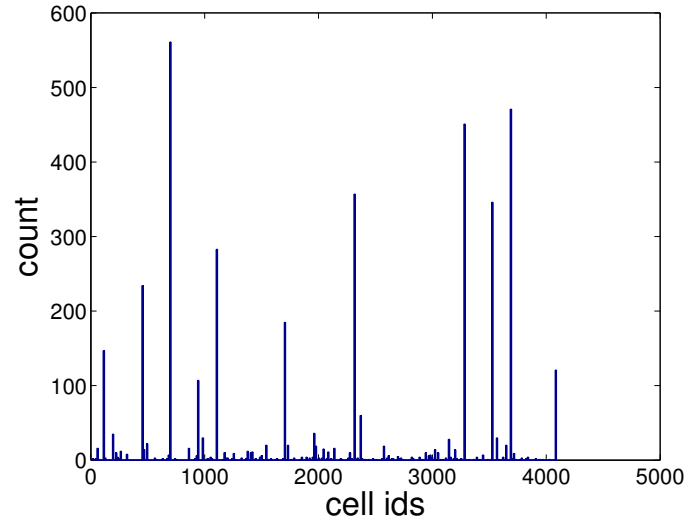
Figure 8.7: Histogram of pixel-ids showing the aggregation of pixels into spatially coherent regions.
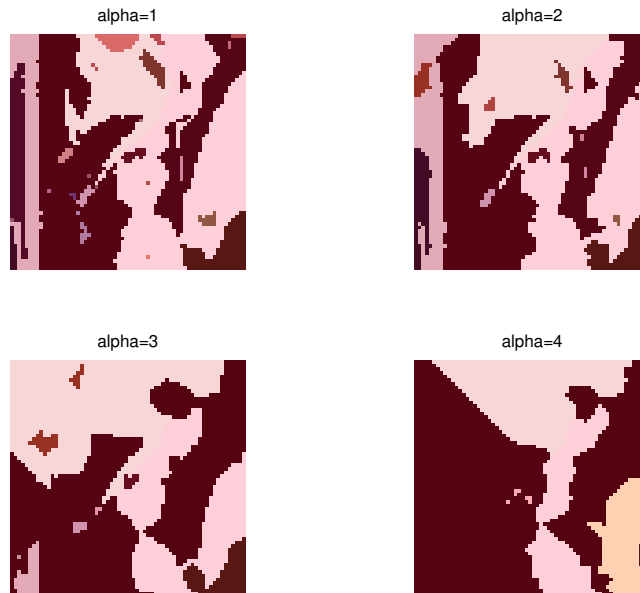
Figure 8.8: Evolution of the segmentation obtained increasing the parameter α

91
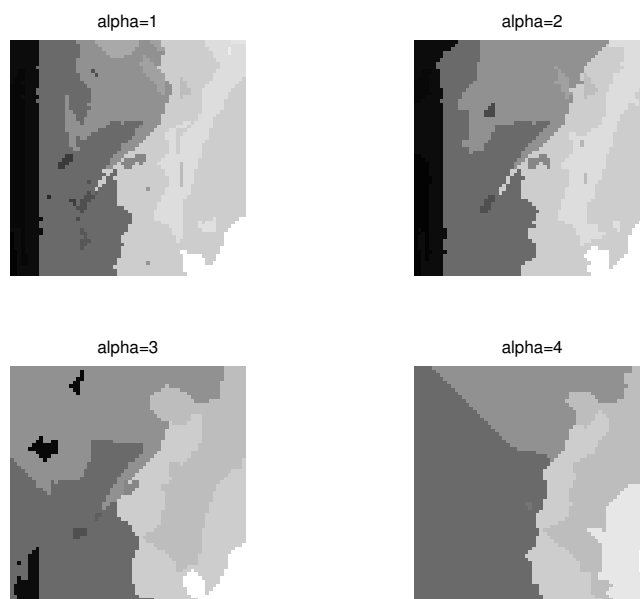
Figure 8.9: Evolution of the dominance regions increasing parameter α
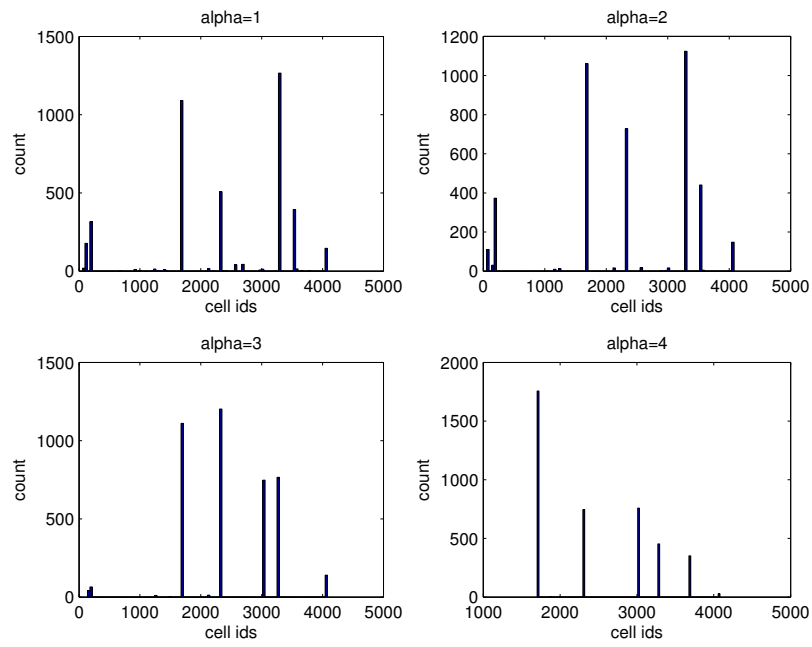
Figure 8.10: Evolution of the histogram of pixel-ids as the parameter α increases

8.5 Conclusions

We have first proposed a MCNN based on the application of AMMs as synaptic operators. The approach has a very fast convergence but introduces little changes in the image and does not detect homogenous regions for segmentation. Therefore, we have introduced a MCA based on the morphological dependence and independence notions. The goal is to obtain homogeneous regions from morphological dependent pixels, with the boundary of such regions defined by the morphological independence between neighboring pixels. We have shown that the approach produces consistent connected regions of homogeneous colors. Besides introducing equivalences between pixels based on confidence intervals defined on the variances allows to control the resolution of the segmentation.

Chapter 9

A Single Individual
Evolutionary Strategy.

9.1   Introduction

This chapter is devoted to the description of Evolutionary Strategies (ES) applied to the task of Endmember Induction from Hyperspectral images. The proposal includes a conventional ES and a Single Individual Evolutionary Strategy (SIES). We differenciate them accordingly to the distinction in modelling paradigms for Evolutionary Algorithms given by both the so-called Pittsburg and Michigan approaches. The common baseline is that we want to solve some optimization problem encoded by a set of variables which describe the solutions to the problem and a fitness function that quantifies the optimality of the solution provided by some precise values of the variables. Evolutionary algorithms are population based random search algorithms. Therefore, they have a population of individuals as the computational state vector. The search proceeds by proposing random new populations by the application of randomized operators on the population individuals. These new populations are evaluated according to the fitness function and a selection is performed to proceed to the next generation. Regardless of the nature of the variables (real or discrete valued), and any other features of the evolutionary algorithm to be designed to solve the problem, there is a basic design choice to be done: the meaning of each individual and that of the whole population. The Pittsburg approach equates

95

each individual with a complete representation of the problem, therefore the fitness function evaluates each individual and the next generation is obtained as a random selection of the best individuals on the basis of the fitness function values. The Michigan approach models the problem using a complete population, so that each individual incorporates one variable or a subset of variables of the problem model. The first implication of this approach is that there are two kinds of fitness function. One is related to the problem of evaluating the population as a whole, measuring the progress towards the solution. The other fitness function is applied to evaluate the contribution of each individual towards the optimization of the global population fitness. This local individual fitness is used for individual selection in order to build the next generation. Proving the convergence of the algorithm involves the consideration of both fitness functions, where? the local individual optimization implies the global fitness optimization, which is a paradigmatic case of cooperation.

In this chapter we explore the definition of a conventional Evolutionary Strategy (ES) following the Pittsburg approach, and Single Individual Evolutionary Strategy (SIES) following the Michigan approach [6, 66]. The "single individual" refers to the fact that the whole population represents a single solution to the problem. We expect that the SIES approach will give comparable (or better) results with less computation.

The structure of the chapter is as follows: Section 9.2 describes the fitness function tailored to the problem of endmember induction for spectral unmixing in remote sensing multispectral and hyperspectral images. Section 9.3 describes the evolutionary strategy (ES) following the Pittsburg approach. Section 9.2 describes the Michigan approach, single endmember evolutionary strategy (SIES). Section 9.5 presents some experimental results of the proposed algorithm and the competing conventional evolution strategy. Section 9.6 gives our conclusions in this chapter.

9.2 The fitness function for endmember induction

In this section we describe the fitness function to be maximized by both the standard Evolutionary Strategy (ES) and the Single Individual Evolutionary Strategy (SIES) tailoring them to the problem of inducing a set of endmembers

from the image data. As discussed in Chapter 3, the endmembers of a given hyperspectral image, under the linear mixture assumption, correspond to the vertices of the minimal simplex that encloses the data points [24, 52, 39]. Therefore, the result of the endmember induction algorithms must be a set of vertices that define a convex region. This defines also which is the computational state of the algorithms, which must be specified by the endmembers induced from the hyperspectral image. The positive and full addition properties are the basic restriction to fulfill, therefore they are the basis for the definition of the fitness function. We introduce the reconstruction error as the regularization term in the fitness function. We formalize the fitness function as follows.

Let us denote $\mathbf{f} = \left\{ \mathbf{f}\left(i, j\right) \in \mathbb{R}^d; i = 1, .., n; j = 1, .., m \right\}$ a $d-$band hyperspectral image, which can be considered as a $d \times (n \cdot m)$ matrix, and $\mathbf{S}$ is the $d \times M$ matrix whose colums are the set of M endmembers whose fitness is to be quantified. Matrix $\mathbf{S}$ corresponds to an individual of the ES and to the whole population of the SIES.

Let it be

$$\widehat{\mathbf{a}} = \left\{ \widehat{\mathbf{a}}\left(i, j\right) \in \mathbb{R}^M; i = 1, .., n; j = 1, .., m \right\}, \tag{9.1}$$

and

$$\varepsilon = \left\{ \varepsilon^2\left(i, j\right) \in \mathbb{R}^M; i = 1, .., n; j = 1, .., m \right\} \tag{9.2}$$

the endmember fractional abundance estimations and reconstrucion error, respectively, computed applying at each pixel equations (9.3) and (9.4) as defined in Chapter 3:

$$\widehat{\mathbf{a}}\left(i, j\right) = \left(\mathbf{S}^T \mathbf{S}\right)^{-1} \mathbf{S}^T \mathbf{f}\left(i, j\right), \tag{9.3}$$

$$\varepsilon^2\left(i, j\right) = \left\| \mathbf{f}\left(i, j\right) - \mathbf{S}\widehat{\mathbf{a}}\left(i, j\right) \right\|^2. \tag{9.4}$$

The maximization of the fitness function corresponds to the minimization of the residual error:

$$\sum_{i=1}^{n} \sum_{j=1}^{m} \varepsilon^2\left(i, j\right).$$

The functional includes terms corresponding to the positive and sum to one constraints. The positivity constraint is modelled by the following term:

$$\sum_{i=1}^{n} \sum_{j=1}^{m} \sum_{\mathbf{k}} \left| \widehat{a}_k\left(i, j\right) \right|,$$

97

where $\mathbf{k} = \{k \, |\widehat{a}_k \, (i,j) < 0\}$. That is, the term corresponds to the addition of the absolute magnitude of the abundance coefficients that violate the positivity constraint. The addition to one constraint is modelled by the following term:

$$\sum_{i=1}^{n} \sum_{j=1}^{m} \left(1 - \sum_{k=1}^{M} \widehat{a}_k \, (i,j)\right)^2,$$

that is, we add up the differences to the additivity to one constraint. The complete functional is formalized as follows:

$$
\begin{aligned}
C\left(\mathbf{f}, \mathbf{S}\right) \;\; = & \;\; \sum_{i=1}^{n} \sum_{j=1}^{m} \varepsilon^2 \, (i,j) + \sum_{i=1}^{n} \sum_{j=1}^{m} \left(1 - \sum_{k=1}^{M} \widehat{a}_k \, (i,j)\right)^2 \\
& + \sum_{i=1}^{n} \sum_{j=1}^{m} \sum_{\mathbf{k}} |\widehat{a}_k \, (i,j)| \,,
\end{aligned}
\tag{9.5}
$$

where $\mathbf{k} = \{k \, |\widehat{a}_k \, (i,j) < 0\}$. Note that all the terms have similar magnitude, because they consist in the summation of small values along the image. The fitness function maximized by the evolutionary strategies is defined as its inverse:

$$F\left(\mathbf{f}, \mathbf{S}\right) = \frac{1}{C\left(\mathbf{f}, \mathbf{S}\right)}.\tag{9.6}$$

9.3 The Evolutionary Strategy

The ES employed as the baseline algorithm for endmember search is a conventional $(\mu + \lambda)$- ES [7, 8, 9, 10, 2, 12, 42, 65]. The general structure of a $(\mu + \lambda)$-ES is as follows:

- The individuals represent complete solutions whose quality can be measured by the fitness function. Each population at any generation has μ individuals. Each individual has an associated mutation parameter, which is the standard deviation of a normal distribution.

- To compute the next generation of the population, we start by selecting λ parents from the current population on the basis of their fitness function values. The selection method is the roulette wheel.

98

Algorithm 9.1 $(\mu + \lambda)$-Evolution Strategy for endmember induction from a hyperspectral image.

Input: the hyperspectral image $\mathbf{f}$, the number of endmembers M.
Compute the mean and standard deviation per band $\mathbf{m_f}$ and $\boldsymbol{\sigma_f}$.
Generate the initial population $P_0 = \{(\mathbf{S}_i, \boldsymbol{\sigma}_i); i = 1, .., \mu\}$; initially $\boldsymbol{\sigma}_i = \boldsymbol{\sigma_f}$.
Each individual is a sample of multivariate normal distribution $\mathbf{S}_i \sim N(\mathbf{m_f}, \boldsymbol{\sigma_f}\mathbf{I})$
While not Stopping Condition

1. Compute the fitness for each individual $\{\phi_i = F(\mathbf{f}, \mathbf{S}_i); i = 1, .., \mu; \mathbf{S}_i \in P_t\}$ applying equation (9.6).

2. Select $P_t^{(p)} = \{(\mathbf{S}_i, \boldsymbol{\sigma}_i); i = 1, .., \lambda\}$ parents from P_t by a roulette wheel based on the individual fitness ϕ_i.

3. Update the variances in $P_t^{(p)}$: $\boldsymbol{\sigma}'_i = \boldsymbol{\sigma}_i \cdot \exp(\tau \cdot \xi)$, where ξ is a random sample of the multivariable standard normal distribution $\xi \sim N(\mathbf{0}, \mathbf{1})$. The product is a Hadamard product.

4. Generate mutations $P_t^{(m)} = \{(\mathbf{S}_i + \zeta_i, \sigma'_i); i = 1, .., \lambda\}$, where each ζ_i is a random sample $\zeta_i \sim N(\mathbf{0}, \boldsymbol{\sigma}'_i\mathbf{I})$

5. Compute the fitness $\left\{\phi_i^{(m)} = F(\mathbf{f}, \mathbf{S}_i); i = 1, .., \lambda\right\}$ for each mutated individual $\mathbf{S}_i \in P_t^{(m)}$

6. Elitist selection: the next generation population P_{t+1} is composed by the μ individuals selected from $P_t^{(m)} \cup P_t$ according to the best fitness

- The parents' mutation parameters are updated. The mutated offspring of each selected parent is generated as a random perturbation of the parent adding a sample of a normally distributed (multivariate) random variable with zero mean and standard deviation given by the mutation parameter.

- The fitness of the mutated offspring is computed.

- The μ best individuals among the parents and mutated offspring are selected for the next generation.

Regarding the convergence of the algorithm, the mutation updating algorithm is critical to obtain a good exploration of the solution space. The algorithm is intended to be self-adaptive in the sense that not only the best individual but also the best mutation parameter are selected and evolved. Besides, the algorithm is elistist, meaning that the best found solution is always preserved. Elitism guarantees that the algorithm is at least a local optimization algorithm, and that, if the solution space is appropriately sampled, it can be a global optimization algorithm.

The pseudocode of the ES algorithm for endmember induction from a hyperspectral image, using the above definitions, is given in Algorithm 9.1. We denote $\mathbf{m_f}$ and $\boldsymbol{\sigma_f}$ the vectors whose components are the mean and standard deviation of each band computed over the image. Population individuals are hypothetical sets of endmembers, and their mutation vector variances $P_t = \{(\mathbf{S}_i, \boldsymbol{\sigma}_i); i = 1, .., \mu\}$. Vector variances are the mutation variances *per* band. The mutation variances are initialized as the global image standard deviations. The initial population is generated as a collection of samples of a random vector following a multivariate normal distribution centered in the image's spectral mean. The ensuing generations are produced by the conventional schema of additive random gaussian perturbations and self-adaptation of the mutation variances of the $(\mu + \lambda)$-ES. The fitness function is given by equation (9.6). The specificity of the algorithm lies in the fact that all the multivariate normal distributions involved have diagonal covariance matrices, whose diagonal values are given by the deviation parameters.

Algorithm 9.2 Single Individual Evolution Strategy for endmember induction.

Input: the hyperspectral image $\mathbf{f}$, the number of endmembers M.

Compute the mean and standard deviation per band $\mathbf{m_f}$ and $\boldsymbol{\sigma_f}$.

Generate the initial population $P_0 = (\mathbf{S}, \boldsymbol{\sigma}) = (\{\mathbf{s}_1, .., \mathbf{s}_M\}, \{\boldsymbol{\sigma}_1, .., \boldsymbol{\sigma}_M\})$, where $\mathbf{S} \sim N(\mathbf{m_f}, \boldsymbol{\sigma_f})$, and, initially, $\boldsymbol{\sigma}_k = \boldsymbol{\sigma_f}$.

While not Stopping Condition

1. Compute the global population fitness $\phi_t^p = F(\mathbf{f}, \mathbf{S})$.

2. Compute the local individual fitness $\{\phi_k = F(\mathbf{f}, \mathbf{s}_k) ; k = 1, .., M\}$

3. *For a maximum of λ attempts*

    (a) Select $(\mathbf{s}_k, \boldsymbol{\sigma}_k)$ as a parent from P_t by a roulette wheel based on the partial individual fitness $\{\phi_k\}$.

    (b) Update the variance vector $\boldsymbol{\sigma}_k' = \boldsymbol{\sigma}_k \cdot \exp(\tau \cdot \xi)$, where ξ is a random sample $\xi \sim N(\mathbf{0}, \mathbf{1})$.

    (c) Generate a mutation $(\mathbf{s}_i' = \mathbf{s}_i + \zeta_i, \sigma_i')$, where ζ_i is a random sample $\zeta_i \sim N(\mathbf{0}, \boldsymbol{\sigma}_i')$.

    (d) Let it be $\mathbf{S}'$ the set of endmembers where we replace $\mathbf{s}_k$ with $\mathbf{s}_k'$. Compute the global global mutated population fitness: $(\phi_t^p)' = F(\mathbf{f}, \mathbf{S}')$.

    (e) Elitism: If $(\phi_t^p)' > \phi_t^p$ then $P_{t+1} = (\mathbf{S}', \sigma')$, where the mutated individual is included in the new population.

9.4 The Single Individual Evolutionary Strategy

The pseudocode of our proposed SIES is given in algorithm 9.2. The SIES follows the Michigan approach, therefore the whole population is a solution to the problem, each individual is a single hypothetical endmember. The fitness function follows the same expression (9.5) as the ES, however in the SIES it is evaluated at the global and local level.

At the global level, the fitness function is computed over all the abundance images and corresponding reconstruction errors obtained with the set of endmembers represented by the entire population. The local individual fitness are evaluated using the abundance image associated with the individual endmember. We denote $F\left(\mathbf{f}, \mathbf{s}_k\right)$ the computation of the local fitness function using only the k-th abundance image. These partial fitness are used to select the individual which is to be mutated. Another difference with the conventional $(\mu + \lambda)$-ES is that the mutations are proposed sequentially instead of being computed simultaneously. Mutations are tested in order, up to a maximum of λ attempts. The selected individual mutation is introduced in the population. The global fitness of this mutated population is computed, which involves computing the abundance images. If the mutated population global fitness is greater than the present population global fitness, then the mutated population becomes the new population for the next generation. Elitist selection implies the monotonic growth of the population global fitness function. The algorithm is a global optimal search algorithm if the mutation explores adequately the solution space. The stopping condition corresponds to a single generation without offspring accepted. The convergence of the $(\mu + \lambda)$-ES usually lead to populations where a single individual is replicated many times, until colonizing the entire population. This phenomenon does not happend in the SIES.

Regarding computational cost, the SIES is faster than the conventional $(\mu + \lambda)$-ES, because the size of the population is restricted to the number of endmembers. Also the number of abundance image computations is lower for two reasons: one is the smaller size of the population, the other is that the number of mutations tested is lower because the process of testing mutations usually finds an improvement before the limit of λ attempts.

9.5   Experimental results

In this section we present results of the application of the $(\mu + \lambda)$-ES and SIES evolutionary strategies on two real world multispectral images described in Appendix B. The first image, provided by the Catalonian Remote Sense Institution (CREAF), is a labelled multispectral CASI image. The second is the Indian Pines hyperspectral image published by the prof. Landgrebe's research group. The settings of the algorithm parameters were the same in both cases. The ES population size was $\mu = 10$, the number of endmembers per individual was $M = 5$ and the number of mutations allowed was $\lambda = 30$. The SIES number of endmembers was $M = 5$, and the maximum number of tested mutations was $\lambda = 30$. The quantitative comparison involves the best fitness of the $(\mu + \lambda)$-ES population among the μ individual against the whole population fitness of the SIES.

9.5.1   The CREAF image

The figure 9.1 shows the plot of an evolution instance of the best individual fitness for the conventional $(\mu + \lambda)$-ES and the global fitness of the SIES. The improvement of the SIES over the ES is remarkable, moreover if we take into account that SIES is faster than $(\mu + \lambda)$-ES and performs much less exploration. The reason for this improvement may be related to the additional randomization introduced by the selection of mutation parents based on their isolated abundance images. However, the relation of the partial fitness and the global fitness does not ensure that choosing the best partial fitness individual will lead to improvements in the global fitness. The endmembers obtained by the $(\mu + \lambda)$-ES and the SIES algorithms are shown in figures 9.2 and 9.3, respectively. It can be appreciated that the obtained set of endmembers does not differ very much one from the other, however the ones resulting from the conventional ES are more ragged than the ones resulting from the SIES.

The qualitative results are given by the abundance images computed using the endmember spectra found by both approaches. They are shown in figures 9.4, 9.5, 9.6 and 9.7. The abundance image intensities have been normalized to the [0,255] interval for visualization. Black corresponds to negative abundance values.

A remarkable feature of both sets of results is the outlining of the fine spatial
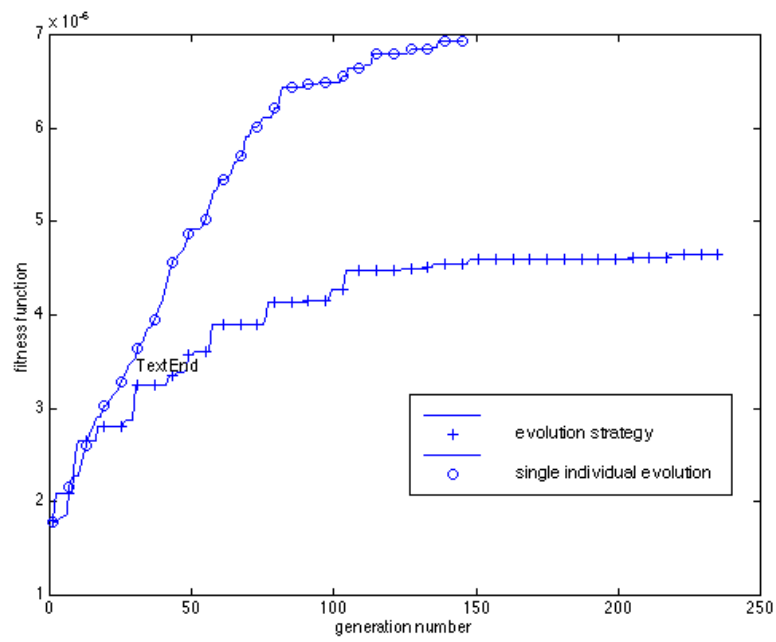
Figure 9.1: Plot of the evolution of the fitness function of the best individual of the $(\mu + \lambda)$-ES and the global population fitness of the SIES searching for endmembers on the CREAF image.
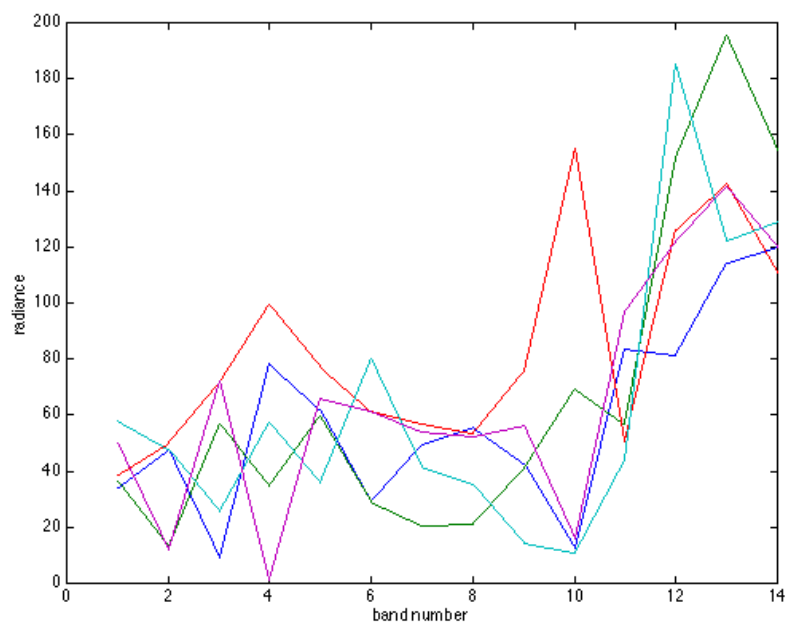
Figure 9.2: Endmembers obtained by the $(\mu + \lambda)$-ES strategy on the CREAF image
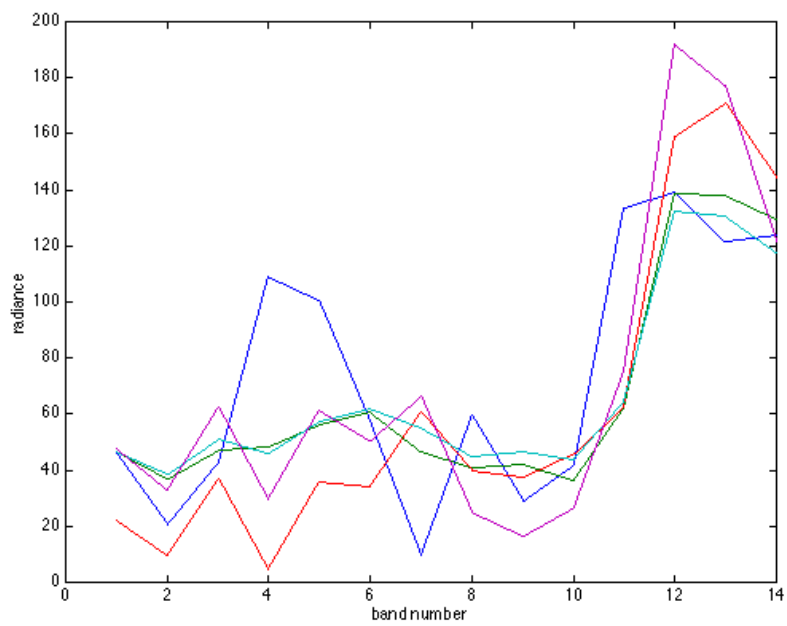
Figure 9.3: Endmemembers obtained by the SIES on the CREAF image.

structure, which is not specified in the ground truth image B.4. The ground truth provides a rough approximation to the image segmentation. Roads which are not well specified in the ground truth are apparent in the abundance images. Also buildings and urban structures are well defined. Some rooftops seem to provide a very strong response differentiated from the other urban structures. The computed endmember spectra can be interpreted as unsupervisedly induced detectors of specific materials that may deserve further analysis, and their abundance images as unsupervised segmentations uncovering the fine spatial structure of the hyperspectral image.

If we concentrate our examination of the images on each ground truth cover class we find the following facts:

- The urban cover is well detected by both approaches. The SIES abundance #3 seems to provide a negative image of the urban structure and the roads. The SIES abundance #4 shows good positive detection of the urban structures, with some confusion with the meadows. SIES abundance #2 is also a negative detection of urban areas showing confusion with the meadows. The $(\mu + \lambda)$-ES abundances #3 and #5 provide a good positive detection of urban structures and roads butconfuse with meadows. The $(\mu + \lambda)$-ES abundance #2 provides the negative detection. The $(\mu + \lambda)$-ES abundance #1 is a good detector of some rooftop structures.

- The vegetal cover is generically detected by some abundances which showed negative detection of urban areas. They are $(\mu + \lambda)$-ES abundance #2, and SIES abundances #2, #3, and #5.

- The meadows are confused in some cases with urban structures as said before.

- Evergreen and deciduous trees are well detected as a single cover in SIES abundance images #2 and #5, and in $(\mu + \lambda)$-ES abundance image #2.

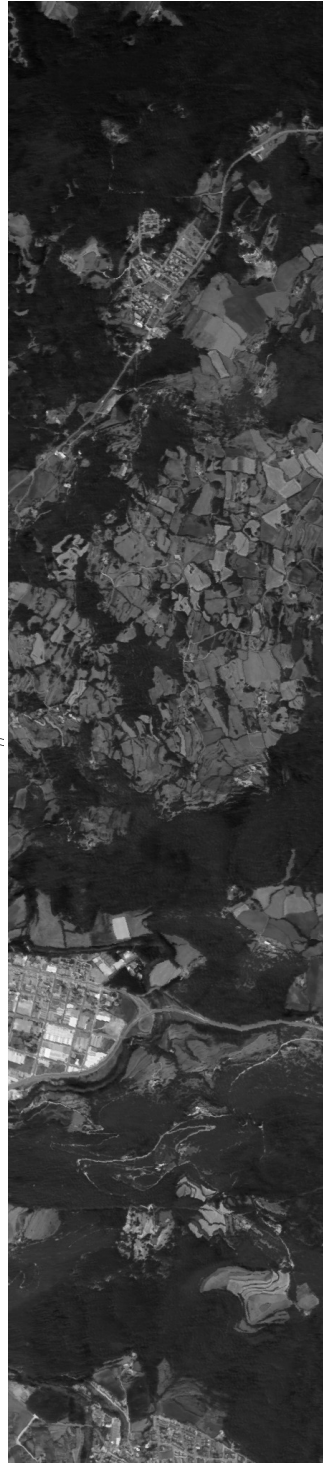### 9.5.2 The Indian Pines image

The second set of results were obtained on the Indian Pines image (Appendix B). We show in figure 9.8 an instance of the evolution of the $(\mu + \lambda)$-ES best fitness and of the global population fitness of the SIES when applied to this

#1
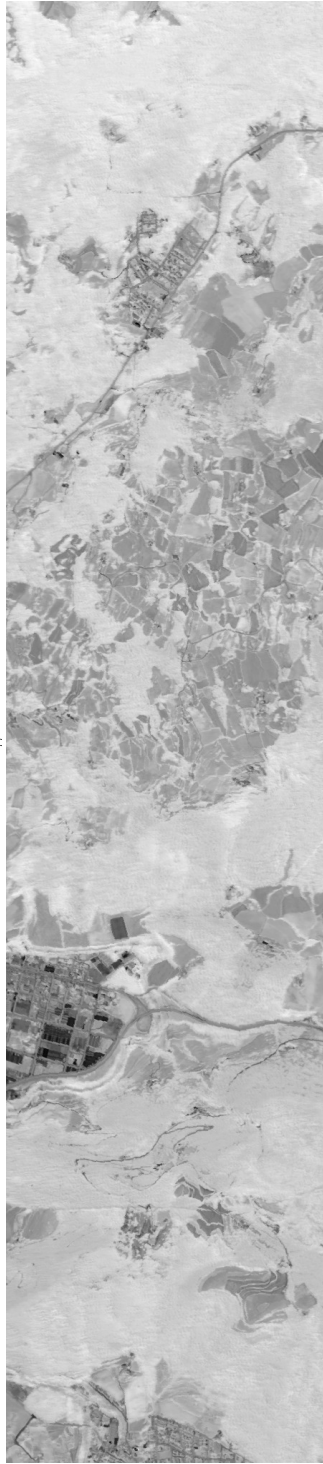
#2

#3

Figure 9.4: Abundance images corresponding to the endmembers discovered by the $(\mu + \lambda)$-ES on the CREAF image
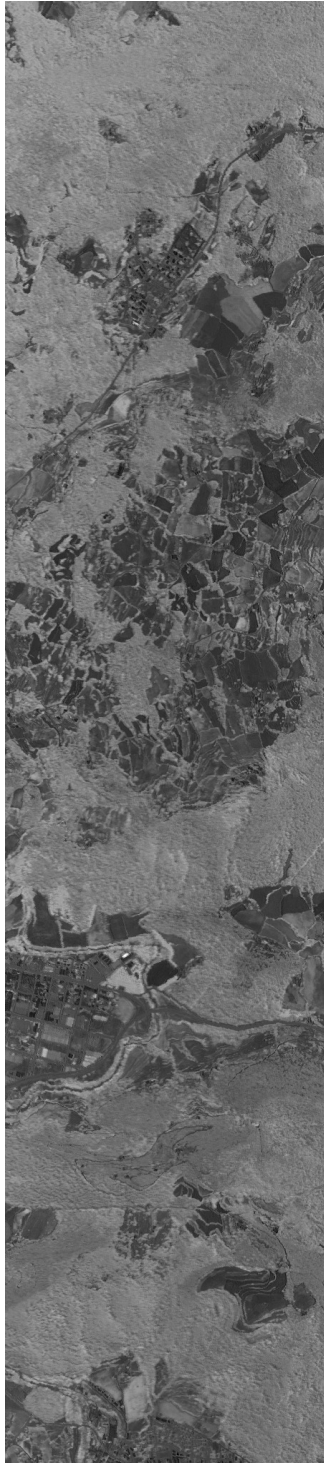
108

#4

#5

Figure 9.5: Abundance images corresponding to the endmembers discovered by the $(\mu + \lambda)$-ES on the CREAF image (cont.)

#1

#2

#3

Figure 9.6: Abundance images corresponding to the endmembers discovered by the SIES on the CREAF image

#4
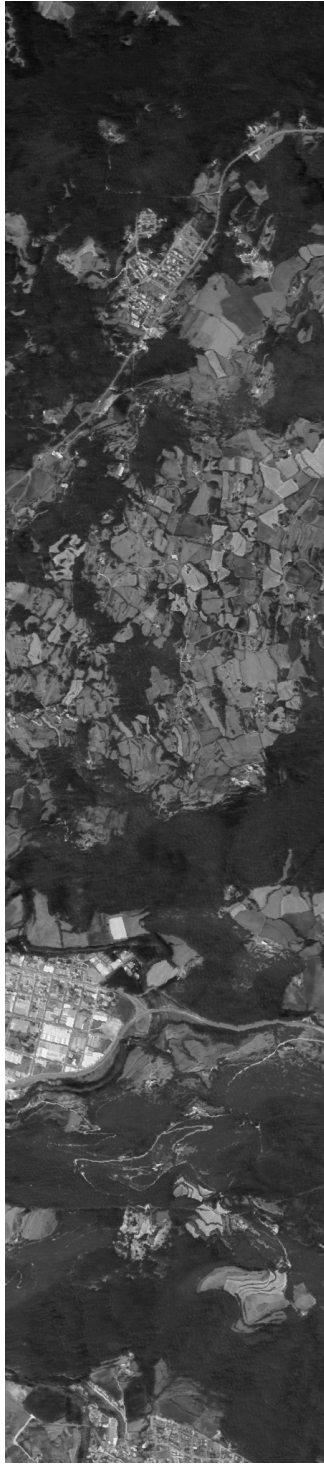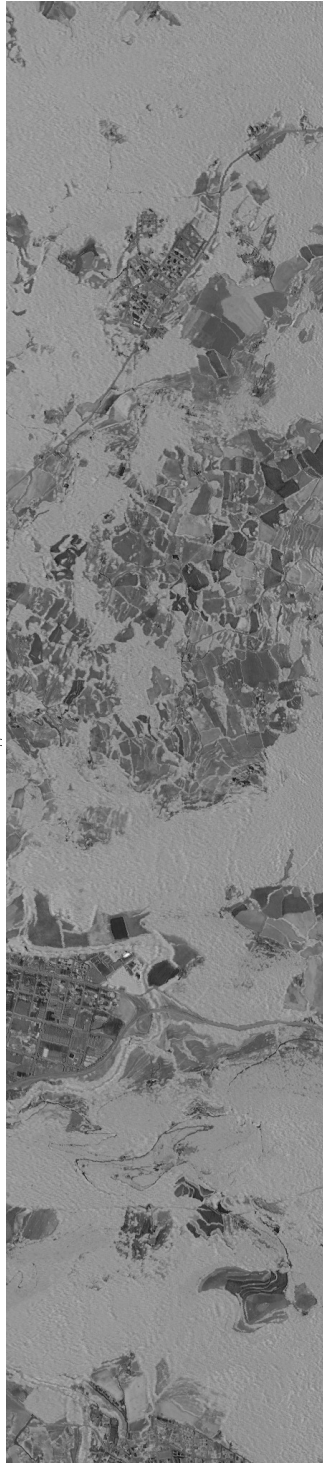
#5

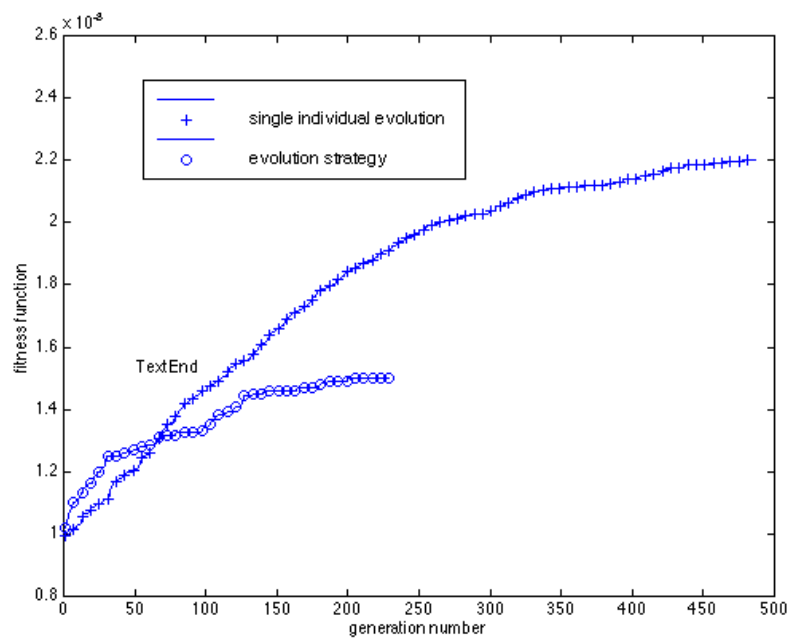Figure 9.7: Abundance images corresponding to the endmembers discovered by the SIES on the CREAF image (cont.)

Figure 9.8: Trace of the fitness function value for an instance of the ES and the SIES strategy on the Indian Pines image.
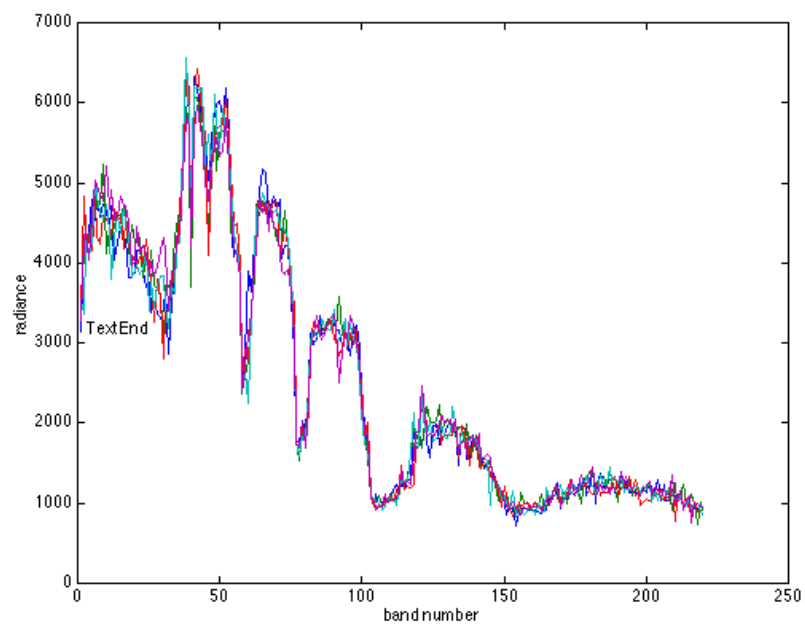
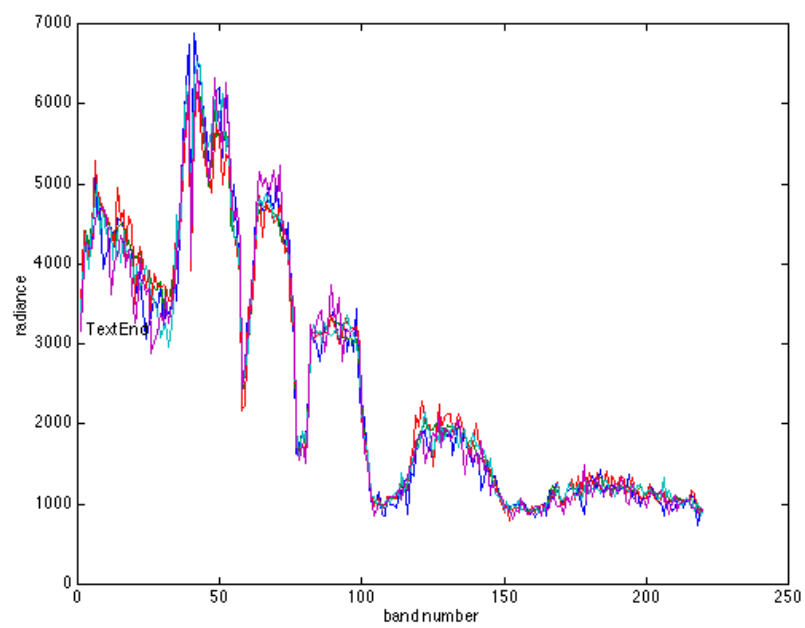Figure 9.9: Endmembers obtained by an instance of the ES on the Indian Pines image

Figure 9.10: Endmembers detected by the SIES on the Indian Pines image.

image. In this image, the computational cost of $(\mu + \lambda)$-ES was substantially greater than that of SIES, for this reason we allowed the SIES experiment to run longer. Anyway, at the 250 generation the fitness performance of SIES was better than that of the $(\mu + \lambda)$-ES. The endmembers found by of the $(\mu + \lambda)$-ES and SIES are plotted in figures 9.9 and 9.10, respectively. The endmembers obtained by SIES have a greater variability.

The abundance images are presented in figures 9.11 and 9.12 for of the $(\mu + \lambda)$-ES and SIES, respectively. We can compare the abundance images with the ground truth reproduced in figure B.1:

- The steel towers that appear near the upper left corner of the ground truth image. Both approaches produce good detectors of this feature. Abundace images #3 and #4 of the $(\mu + \lambda)$-ES, and #2 and #3 of the SIES (counting row-wise), show high detection of this feature. At the same time these abundances show high responses in pixels corresponding to cultivated lands. This can be understood if we consider that the crops were at very early stages of growth, therefore most of the land surface could be bare soil.

- The vegetation cover is better represented by the woods. Besides the regions identified in the ground truth, it seems that much of the background was also woods. The abundance images #3 and #4 of the SIES show good detection of these woods. They are well detected also by abundances #1, #2 and #5 of the $(\mu + \lambda)$-ES. The detection of the woods area in the lower right corner and its extension to other areas of the image is in good agreement with the results of some studies [100, 99, 101] on the application of supervised classification to this image. Our approach has the advantage of producing these results without previous labelling of the data.

- The crop fields are well detected by abundance #3 of the $(\mu + \lambda)$-ES, though confused somehow with the steel towers and without discrimination among them. A special case is the wheat field which is not well detected by any endmember. This may be due to a different stage of growth. By coincidence, abundance #3 of SIES shows the best detection of the crop fields.

- Another interesting feature that appears in both sets is the agreement in the detection of the roads and railway tracks that cross the image.

115

9.6   Conclusions

In this chapter we describe the application of a conventional $(\mu + \lambda)$-ES evolutionary strategy to endmember induction from hyperespectral images. We introduce the straightforward encoding of the problem and a fitness function that embodies the constraints of linear spectral mixing and the minimization of the reconstruction error. We also propose a Single Individual Evolutionary Strategy (SIES) following the Michigan approach. The SIES is computationally lighter than the conventional $(\mu + \lambda)$-ES. We have show in two real life images that the SIES performs better than the $(\mu + \lambda)$-ES in terms of fitness function optimization. The SIES shows the improvement introduced by the mutation of single endmember spectra inside the set of endmembers represented by the current population. Selection is elitist, so the algorithm retains good convergence properties despite the approximate nature of the representation and manipulation of the solutions. When studying the abundance images obtained by both methods, we found that the identification of ground truth cover classes is similar in both approaches.

#1

#2

#3

#4

#5
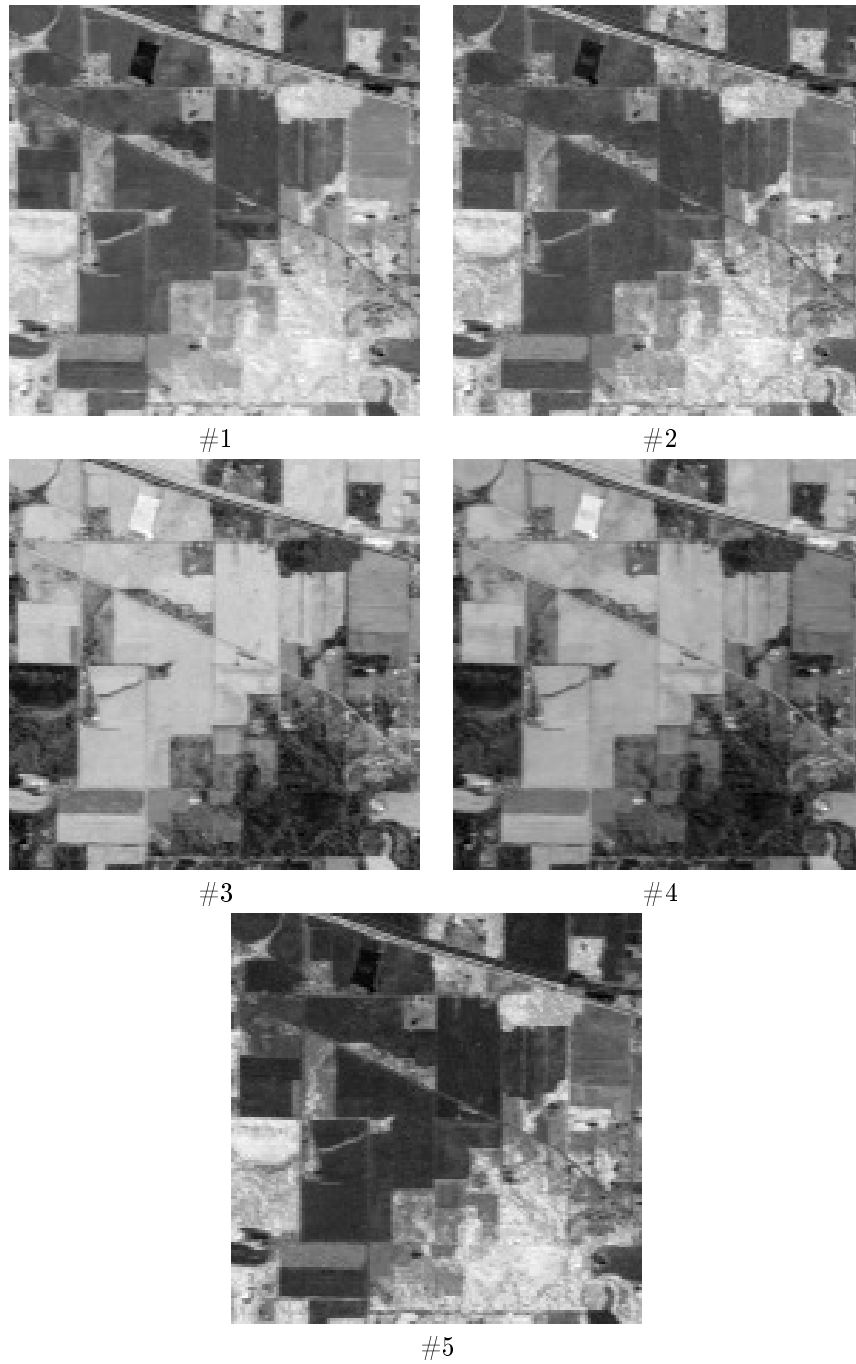
Figure 9.11: Abundance images corresponding to the endmembers discovered by the $(\mu + \lambda)$-ES on the Indian Pines image
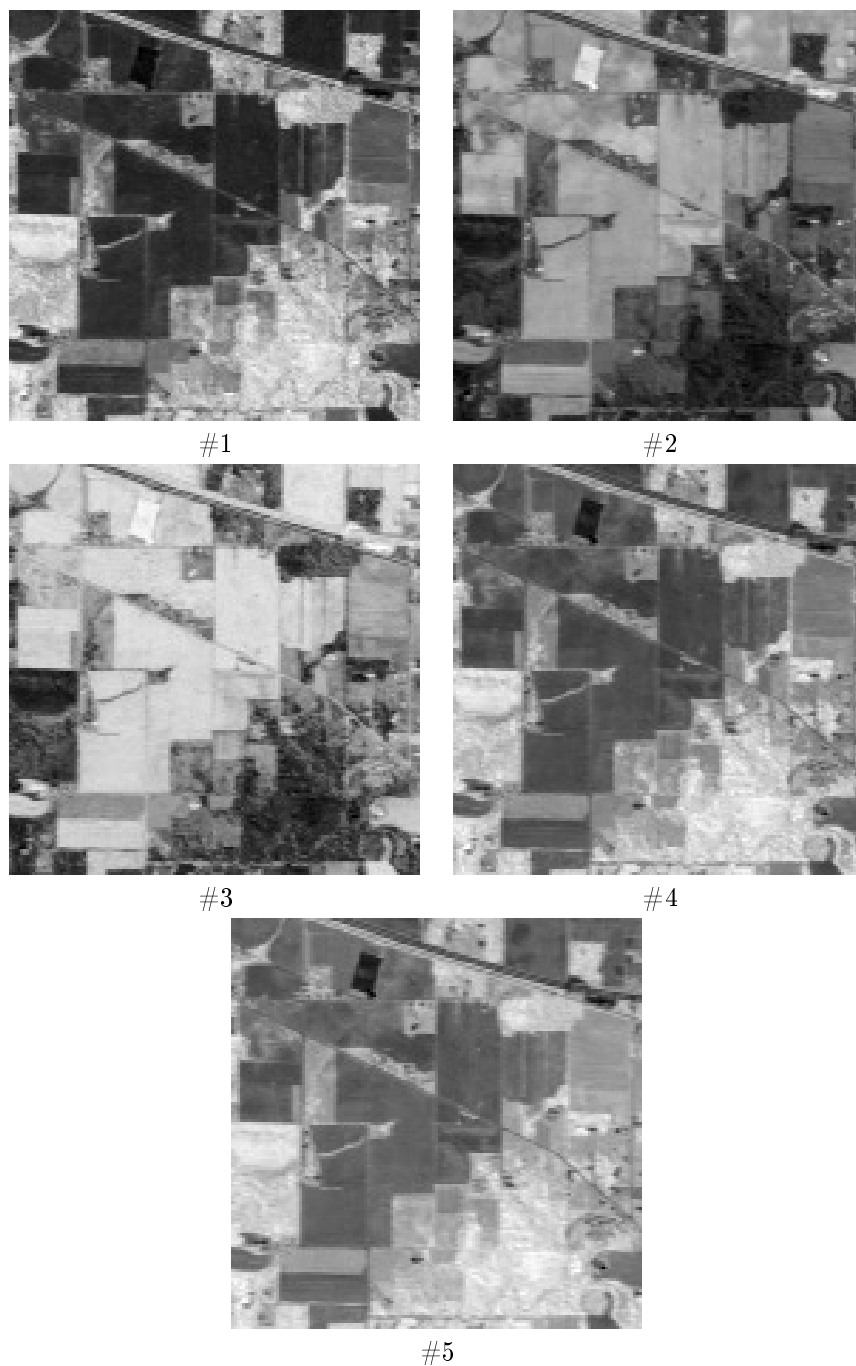
117

#1

#2

#3

#4

#5

Figure 9.12: Abundance images corresponding to the endmembers discovered by the SIES strategy in the Indian Pines image

Appendix A

Synthetic hyperspectral images

The hyperspectral images used for the experimental results are generated as linear mixtures of a set of spectra (the ground truth endmembers) with synthesized abundance images. The ground truth endmembers were selected from the USGS spectral libraries corresponding to the AVIRIS flights. Figures A.2, A.1 and A.3 show the spectra used as endmembers in the 2, 3 and 5 endmember images. The first 2 spectra are well detached, and our algorithm must find them easily. The spectra in the case of 3 and 5 endmembers are less clearly separated, they are morphologically independent in at least one sense (erosive or dilative) but most of the times is due to the vector lexicographic order being a partial ordering. Nevertheless, the notion of morphological independence does not require a total order to serve our purposes.

The synthetic ground truth abundance images were generated in a two step procedure,

1. First, we simulate each as an gaussian random field with Matern correlation function of parameters (θ_1, θ_2) varying between 2 and 20. We applied the procedures proposed by [55] for the efficient generation of big domain gaussian random fields.

2. Second, to ensure that there are regions of almost pure endmembers, we selected for each pixel the abundance coefficient with the greater value
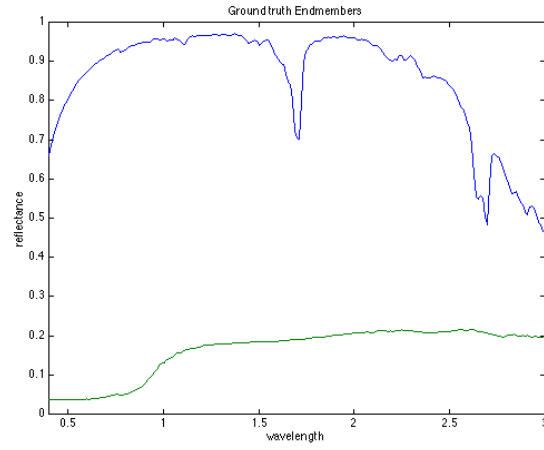
Figure A.1: Ground truth endmembers extracted from the USGS library used for the 2 endmember images
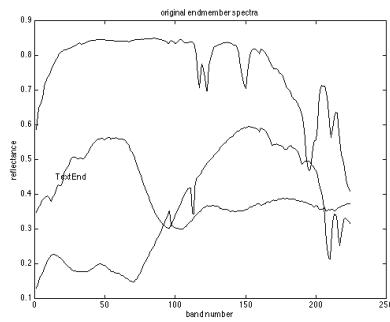

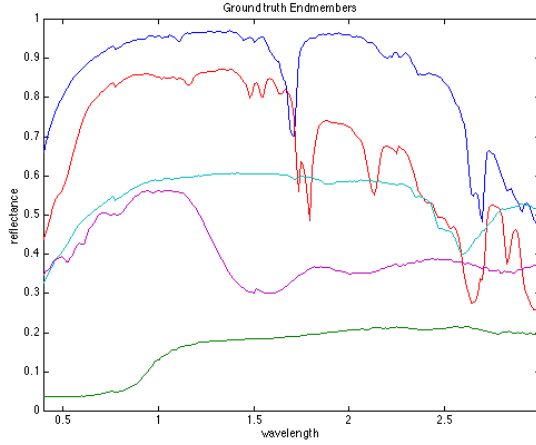Figure A.2: Ground truth endmember spectra, case of 3 endmembers

Figure A.3: Ground truth endmembers extracted from the USGS library used for the 5 endmember images

and we normalize the remaining to ensure that the abundance coefficients in this pixel sum up to one.

It can be appreciated on the abundance images that each endmember has several regions of almost pure pixels, viewed as brighter regions in the images. Image size is 64×64 pixels of 224 spectral bands each. We have 8 images with 2 endmember/abundances and 5 images with 5 endmember/abundances. High correlation produces smooth distributions of the abundances.

Figures A.4, A.5 and A.6 present intances of the generated abundance images for the case of 2, 3 and 5 endmembers, respectively. Note the noisy aspect of the image, instead of making up simple geometrical distributions and corrupting it with noise, the gaussian field covariance function control parameters allow to obtain images with diverse degrees of noise appearance. For some applications, like target detection, it may be more appropriate to layout some specific regions in the image and to perform a conditional simulation to obtain noisy and realistic versions of the scene.

The gaussian distribution of the abundance images is an inconvenient when applying ICA, so it may be interesting to build new non gaussian abundance images. It must be noted that corrupting synthetic images obtained by other means is usually done adding gaussian noise. This procedure will pose the same inconvenient as ours regarding ICA. On the positive side, the synthesis

121

of abundance images as random fields allows to control the intrinsic noisiness of the simulated scenes. Noise can be added as usual, to simulate capture and transmission conditions.
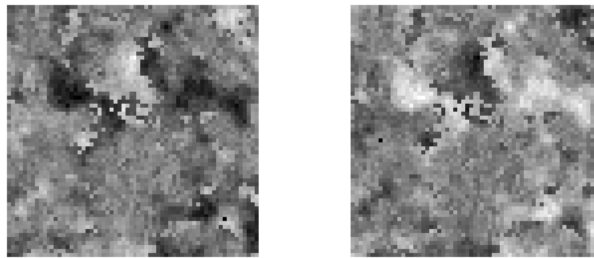
Figure A.4: Ground truth synthetic abundance images of the 2 endmember hyperspectral image.

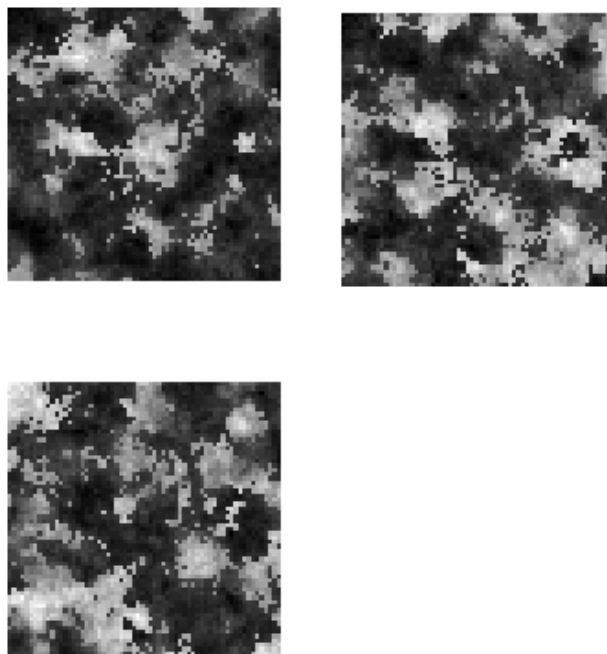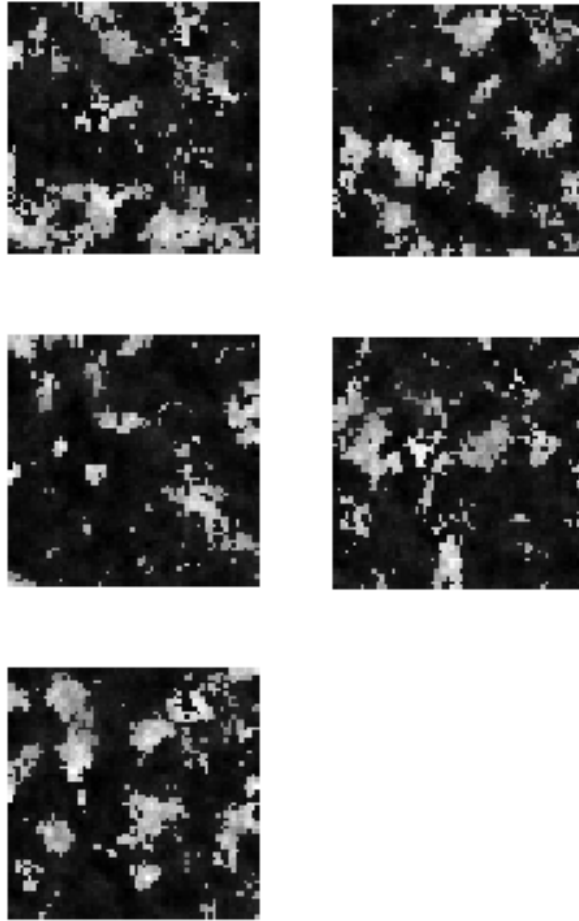Figure A.5: Ground truth synthetic abundance images of the 3 endmember hyperspectral image.

Figure A.6: Ground truth synthetic abundance images of the 5 endmembers hyperspectral image.

Appendix B

Hyperspectral and multiespectral data from remote sensing

This appendix contain the description of real world remote sensing images used in the experiments reported in this PhD.
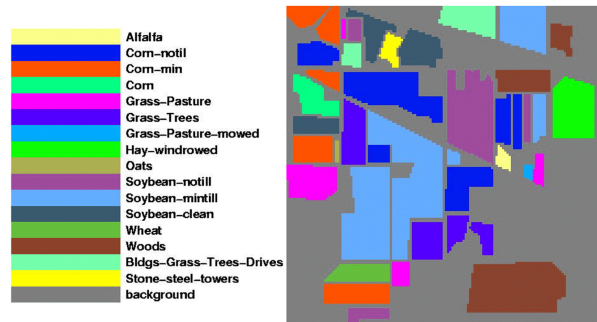

Figure B.1: Ground truth of the Indian Pines image.

B.1   Indian Pines

The Indian Pines 1992 image was obtained by the Airborne Visible/Infrared Imaging Spectrometer (AVIRIS) developed by NASA JPL which has 224 contiguous spectral channels covering a spectral region from 0.4 to 2.5 mm in 10 nm steps. It is a 145 by 145 pixel image with 220 spectral bands that contains a distribution of two-thirds of agricultural land and one-third of forest and other elements (two highways, a railroad track, some houses and smaller roads). The full data set is called Indian Pines 1 920612B, and it is available at http://makalu.jpl.nasa.gov/locator/index.html. The image ground truth designates 16 mutually exclusive classes of land cover. Figure B.1 shows the ground truth as given in [99, 100, 101], where some supervised classification approaches are experimented over this image. Besides it has been widely used in many hyperspectral image processing studies [102].

B.2   Salinas

Hyperspectral data collected by the AVIRIS imaging spectrometer in 1998 over Salinas Valley, California. The full scene (Salinas C) consists of 512 lines by 217 samples with 224 spectral bands from 0.4 μm - 2.5 μm with a pixel resolution of 3.7mx3.7m. These data was available only as sensor radiance data and includes vegetables, bare soils and vineyard fields. The subscene of the dataset (Salinas A) comprises 83x86 pixels and is used sometimes because it has much less background pixels. The ground truth of this image is shown in figure B.2. The ground truth for the whole scene is shown in figure B.3.

B.3   The CREAF image

The first data set used for the experimental work corresponds to a multispectral image of size of 710x4558 pixels which covers a large area including vegetation, cultivated land areas and urban areas. This image has been acquired through a CASI (Compact Airbone Spectrographic Imager) sensor using a general configuration of 14 bands, that is, each pixel is represented by a vector of 14 components each a 8-bpp gray scale value. From all the 14 bands of the original image, a smaller region of 448x2048 pixels has been selected (croped). For the operation
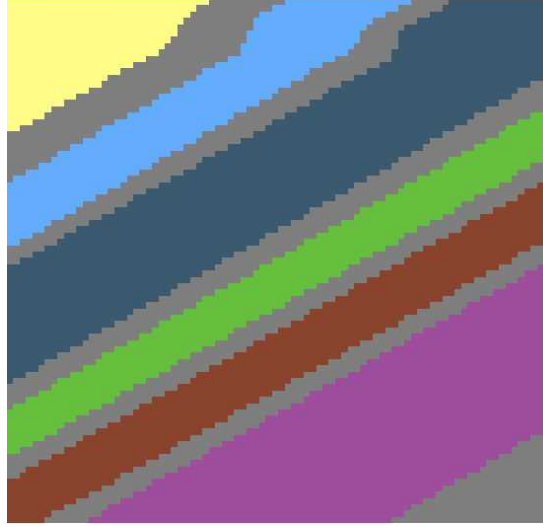
Figure B.2: Salinas A ground truth

of both the ES and the SIE a 8:1 subsampled version of this region has been used to compute the fitness function value. However, final abundance results were computed over the 448x2048 pixels region.

The ground truth of the image is composed of the following categories of land cover: **A** evergreen trees. **B** deciduous trees. **C** brushwoods. **D** meadows and crops. **E** urban areas. The ground truth is visualized in figure B.4 assigning an increasing intensity to the land cover categories: black corresponds to evergreen trees and white to urban areas.
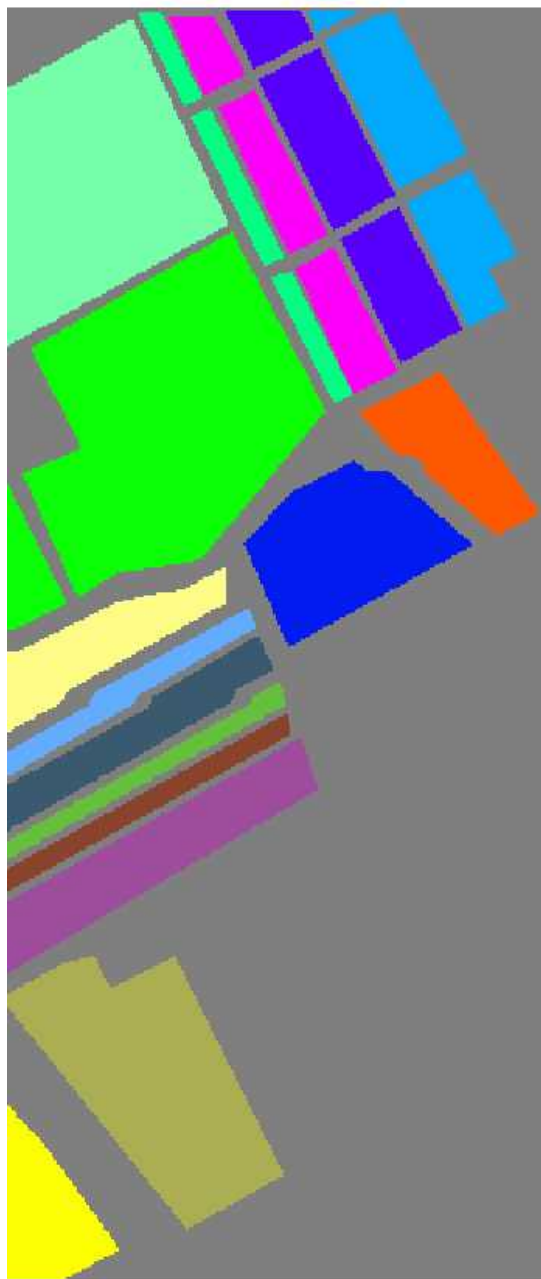
Figure B.3: Salinas C ground truth
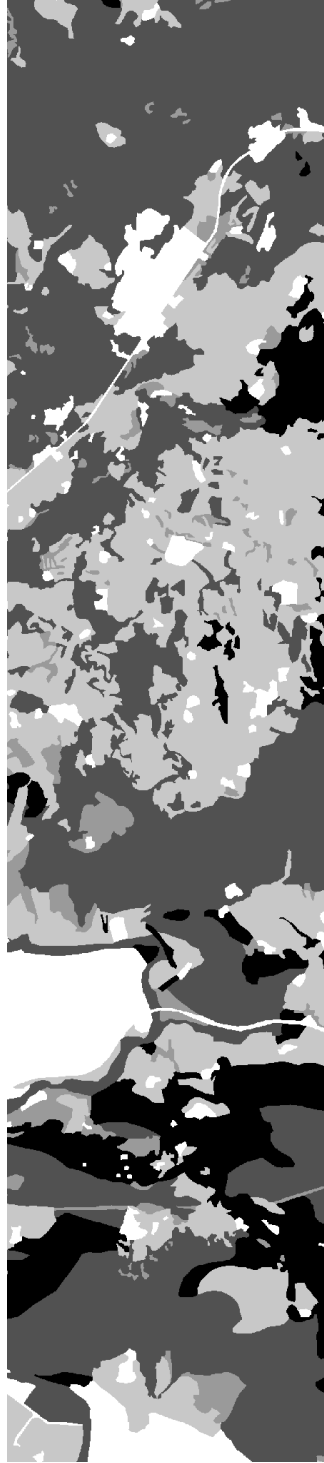
Figure B.4: Ground truth of the CREAF image. White corresponds to urban areas (class **E**). Black corresponds to evergreen trees (class **A**). Intermediate grey values correspond to meadows, brushwoods, deciduous trees, (classes **D**, **C**, **B**).

Bibliography

[1] Finding optimal decision scores by evolutionary strategies. *Artificial Intelligence in Medicine*, 32(2):85 − 95, 2004.

[2] Parametric optimization with evolutionary strategies in particle physics. *Nuclear Instruments and Methods in Physics Research Section A: Accelerators, Spectrometers, Detectors and Associated Equipment*, 534(1-2):147 − 151, 2004. Proceedings of the IXth International Workshop on Advanced Computing and Analysis Techniques in Physics Research.

[3] An approach to sustainable 'fashion' e-retail: A five-stage evolutionary strategy for 'clicks-and-mortar' and 'pure-play' enterprises. *Journal of Retailing and Consumer Services*, 13(4):289 − 299, 2006.

[4] On the combination of evolutionary algorithms and stratified strategies for training set selection in data mining. *Applied Soft Computing*, 6(3):323 − 332, 2006.

[5] J.B. Adams and A.R. Gillespie. *Remote Sensing of Landscapes with Spectral Images: A Physical Modeling Approach.* Cambridge University Press, 2006.

[6] S. Alayon, J.I. Estevez, J. Sigut, J.L. Sanchez, and P. Toledo. An evolutionary michigan recurrent fuzzy system for nuclei classification in cytological images using nuclear chromatin distribution. *Journal of Biomedical Informatics*, 39(6):573 − 588, 2006.

[7] Torsten Asselmeyer and Werner Ebeling. Unified description of evolutionary strategies over continuous parameter spaces. *Biosystems*, 41(3):167 − 178, 1997.

[8] T. Bäck. *Evolutionary Algorithms in Theory and Practice*. Oxford University Press, New York, 1996.

[9] T. Bäck and H.P. Schwefel. An overview of evolution algorithms for parameter optimization. *Evolutionary Computation*, 1(1):1–24, 1993.

[10] T. Bäck and H.P. Schwefel. Evolutionary computation: an overview. In IEEE Press, editor, *ICEC'96*, pages 20–29, 1996.

[11] Larry Biehl and David Landgrebe. Multispec–a tool for multispectral-hyperspectral image data analysis. *Computers & Geosciences*, 28(10):1153 − 1159, 2002.

[12] Edward A. Billard. Evolutionary strategies of stochastic learning automata in the prisoner's dilemma. *Biosystems*, 39(2):93 − 107, 1996.

[13] Kerstin Bunte, Michael Biehl, Marcel F. Jonkman, and Nicolai Petkov. Learning effective color features for content based image retrieval in dermatology. *Pattern Recognition*, In Press, Corrected Proof:−, 2010.

[14] C.-I. Chang and A. Plaza. A fast iterative algorithm for implementation of pixel purity index. *Geoscience and Remote Sensing Letters, IEEE*, 3(1):63–67, 2006.

[15] Hong Chang and Dit-Yan Yeung. Kernel-based distance metric learning for content-based image retrieval. *Image and Vision Computing*, 25(5):695 − 703, 2007.

[16] Zhenyong Chen, Yongyong He, Fulei Chu, and Jingyuan Huang. Evolutionary strategy for classification problems and its application in fault diagnostics. *Engineering Applications of Artificial Intelligence*, 16(1):31 − 38, 2003.

[17] Shyi-Chyi Cheng. Content-based image retrieval using moment-preserving edge detection. *Image and Vision Computing*, 21(9):809 − 826, 2003.

[18] Shyi-Chyi Cheng, Tzu-Chuan Chou, Chao-Lung Yang, and Hung-Yi Chang. A semantic learning for content-based image retrieval using analytical hierarchy process. *Expert Systems with Applications*, 28(3):495 − 505, 2005.

[19] John Y. Chiang and Shuenn-Ren Cheng. Multiple-instance content-based image retrieval employing isometric embedded similarity measure. *Pattern Recognition*, 42(1):158 – 166, 2009.

[20] L. O. Chua and T. Roska. *Cellular neural networks and visual computing: foundation and applications*. Cambridge University Press, June 2002.

[21] L.O. Chua and L. Yang. Cellular neural networks: applications. *Circuits and Systems, IEEE Transactions on*, 35(10):1273–1290, 1988.

[22] L.O. Chua and L. Yang. Cellular neural networks: theory. *Circuits and Systems, IEEE Transactions on*, 35(10):1257–1272, 1988.

[23] Roger N. Clark and Ted L. Roush. Reflectance spectroscopy: Quantitative analysis techniques for remote sensing applications. *Journal of Geophysics Research*, 89(B7):6329–6340, 1984.

[24] M. Craig. Minimum volume transformations for remotely sensed data. *IEEE Trans. Geos. Rem. Sensing*, 32(3):542–552, 1994.

[25] Ricardo da S. Torres, Alexandre X. Falco, Marcos A. Gonzalves, Joao P. Papa, Baoping Zhang, Weiguo Fan, and Edward A. Fox. A genetic programming framework for content-based image retrieval. *Pattern Recognition*, 42(2):283 – 292, 2009. Learning Semantics from Multimedia Content.

[26] Sumitesh Das. Modeling mixed microstructures using a multi-level cellular automata finite element framework. *Computational Materials Science*, 47(3):705 – 711, 2010.

[27] H. Daschiel and M. Datcu. Information mining in remote sensing image archives: system evaluation. *Geoscience and Remote Sensing, IEEE Transactions on*, 43(1):188–199, 2005.

[28] M. Datcu, H. Daschiel, A. Pelizzari, M. Quartulli, A. Galoppo, A. Colapicchioni, M. Pastori, K. Seidel, P.G. Marchetti, and S. D'Elia. Information mining in remote sensing image archives: system concepts. *Geoscience and Remote Sensing, IEEE Transactions on*, 41(12):2923–2936, 2003.

[29] M. Datcu and K. Seidel. Human centered concepts for exploration and understanding of satellite images. In *Advances in Techniques for Analysis of Remotely Sensed Data, 2003 IEEE Workshop on*, pages 52–59, 2003.

[30] M. Datcu, K. Seidel, and M. Walessa. Spatial information retrieval from remote-sensing images. I. Information theoretical perspective. *Geoscience and Remote Sensing, IEEE Transactions on*, 36(5):1431–1445, 1998.

[31] E. de Ves, J. Domingo, G. Ayala, and P. Zuccarello. A novel bayesian framework for relevance feedback in image content-based retrieval systems. *Pattern Recognition*, 39(9):1622 – 1632, 2006.

[32] S. D'Elia. Image information mining for earth observation at ESA. In *Geoscience and Remote Sensing Symposium, 2004. IGARSS '04. Proceedings. 2004 IEEE International*, volume 1, page 171, 2004.

[33] B. Demir and S. Erturk. Hyperspectral data classification using RVM with pre-segmentation and RANSAC. In *Geoscience and Remote Sensing Symposium, 2007. IGARSS 2007. IEEE International*, pages 1763–1766, 2007.

[34] Z. Eslami, S.H. Razzaghi, and J. Zarepour Ahmadabadi. Secret image sharing based on cellular automata and steganography. *Pattern Recognition*, 43(1):397 – 404, 2010.

[35] Keinosuke Fukunaga. *Introduction to statistical pattern recognition*. Academic Press, 1990.

[36] Iker Gondra and Douglas R. Heisterkamp. Content-based image retrieval with the normalized information distance. *Computer Vision and Image Understanding*, 111(2):219 – 228, 2008.

[37] M. Grana and J. Gallego. Hyperspectral image analysis with associative morphological memories. In *Image Processing, 2003. ICIP 2003. Proceedings. 2003 International Conference on*, volume 3, pages III–549–52 vol.2, 2003.

[38] M. Graña, A. Manhaes-Savio, M. García-Sebastián, and E. Fernandez. A lattice computing approach for on-line fmri analysis. *Image and Vision Computing*, 28(7):1155–1161, 2010.

[39] M. Graña, B. Raducanu, P. Sussner, and G.X. Ritter. Advances in artificial intelligence- iberamia 2002. volume 2527 of *LNAI*, chapter On endmember detection in hyperspectral images with Morphological Associative Memories, pages 526–535. Springer Verlag, 2002.

[40] M. Graña, I. Villaverde, J.O. Maldonado, and C. Hernandez. Two lattice computing approaches for the unsupervised segmentation of hyperspectral images. *Neurocomputing*, 72(10-12):2111–2120, 2009.

[41] Manuel Grana, Ivan Villaverde, José O. Maldonado, and Carmen Hernandez. Two lattice computing approaches for the unsupervised segmentation of hyperspectral images. *Neurocomput.*, 72(10-12):2111–2120, 2009.

[42] Ajay K. Gupta and Garrison W. Greenwood. Static task allocation using (μ, λ) evolutionary strategies. *Information Sciences*, 94(1-4):141 − 150, 1996.

[43] Bruce Hapke. *Theory of Reflectance and Emittance Spectroscopy.* Cambridge University Press, September 1993.

[44] A. Hyvärinen, J. Karhunen, and E. Oja. *Independent component analysis.* John Wiley and Sons, May 2001.

[45] A. Hyvärinen and E. Oja. A fast fixed-point algorithm for Independent Component Analysis. *Neural Computation*, 9(7):1483–1492, 1997.

[46] A. Ifarraguerri and C.I. Chang. Multispectral and hyperspectral image analysis with convex cones. *IEEE Trans. Geos. Rem. Sensing*, 37(2):756–770, 1999.

[47] P.T. Jackway. Gradient watersheds in morphological scale-space. *Image Processing, IEEE Transactions on*, 5(6):913 −921, jun. 1996.

[48] N. Jhanwar, S. Chaudhuri, G. Seetharaman, and B. Zavidovique. Content based image retrieval using motif cooccurrence matrix. *Image and Vision Computing*, 22(14):1211 − 1220, 2004. The Indian Conference on Vision, Graphics and Image Processing.

[49] Hopfield J.J. Neural networks and physical systems with emergent collective computational abilities. *Proc. Nat. Acad. Sciences*, 79(2554-2558), 1982.

[50] P.S. Karvelis, A.T. Tzallas, D.I. Fotiadis, and I. Georgiou. A multichannel watershed-based segmentation method for multispectral chromosome classification. *Medical Imaging, IEEE Transactions on*, 27(5):697 −708, may. 2008.

[51] Graham Kendall, Jane M Binner, and Alicia M Gazely. Evolutionary strategies: A new macroeconomic policy tool? In R. Neck, editor, *Modeling and Control of Economic Systems 2001*, pages 377 − 381. Elsevier Science Ltd, Oxford, 2003.

[52] N. Keshava and J.F. Mustard. Spectral unimixing. *IEEE Signal Proc. Mag.*, 19(1):44–57, 2002.

[53] A. R. Khan, P. P. Choudhury, K. Dihidar, and R. Verma. Text compression using two-dimensional cellular automata. *Computers and Mathematics with Applications*, 37(6):115 − 127, 1999.

[54] M. L. Kherfi, D. Ziou, and A. Bernardi. Combining positive and negative examples in relevance feedback for content-based image retrieval. *Journal of Visual Communication and Image Representation*, 14(4):428 − 457, 2003.

[55] B. Kozintsev. *Computations With Gaussian Random Fields*. Phd thesis, 1999.

[56] Boris Kozintsev. *Computations with Gaussian Random Fields, PhD Thesis*. University of Maryland, 1999.

[57] Jung Won Kwak and Nam Ik Cho. Relevance feedback in content-based image retrieval system by selective region growing in the feature space. *Signal Processing: Image Communication*, 18(9):787 − 799, 2003.

[58] Jorma Laaksonen, Markus Koskela, Sami Laakso, and Erkki Oja. Picsom - content-based image retrieval with self-organizing maps. *Pattern Recognition Letters*, 21(13-14):1199 − 1207, 2000. Selected Papers from The 11th Scandinavian Conference on Image.

[59] Zhi Lin. An algorithm of evolutionarily stable strategies for the single-population evolutionary game. *Journal of Computational and Applied Mathematics*, 217(1):157 − 165, 2008.

[60] Yan Liu and Stuart R. Phinn. Modelling urban development with cellular automata incorporating fuzzy-set approaches. *Computers, Environment and Urban Systems*, 27(6):637 − 658, 2003. Part Special Issue: Urban Data Management Society.

[61] Ying Liu, Dengsheng Zhang, Guojun Lu, and Wei-Ying Ma. A survey of content-based image retrieval with high-level semantics. *Pattern Recognition*, 40(1):262 − 282, 2007.

[62] J. O Maldonado, D. Vicente, M. A Veganzones, and M. Grana. Spectral indexing for hyperspectral image CBIR. In *ESA-EUSC 2006*, Torrejon air base, Madrid (Spain), 2006.

[63] D. Manolakis and G. Shaw. Detection algorithms for hyperspectral imaging applications. *Signal Processing Magazine, IEEE*, 19(1):29–43, January 2002.

[64] D. Manolakis and G. Shaw. Detection algorithms for hyperspectral imaging applications. *Signal Processing Magazine, IEEE*, 19(1):29–43, January 2002.

[65] B. McKay. Evolutionary algorithms. In Sven Erik Jorgensen and Brian Fath, editors, *Encyclopedia of Ecology*, pages 1464 − 1472. Academic Press, Oxford, 2008.

[66] Shashi Bhushan Mehta, Santanu Chaudhury, Asok Bhattacharyya, and Amarnath Jena. Tissue classification in magnetic resonance images through the hybrid approach of michigan and pittsburg genetic algorithm. *Applied Soft Computing*, In Press, Accepted Manuscript:−, 2011.

[67] Brian S. Penn. Using simulated annealing to obtain optimal linear end-member mixtures of hyperspectral data. *Computers & Geosciences*, 28(7):809 − 817, 2002.

[68] Brian S. Penn. Using self-organizing maps to visualize high-dimensional data. *Computers & Geosciences*, 31(5):531 − 544, 2005.

[69] A. Plaza, P. Martinez, R. Perez, and J. Plaza. Spatial/spectral endmember extraction by multidimensional morphological operations. *Geoscience and Remote Sensing, IEEE Transactions on*, 40(9):2025–2041, 2002.

[70] A. Plaza, P. Martinez, R. Perez, and J. Plaza. A quantitative and comparative analysis of endmember extraction algorithms from hyperspectral data. *Geoscience and Remote Sensing, IEEE Transactions on*, 42(3):650–663, 2004.

[71] Antonio Plaza, Javier Plaza, and Abel Paz. Improving the scalability of hyperspectral imaging applications on heterogeneous platforms using adaptive run-time data compression. *Computers & Geosciences*, In Press, Corrected Proof:–, 2010.

[72] G. Qiu. Indexing chromatic and achromatic patterns for content-based colour image retrieval. *Pattern Recognition*, 35(8):1675 – 1686, 2002.

[73] G. Quellec, M. Lamard, G. Cazuguel, B. Cochener, and C. Roux. Wavelet optimization for content-based image retrieval in medical databases. *Medical Image Analysis*, 14(2):227 – 241, 2010.

[74] Bogdan Raducanu, Manuel Graña, and F. Xabier Albizuri. Morphological scale spaces and associative morphological memories: Results on robustness and practical applications. *J. Math. Imaging Vis.*, 19(2):113–131, 2003.

[75] R.S. Rand and D.M. Keenan. A spectral mixture process conditioned by gibbs-based partitioning. *IEEE Trans. Geos. Rem. Sensing*, 39(7):1421–1434, 2001.

[76] Irene Ring. Evolutionary strategies in environmental policy. *Ecological Economics*, 23(3):237 – 249, 1997.

[77] G. X. Ritter, J. L. Diaz de Leon, and P. Sussner. Morphological bidirectional associative memories. *Neural Networks*, 12(6):851 – 867, 1999.

[78] G. X. Ritter, J.L. Diaz de Leon, and P. Sussner. Morphological Bidirectional Associative Memories. *Neural Networks*, 12(6):851–867, 1999.

[79] Gerhard Ritter and Paul Gader. Fixed points of lattice transforms and lattice associative memories. volume 144 of *Advances in Imaging and Electron Physics*, pages 165 – 242. Elsevier, 2006.

[80] Gerhard Ritter and Paul Gader. Fixed points of lattice transforms and lattice associative memories. volume 144 of *Advances in Imaging and Electron Physics*, pages 165 – 242. Elsevier, 2006.

[81] Gerhard X. Ritter and Gonzalo Urcid. Lattice algebra approach to endmember determination in hyperspectral imagery. volume 160 of *Advances in Imaging and Electron Physics*, pages 113 – 169. Elsevier, 2010.

138

[82] Gerhard X. Ritter, Gonzalo Urcid, and Laurentiu Iancu. Reconstruction of patterns from noisy inputs using morphological associative memories. *Journal of Mathematical Imaging and Vision*, 19:95–111, 2003. 10.1023/A:1024773330134.

[83] Gerhard X. Ritter, Gonzalo Urcid, and Laurentiu Iancu. Reconstruction of patterns from noisy inputs using morphological associative memories. *Journal of Mathematical Imaging and Vision*, 19:95–111, 2003. 10.1023/A:1024773330134.

[84] Gerhard X. Ritter, Gonzalo Urcid, and Mark S. Schmalz. Autonomous single-pass endmember approximation using lattice auto-associative memories. *Neurocomput.*, 72(10-12):2101–2110, 2009.

[85] G.X. Ritter, P. Sussner, and J.L. Diaz de Leon. Morphological Associative Memories. *Neural Networks, IEEE Transactions on*, 9(2):281–293, March 1998.

[86] G.X. Ritter, P. Sussner, and J.L. Diaz-de Leon. Morphological associative memories. *Neural Networks, IEEE Transactions on*, 9(2):281 –293, mar. 1998.

[87] Paul L. Rosin. Image processing using 3-state cellular automata. *Computer Vision and Image Understanding*, 114(7):790 – 802, 2010.

[88] J.A. Roubos, G. van Straten, and A.J.B. van Boxtel. An evolutionary strategy for fed-batch bioreactor optimization; concepts and performance. *Journal of Biotechnology*, 67(2-3):173 – 187, 1999.

[89] Chinmoy Sarkar and S.A. Abbasi. Cellular automata-based forecasting of the impact of accidental fire and toxic dispersion in process industries. *Journal of Hazardous Materials*, 137(1):8 – 30, 2006.

[90] M. Schroder, H. Rehrauer, K. Seidel, and M. Datcu. Spatial information retrieval from remote-sensing images. II. Gibbs-Markov random fields. *Geoscience and Remote Sensing, IEEE Transactions on*, 36(5):1446–1455, 1998.

[91] M. Schroder, H. Rehrauer, K. Seidel, and M. Datcu. Interactive learning and probabilistic retrieval in remote sensing image archives. *Geoscience and Remote Sensing, IEEE Transactions on*, 38(5):2288–2298, 2000.

[92] L. Shafarenko, M. Petrou, and J. Kittler. Automatic watershed segmentation of randomly textured color images. *Image Processing, IEEE Transactions on*, 6(11):1530 –1544, nov. 1997.

[93] A.W.M. Smeulders, M. Worring, S. Santini, A. Gupta, and R. Jain. Content-based image retrieval at the end of the early years. *Pattern Analysis and Machine Intelligence, IEEE Transactions on*, 22(12):1349–1380, 2000.

[94] Alex Smirnoff, Serge J. Paradis, and Ruth Boivin. Generalizing surficial geological maps for scale change: Arcgis tools vs. cellular automata model. *Computers and Geosciences*, 34(11):1550 − 1568, 2008.

[95] Adam Stawowy. Evolutionary strategy for manufacturing cell design. *Omega*, 34(1):1 − 18, 2006.

[96] P. Sussner and M.E. Valle. Gray-scale morphological associative memories. *IEEE trans. Neural Networks*, 17(3):559–570, 2006.

[97] Peter Sussner. Fixed points of Autoassociative Morphological Memories. In *Neural Networks, 2000. IJCNN 2000, Proceedings of the IEEE-INNS-ENNS International Joint Conference on*, volume 5, pages 611–616, 2000.

[98] Peter Sussner. Observations on Morphological Associative Memories and the kernel method. *Neurocomputing*, 31(1-4):167–183, 2000.

[99] S. Tadjudin and D. Landgrebe. Classification of high dimensional data with limited training samples. Technical Report TR-ECE 98-8, Purdue University., 1998.

[100] S. Tadjudin and D. Landgrebe. Covariance estimation with limited training samples. *IEEE Trans. Geos. Rem. Sensing*, 37(4):2113–2118, 1999.

[101] S. Tadjudin and D. Landgrebe. Robust parameter estimation for mixture model. *IEEE Trans. Geos. Rem. Sensing*, 38(1):439–445, 200.

[102] Y. Tarabalka, J. Chanussot, and J.A. Benediktsson. Segmentation and classification of hyperspectral images using watershed transformation. *Pattern Recognition*, 43(7):2367 − 2379, 2010.

[103] Gonzalo Urcid-S. and Juan-Carlos Valdiviezo-N. Generation of lattice independent vector sets for pattern recognition applications. volume 6700, page 67000C. SPIE, 2007.

[104] Miguel Veganzones and Manuel Grana. Endmember extraction methods: A short review. In *Knowledge-Based Intelligent Information and Engineering Systems*, pages 400–407. 2010.

[105] Miguel Angel Veganzones, José Orlando Maldonado, and Manuel Graña. On content-based image retrieval systems for hyperspectral remote sensing images. In Manuel Graña and Richard Duro, editors, *Computational Intelligence for Remote Sensing*, volume 133 of *Studies in Computational Intelligence*. Springer Verlag, 2008.

[106] Thomas Villmann, Erzsebet Merenyi, and Barbara Hammer. Neural maps in remote sensing image analysis. *Neural Networks*, 16(3-4):389 – 403, 2003. Neural Network Analysis of Complex Scientific Data: Astronomy and Geosciences.

[107] L. Vincent and P. Soille. Watersheds in digital spaces: an efficient algorithm based on immersion simulations. *Pattern Analysis and Machine Intelligence, IEEE Transactions on*, 13(6):583 –598, jun. 1991.

[108] Xiang-Yang Wang, Jing-Wei Chen, and Hong-Ying Yang. A new integrated svm classifiers for relevance feedback content-based image retrieval using em parameter estimation. *Applied Soft Computing*, 11(2):2787 – 2804, 2011. The Impact of Soft Computing for the Progress of Artificial Intelligence.

[109] M. E Winter, M. R Descour, and S. S Shen. N-FINDR: an algorithm for fast autonomous spectral end-member determination in hyperspectral data. volume 3753, pages 266–275, Denver, CO, USA, October 1999. SPIE.

[110] Xiaoqian Xu, Dah-Jye Lee, Sameer K. Antani, L. Rodney Long, and James K. Archibald. Using relevance feedback with short-term memory for content-based spine x-ray image retrieval. *Neurocomputing*, 72(10-12):2259 – 2269, 2009. Lattice Computing and Natural Computing (JCIS 2007) / Neural Networks in Intelligent Systems Designn (ISDA 2007).

[111] Peng-Yeng Yin and Shin-Huei Li. Content-based image retrieval using association rule mining with soft relevance feedback. *Journal of Visual Communication and Image Representation*, 17(5):1108 – 1125, 2006.

[112] Huan Yu, Zhengwei He, and Xin Pan. Wetlands shrink simulation using cellular automata: a case study in sanjiang plain, china. *Procedia Environmental Sciences*, 2:225 − 233, 2010. International Conference on Ecological Informatics and Ecosystem Conservation (ISEIS 2010).

[113] Jun Yue, Zhenbo Li, Lu Liu, and Zetian Fu. Content-based image retrieval using color and texture fused features. *Mathematical and Computer Modelling*, In Press, Corrected Proof:−, 2010.

[114] Djemel Ziou, Touati Hamri, and Sabri Boutemedjet. A hybrid probabilistic framework for content-based image retrieval with feature weighting. *Pattern Recognition*, 42(7):1511 − 1519, 2009.